Role of Fluid Dynamics in Nanofabrication: Growth Mechanism and Optical Properties of Ligand Free CdS Nanotubes made using Alumina Nano-Reactor

A thesis
Submitted in partial fulfillment of the requirements
Of the degree of
Doctor of Philosophy

By

Arthur Varghese

20083018

INDIAN INSTITUTE OF SCIENCE EDUCATION AND RESEARCH

PUNE

April, 2015

DEDICATION TO,
Mother and Father

Declaration

I declare that, this written submission represents my ideas in my own words and where other's ideas and works have been included, I have adequately cited and referenced the original sources. I also declare that I have adhered to all principles of academic honesty and integrity and have not misrepresented or fabricated or falsified any idea/data/fact/source in my submission. I understand that violation of the above will be cause for disciplinary action by the Institute and can also evoke penal action from the sources which have thus not been properly cited or from whom proper permission has not been taken when needed.

Date

Arthur Varghese

Roll No: 20083018

Certificate

Certified that the work incorporated in the thesis entitled "Role of Fluid Dynamics in Nanofabrication: Growth Mechanism and Optical Properties of Ligand Free CdS Nanotubes made using Alumina Nano-Reactor.", submitted by *Arthur Varghese* was carried out by the candidate, under my supervision. The work presented here or any part of it has not been included in any other thesis submitted previously for the award of any degree or diploma from any other University or Institution.

Date

Dr. Shouvik Datta

Supervisor

ACKNOWLEDGEMENTS

This thesis is one of the major remarkable achievements in my long journey of life. Without the help of most important people it is not possible to have a thesis in this current shape. It is my wish to thank to all those who helped me with valuable suggestions and their ideas to explore diverse areas.

First, I like to express my gratitude to my PhD supervisor Dr. Shouvik Datta for his continuous guidance, help, writing papers and preparing scientific documents. I specially thank him for giving a complete freedom in lab and also a most enjoyable working environment. Unique opportunity that I got to learn new techniques is not possible without him.

It is my pleasure to thank our collaborator Prasenjith Ghosh for his theoretical modeling to understand the photoluminescence process in CdS nanotubes and also providing us valuable scientific suggestions. I also thank Dr. Apratim Chatterji for his valuable modeling on diffusion based growth mechanism of nanotubes.

I would like to thank IISER Pune and Dr. K. N. Ganesh, director for providing me a magnificent research environment to fruit my goals. I thank my research advisory committee members, Dr. Prasenjith Ghosh, Dr. Surjeet Singh, Dr. Pankaj Mandal and Dr. Partha Hazra for their suggestions. I am also grateful for all people from physics department who had helped me in the academic activities. I acknowledge the fellowship that I had received during my graduation period from IISER Pune. Many thanks for IISER Pune administration for their kind support given to me. I also thank DST India and NCL Pune for providing me the facilities required for my work.

I also like to thank my lab mates, Kanika Bansal and Padmashri Patil for their valuable support during the entire graduation period.

I also thank Dr. Sulabha kulkarni and Dr. Neha Tiwari for their help during the preliminary stages of my research work. Subsequently, i thank those who had trained me to use magnetron sputtering, electron microscope and nanolithography.

Other than lab facilities, I thank IISER Pune for providing me comfortable accommodation. I thank all my IISER friends and special thanks for 2008 physics PhD batch for their support and refreshing the mind with lot of entertainments. I thank AVR Murthy, Arun Babu, Soumya Singha Roy, Madhusudan Ingale, V. Resmi, Kanika Bansal, Padmashri Patil, Madhan Gopal, K R Ramya, Abhishek Shukla, Vimal Kishore, Abhijith T Nair, Neeraj Maheswari, Atul Dwivedi and Anil Shetti for their help. I thank my initial room partners Arun Babu and AVR Murthy, starting from cooking to serious preparation for exams. I also thank Madhan Gopal for the discussion with me on various fields. I also thank to all the mess people that have provided me the food in pune.

I thank all my teachers, who had motivated me to do science. I also thank my long term friends Shinu K E, Anu V R, Eldho T M, Bhagyesh, Aniyan K E, Pratab, Kamal P Mani, Vineesh Kumar, Sreejith and Saneesh for their support and backing me all the time.

My higher studies will not be possible without an energetic support from my family members. I thank my father, mother and sister for their care, love and encouragements given to me in the entire life.

Arthur Varghese.

Contents

List of figures

Abstract

Cadmium sulfide is a well-known photoactive semiconducting material with many potential applications in optoelectronics. Most of these CdS nanostructures are grown using various physical and chemical routes. As such, it is well known that chemical synthesis process can tune the size and shape dependent physical properties of the material itself. Moreover, better knowledge on the role of hydrodynamics and kinetics of chemical reactions is very much needed to control the shape and also tuning the potential properties of nanostructures made using wet chemical nanofabrication process. Understanding such growth dynamics and subsequent modifications of physical properties of the concerned material is very important in optimizing the device quality for future applications. To probe this, we explore the role of hydrodynamics in nanofabrication process of ligand free cadmium sulfide [CdS] nanotubes self-assembled on porous alumina using a two-chamber nanoreactor based synthesis method. These CdS nanotubes show a significant photoluminescence [PL] red shift with increasing size as a result of the interplay between crystalline strain and defects incorporated during nucleation process.

Here, we present [chapter 3] a directionally asymmetric growth of CdS nanotubes on porous alumina as a result of nanoconfined reactions between two chemical precursors flowing horizontally in opposite directions. We show that the dissimilar flow rates of chemical precursors are responsible for initiating the one sided growth of CdS nanotubes on porous alumina. Structural evaluation using scanning electron microscopy images identified the nucleation sites, and also shows the elongation of CdS nanotubes. These incremental growths of CdS nanotubes may be due to plausible presence of chemo-hydrodynamic instability at the AAO-Na_2S interface. However, the estimated values of dimensionless numbers are not sufficient enough to explain the occurrence of hydrodynamic instability at nanoscale. Therefore, using the electron microscope images, we investigate the unexplored roles of chemo-hydrodynamics at liquid-liquid reactive interface for such prolonged nucleation of CdS nanotubes.

To address the presence of hydrodynamic instability during nanotubular growth, we measured the length of CdS nanotubes [chapter 4] and observed an increasing runaway growth rate with growth duration using scanning electron microscopy, which cannot be explained by simple diffusion process of reactive ions. We argue this as a signature of instability at such reactive interface. We also identified the role of precursors in this particular CdS nanotubular growth and found that sodium sulfide (Na_2S) is playing an important role in the elongation of nanotubes. Overall, many experiments are done to demonstrate the plausible chemo-hydrodynamic influence and presence of instability at nanoscale during this nanofabrication process.

To know more about the optical properties of these CdS nanotubes, we measured the PL. Interestingly, we see an enhanced PL [chapter 5] from CdS nanotubes as compared to CdS nanocrystallites made by bulk mixing of same precursors used during the synthesis of nanotubes. Even though the size of CdS nanotubes is much larger than its quantum confinement regime, we observed a sizeable shift in PL [chapter 6] with different diameter and length. In fact this can be verified from optical absorption studies, which reveals that near band edge absorption of CdS nanotubes is not affected by its size. As from experimental and theoretical results, we argue that the PL shift is mainly due to the influence of crystalline strain on cadmium vacancy minority defect at the nanotube surface as result of its unique growth process. We also show an increasing crystalline strain with size of these CdS nanotubes, which can ultimately red shift the PL peak. Calculations based on density functional theory also supported this explanation. Although sulfur interstitials having the lowest formation energy is the most abundant surface defect on these nanotubes but it is not participating in PL process. So, we predict that the nature of the defects is more important in determining the PL process as compared to defects with more concentration located on the surface.

Chapter 1
Introduction

1.1 Semiconductor nanostructures and the role of hydrodynamics in nanofabrication of ligand free cadmium sulfide nanowires within a nanoreactor

Last few decades have seen tremendous growth in research to investigate and understand various exciting physical and chemical processes happening at length scales of 1 to 1000 nm[1,2,3]. As the material size reduces to nanoscale[3-7], properties are widely influenced by its structure and size. Recent developments in technology also provided better and efficient tools to probe and comprehend the behavior of nanomaterials and nanostructures under various conditions as well as their effective use in various applications.

New physical processes and novel properties also begin to manifest as the size of these nanostructures are reduced to a level comparable to De-Broglie wavelength where the quantum confinement of electrons is dominant and surface related electronic effects play a major role[2,4,8]. This transition from classical to quantum significantly affects the structural, electronic, optical and thermal properties of the material[2,3]. Unlike the volume dominated electronic processes in bulk, increased surface to volume ratio of smaller structures influence many physical properties at nanometer length scales[2,3].

Nanostructures can be broadly classified according to their electron confinement direction in space and size[3,4,8,9]. Some structures can grow along one dimension and remain spatially restricted within nanometer length scales along the other two directions. These are normally known as 1-D nanostructures. As the lateral size becomes comparable to the De-Broglie wavelength, this one dimensional structure begins to show quantum electronic properties. Some examples of these 1D structures which have potential applications in quantum electronics are nanowires, nanotubes and nanobelts[3] etc.

It is expected that most of the promising applications of these nanostructures also come from their novel physical properties[2,3]. In modern electronics technology, a significant part of all the developments depend on the intelligent use of semiconducting materials and structures to make devices with newer functionalities. Most nanoelectronics applications are focused towards the need for future energy devices like solar cell,[10-13] super capacitors[14-17], fuel cells[18] etc. Semiconductor nanostructures with prominent light emission and with good electronic transport capabilities are suitable candidates for fabricating efficient light emitting diodes, lasers and transistors[2,3,10,19].

Designing simple and new methods to make nanomaterial's having precise shape and sizes along with narrow size distribution are one of the most important challenges in nanofabrication process. Operational parameters of any such nanoelectronic device crucially depend on these structural parameters. Therefore, many new fabrication avenues[2,3] are being utilized for growing such size and shape controlled nanostructures. These different growth conditions certainly play an important role in dictating the properties of these nanomaterial's and subsequently affect the operation of the nanodevices. Self-organization of nanostructures is also very important and this can be improved through proper understanding of the growth processes.

Moreover, most of these types of nanostructures are grown using solution based chemical routes. Usually, without a suitable substrate/template, it is difficult to grow well-organized arrays of nanostructures for potential applications. Growth processes on these substrates/templates are in general influenced by surface chemistry, reaction dynamics, external influences like pressure, current and also possibly in some cases by hydrodynamics at the liquid-liquid or liquid-solid interfaces. However, precise involvements of various hydrodynamic parameters in solution processed nanofabrication and self-assembly are not very well studied at all. Here, in this thesis we are using a particular nanoreactor based wet chemical nanofabrication route to understand the role of hydrodynamics in the growth process of cadmium sulfide nanotubes.

Usually template based chemical routes require well organized arrays of nucleation centers for fabrication of ordered 1-D nanostructures. One example for this is self-organized porous alumina having uniformly sized nanopores prepared by electrochemical anodization of aluminum metal. Such nanoporous alumina has been efficiently used to grow these types of self-assembled

nanostructures. However, it is also important to consider the role of fluid flow, membrane interfacial forces and chemo-hydrodynamic influences during solution processed fabrication and self-assembly of nanostructures. In this thesis, we are trying to understand how chemo-hydrodynamics of the aqueous reactant solutions influence the mixing and further reaction within a nanoconfined space or in a 'nanoreactor'. Such studies on the influence of flow characteristics on nanoscale self-assembly inside a nanoreactor are not commonly reported in literature. Here we use columnar nanochannels of porous alumina as a 'nanoreactor' to synthesize and self-assemble ordered arrays of 'ligand free' cadmium sulfide nanotubes by simple chemical reaction between Na_2S and $CdCl_2$. Later on we study interesting optical properties of these ligand free cadmium sulfide nanotubes using photoluminescence spectroscopy. In the next few sections of this chapter we will describe different introductory concepts on nanofabrication, fluid flow as well as semiconductor physics which will be used throughout this thesis.

1.2 Nanochannels as nanotemplate for 1-D nanostructure growth

Network of self-assembled uniform pores are generally used for simple and efficient method to fabricate 1-D ordered nanostructure and nanotubes. These templates have very small circular nanochannels with diameters in the order of 5-200 nanometers depending on growth conditions. These pores can be filled by constituent ions or reactant atoms/molecules for nucleation of structures like nanowires and nanotubes inside the confined geometry. Penetration of ions through the nanochannels and thereby allowing them to react with in these nanoconfined spaces are done by various methods like flow of electrolyte containing constituent ions through the nanochannels by pressure injection, chemical vapor deposition and electrochemical deposition[3]. Most commonly used templates are porous alumina and polycarbonate membranes[3]. Uniform pore size of electrochemically fabricated porous alumina membrane makes it a suitable candidate for growing nanowires and nanotubes.

1.3 Porous alumina

Electrochemical anodization of high purity aluminum [Al] foil [99.95%] in acidic electrolyte at an optimized voltage, temperature and concentration results in porous aluminum oxide film[20-22], widely called as porous anodic alumina template [AAO]. Optimized voltage and acid concentration give rise to well-ordered hexagonal arranged honeycomb structures as shown in the figure 1.1. Depending upon the applied voltage, pore diameter can vary from 5-200 nm with a pore density 10^9-10^{11} pores/cm^2. Initially, during anodization process, aluminum foil is oxidized to form a barrier layer of aluminum oxide[20,22] on the surface and resulting film was partially etched by the acidic electrolyte at high electric field. Strong electric field and ionic conductivity of aluminum oxide drives the ions [O^{-2}/OH^-] to migrate through the etched patches of barrier oxide layer for further growth[20] at the metal interface. In general, porous oxide layer formation occurs at anode side[21] [Al foil] and hydrogen bubbles formation occurs at cathode electrode [platinum electrode] side. The chemical reactions that take place at anode and cathode are given in equation 1.1 and 1.2 respectively.

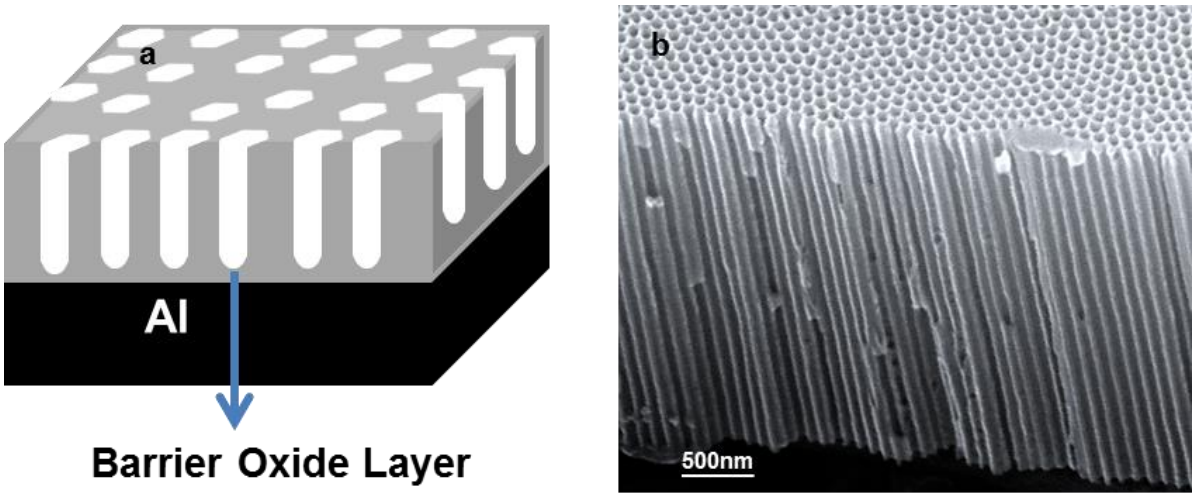

Figure 1.1: (a) Schematic picture of porous alumina membrane. This has pore structure at the upper side and barrier layer formation on the lower part[22]. The bottom side of this film have non anodized aluminum [Al].(b) Picture on the right is the scanning electron microscopy image of porous alumina anodized at 40V, which clearly shows an ordered arrangement of nanochannels.

$$2Al + 3H_2O = Al_2O_3 + 6H^+ + 6e^- \quad \textbf{(1.1)}$$

$$6H^+ + 6e^- = 3H_2 \quad \textbf{(1.2)}$$

1.4 Growth mechanism of porous alumina

Self-organization of porous alumina [figure 1.2] is not fully understood yet. However, there is a well-accepted procedure[22], where nanoporous growth occurs through two simultaneous electrochemical processes which results in pore formation with uniform diameter and pore ordering. It is believed that the reason for pore formation having uniform pore diameter is mainly due to the balance between electric field enhanced growth rate and dissolution of alumina in acid. Under normal condition, oxidation of aluminum metal result in volume expansion less than double the original film during the growth process. Origin of self-ordering of these pores may be due to the mechanical stress[23] developed during the volume expansion process. Stress developed at the bottom of the pores supports the ordering and further pushing the porous film upwards for vertical growth. Volume expansion coefficient [ξ] known as Pilling-Bedworth ratio [PBR][22,24] given by the equation 1.3 determine whether to from ordered or disordered pores.

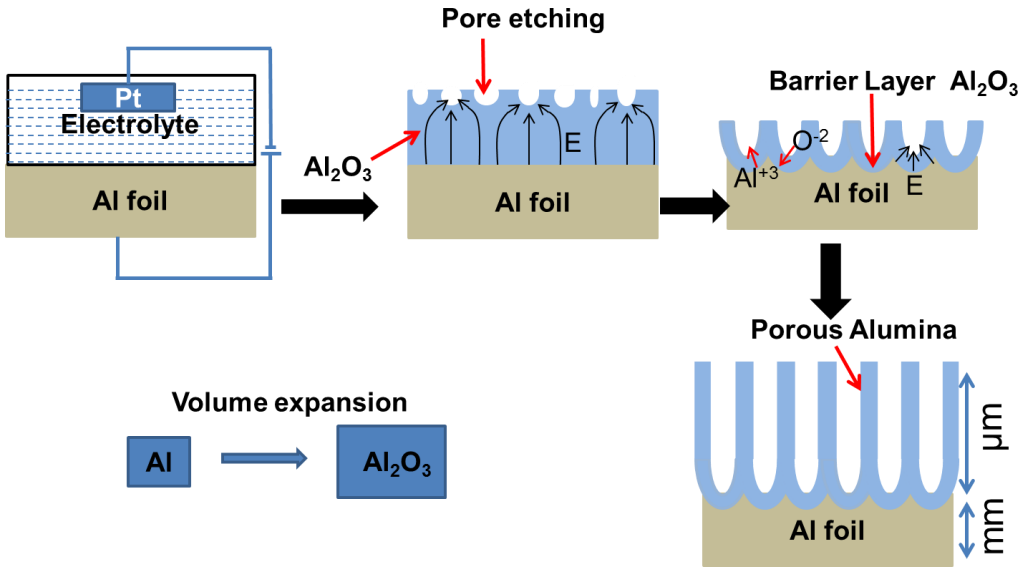

Figure 1.2: Growth process of porous alumina at various stages[20,22]. This figure shows the nanochannel formation on high purity aluminum foils from initial growth stages.

$$\xi = \frac{Volume\ of\ AAO\ (V_{Al_2O_3})}{Volume\ of\ Al\ (V_{Al})} = \frac{M_{Al_2O_3}}{M_{Al}} \times \frac{\rho_{Al}}{F_W \times \rho_{Al_2O_3}} \quad \textbf{(1.3)}$$

Where M is the molecular mass, ρ is the density and F_W is the weight fraction of aluminum ions in porous alumina, which is around 0.5.

$$Linear\ strain = \sqrt[3]{\xi} - 1 \quad \textbf{(1.4)}$$

Compressive stress developed for moderate expansion coefficient[22,24] around 1.2-1.3 will produces a well ordered pattern of uniform pores. Above these values, the maximum stress developed causes the film to break down and form bigger cracks. Expansion coefficient below 1.2 mainly gives rise to disordered pores. Stress can be calculated using the young's modulus of porous alumina and strain[25] [equation 1.4]. The value is found to be less than 4×10^3 MPa.

1.5 Influence of anodizing parameters on pores formation

1.5.1 Role of applied voltage

In general, self-organization of porous alumina can be achieved over a wide range of voltages of 5-300 V applied during anodization process in various electrolytes. Depending on various factors, break down[26-29] of porous alumina film start in the range 200-700 V and further influenced by local temperature and the type of electrolyte. As seen in figure 1.1, the barrier layer thickness and the pore diameter [D_p] are mainly depended on applied voltage. Barrier layer thickness[22] of porous alumina is experimentally measurable using scanning electron microscopy and can be estimated as 1-1.4 nm/v times the applied voltage. Pore diameter[22] is linearly related to the applied voltage with a proportionality constant λ_p= 1.3 nm/V as given in equation 1.5. Similarly inter pore distance D_c [equation 1.6] is linearly related to applied voltage by a proportionality constant λ_c= 2.5 nm/V.

$$D_p = \lambda_p . V \quad \textbf{(1.5)}$$

$$D_c = \lambda_c . V \quad \textbf{(1.6)}$$

Thickness [h] of porous layer is voltage independent and mainly dependent on the current [i] and growth duration time [t]. But other parameters like concentration, electrolyte and temperature can add to this. Rate of dissolution of alumina at local high temperature and type of electrolyte affects the growth rate of porous alumina and by avoiding some of above parameters; we can approximate the thickness[22] of porous alumina by equation 1.7.

$$h = i.k.t, \ where \ k = 3 \times 10^{-6} cm^3 (mA/min)^{-1}. \quad \textbf{(1.7)}$$

1.5.2 Concentration

Electrolyte concentration and pH[21,22] mostly determine the growth rate and the pore formation process inside a porous alumina film. Usually any well-ordered porous structure formation is not observed for an electrolyte with pH around 5-7[21] and the main reason is its reduced dissolution or etching of alumina layer. Anodizing done in a strong and mild acids [sulfuric acid, oxalic acid, phosphoric acid and citric acid] having less pH results in better ordering of pores. Lowering the pH up to a level of 1-4 can also enhance the dissolution rate[22] at lower applied potential used in anodization process. We can observe this in the case of strong sulfuric acid [0.3M, pH ~1.2], which is used for fabricating narrower channels at low voltages [10-40 V]. In porous alumina fabrication process, parameters like voltage and concentration of electrolytes are optimized [Table 1.1] for a well-ordered nanochannels.

Acid (concentration)	Applied Voltage (V)	Temperature (C)	Pore diameter (nm)
Sulfuric Acid (0.3M)	10-40	0-10	10-50
Oxalic Acid (0.3M)	30-90	0-10	40-100
Phosphoric Acid (0.3M)	100-200	0-5	100-220
Citric Acid (0.3M)	200-400	0-10	200-500

Table1.1: Optimized growth conditions for well-organized porous alumina nanochannels[21,22].

1.5.3 Role of temperature

Heat generated during anodization process at high voltages influences the dissolution rate of alumina and further leads to damage of the film[22]. Normally the electrolyte is kept at low temperature [0 to 10˚ C] to reduce the heat generated at the pore bottom during electrochemical fabrication and thereby it helps in avoiding any crack formation. This kind of breakdown of the film structure can occur mainly due to high stress developed by enhanced growth in presence of electric field and localized heat. At low temperature the growth rate of the alumina is reduced and thereby creating a better environment for self-organization. Depending on the strength of applied voltage and local heat generated, range of temperature is optimized for a better well-ordered porous structure. In general, temperature range[21] 0-7˚ C is good enough for a nicely ordered porous structure growth in oxalic and sulfuric acids but in the case phosphoric acid, it is better at 0-5˚ C.

1.6 Role of internal parameters of aluminum foil

- Aluminum foil having impurity result in different volume expansion coefficient[22] and alter the self-ordering during anodization process. Better organization of hexagonal pores can be achieved in high purity aluminum foil.

- Grain sizes on aluminum foil can also play a role in self-organization[22], which is improved in an annealed aluminum foil [500˚ C].
- Another important parameter which affects the pore formation was surface roughness[22] of film. Electro polishing of aluminum foil can reduce the roughness and further used for anodization process for the better organization of pores.

1.7 General procedure for making highly ordered pores

Masuda et al. first reported two step anodization processes[22], which can improve the uniformity and ordering of nanoporous alumina template. In most of the cases, first anodization result in less ordered porous structure as discussed in section 1.6. So to overcome this, surface of AAO membrane having pores of irregular shapes as shown in the figure 1.2 is removed by etching in 1.6 wt. % of chromic acid and 6 wt. % phosphoric acid at 70˚ C. After this process, remaining part of etched porous alumina is used for second round of anodization under the same conditions as in first anodization process, which results in highly uniform and ordered pores on the surface [figure 1.1].

1.8 Transparent porous alumina with open nanochannels

Nanochannels as shown in figure 1.1 & 1.2, having an insulating barrier layer can resist the flow of electrons and this is a major drawback in fabricating nanomaterial by electrochemical deposition using nanoporous alumina template. This also poses as a hindrance towards electrical characterization of any device made using such template. However, this barrier layer can be removed by various methods[22] and similarly the remaining part of aluminum on back side as in the figure 1.1 & 1.2, which was left untouched in the anodization process can also be etched. This is usually done by etching the backside aluminum with saturated $CuCl_2$ solution[22] which results in a transparent thin film of porous alumina with a barrier layer. Finally the nanochannels

are opened from the back end by etching this alumina barrier layer in a 5 volume % phosphoric acid solution[22].

1.9 Fabrication of nanostructures using such nanotemplate

In the past, these nicely ordered nanochannels are identified as a well suited candidate for ordered self-assembly of 1-dimensional nanostructures. Methods[3] like chemical vapor deposition [CVD], vapor-liquid-solid [VLS], electrochemical deposition and solution based chemical route are widely used for growing nanostructures like nanowires, nanotubes and nanoparticles[3,20,22] using these nanochannels. All these methods above have some comparative advantages and disadvantages. Among these methods, chemical route is simple and low cost way of fabricating 1-D nanostructures by confined nucleation of ions in these nanochannels. Most challenging here is the pore-filling process of reactant electrolytes and thereby allowing any nanoconfined growth in the confined region. All processes through these nanochannels are controlled by surface forces, which also play an important role in the flow of chemical precursors for initiating the growth. However, external force like pressure and concentration gradient can overcome the internal forces, which is hindering the flow and thereby filling process of electrolyte completely to remove the trapped air in these nanochannels. These can be achieved by external pressure, vacuum filtration[30] and also by electric field. In our experiment, two precursors [0.1M of Na_2S & 0.1M $CdCl_2$] of same height were placed on opposite side of horizontally placed alumina nanochannels. We then study the growth dynamics to investigate the role of fluid dynamics in nanoscale self-assembly.

1.10 Fluid flow in nanochannels

In general, fluid flow through nanochannels with size much above 10 nm can be easily described by continuity approximation and Navier-Stokes equations[31,32]. Fluid flow through these nanochannels is expected to follow Newtonian behavior, where any stress is proportional to the rate of change of strain[31] or by a force which is proportional to velocity of flow. The

parameter which governs such behavior is the inherent property of the fluid called viscosity [μ][31,32]. Size and shape of molecules in the fluid and their interaction defines the viscosity. When a fluid is forced through micro/nano channels, it generally moves faster along the axis and flow is usually very slow near the wall due to net increase in the viscosity [wall interaction] and surface tension. Normally, external forces [pressure difference, gravity, electric field etc] can overcome the friction between two layers. Sometimes viscosity of the fluid varies with stress or by chemical reaction, which is described by non-Newtonian flow.

1.11 Fluid flow by capillary action

Surface interaction of wall and the fluid, which prominently control the flow, is influenced by surface tension [γ][31,32]. It is defined as the Gibbs free energy per area at particular temperature and pressure [p]. Physical origin of surface tension is due to a net inward force on the surface molecule by intermolecular forces and result is a minimized surface area. When the adhesive interactions [solid-liquid] are much more than the cohesive interactions, the fluid tries to flow by capillary action in narrow channels. To maintain equilibrium between normal forces and surface tension forces, the fluid surface tries to arrange in a curved geometry, which can be visualized on an interface between air and liquid phase [Figure 1.3]. Pressure difference of a free fluid contact with air and a smaller channels can be determined by Young- Laplace[31,32] equation 1.8. Length of channels filled by a free fluid is determined by the pressure difference and from Young-Laplace equation, it increases for smaller nanochannels[31,32] and also with surface tension.

$$\Delta p = \frac{2\gamma}{R} \qquad \textbf{(1.8)}$$

Molecular interaction of fluid with any surface can understood by contact angle[31,32] measurement, which is defined as an angle between solid-liquid and liquid-gas interface. For narrow channels, a fluid having surfaces with contact angle less than 90˚ [concave meniscus] is referred as hydrophilic surface[32] and greater than 90˚[convex meniscus] is known as hydrophobic surface[32]. In our nanofabrication process of CdS nanotubes, the aqueous electrolytes have hydrophilic interaction with porous alumina.

1.12 Horizontal fluid flow

As discussed in earlier, pressure difference across a thin horizontal channel[32] determines the speed of filling process. Fluids can filled faster in horizontal nanochannels by creating a pressure difference [liquid height or by applied forces]. Pressure drop at any particular point for a horizontal flow can be calculated from Hagen-Poiseuille[32] equation 1.9.

$$\frac{dp}{dx} = \frac{8\mu}{R^2}\frac{dx}{dt} \tag{1.9}$$

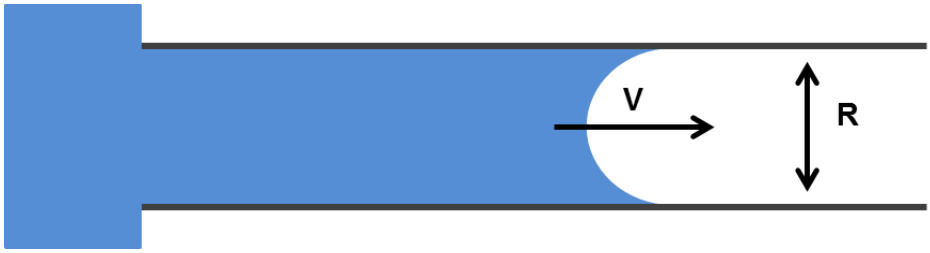

Figure 1.3: A simple fluid flow with velocity v in a horizontally placed nanochannel of radius R.

1.13 Types of fluid flow

Fluid flow can be classified into laminar, transitional and turbulent[31]. Usually in a viscous force dominated flow, layers of the fluid move in an orderly and linear fashion and such flow is called as laminar flow. In the case of turbulent flow, particles move in a random way and most importantly, a small perturbation is enough to disturb the motion which can lead to unstable flow movements. Any intermediate behavior between laminar and turbulent motion is called a transitional flow. In classical fluid dynamics, most of these flows can be identified using Reynolds number [Re][31,32], which is defined as the ratio of inertial forces to the surface forces.

$$Re = \frac{\rho v L}{\mu} \quad \textbf{(1.10)}$$

In general, laminar flow is observed for Reynolds number less than ~2300 and it became turbulent when it overcomes the limit 4200. For a fluid flow through microchannel[31] with diameter [L] 100 μm and speed [v] 100 μm/s, Reynolds number is estimated to be around Re = 0.01. Similarly for smaller nanochannels of porous alumina the flow is laminar. Only way to achieve turbulent regime in these smaller nanochannels is by having a large pressure gradient or velocity as in equation 1.9. Later we will argue that such unstable flow can be perturbed by possible chemo-hydrodynamic reactions during a nanofabrication process.

1.14 Transport of ions in nanochannels

1.14.1 Role of surface charge

Usually the surface charge density of inorganic membranes is determined by the isoelectric point[33,34] and pH of the electrolyte. In general, electrolyte with pH above isoelectric point result in negative surface charges whereas in the other case with a pH less than isoelectric pont leads to positive charges on the surface. Isoelectric point of a material mainly depends on the interaction of electrolyte molecules with nanochannel surface. In the case of aqueous solution, reaction of OH^- and H^+ with the surface determines the isoelectric point and there by the surface charge density. It can vary with different types of electrolyte used in membrane or nanochannels made of same inorganic compound. In the case of porous alumina[33], isoelectric point is around 8-9.

1.14.2 Role of electric double layer

In some cases surface charge developed inside the nanochannels control the flow of ions by internal electric forces[31,32]. For an electrolyte in contact with nanochannels, counter ions with opposite charge are attracted toward surface charges [figure 1.4], which can further initiate to create a region of net charge called as electric double layer [EDL][32-37]. These regions have an immobile layer of counter ions attached to the surface charge [stern layer] and a mobile layer of

ions [diffusive or Gouy-Chapman layer]. Stern layer and the diffusive layer together constitute the EDL. Surface charges are usually estimated using Zeta potential and this parameter is defined as the potential difference between immobile layer and solid surface. We can understand the behavior of ionic flow through smaller nanochannels using Poisson-Boltzmann[32] distribution equation 1.11.

$$\nabla^2\varphi = \frac{-\rho}{\varepsilon} = \frac{-e}{\varepsilon}\sum_{i=n} Z_i n_i^0 exp(-\frac{Z_i e\varphi}{K_B T}) \quad \textbf{(1.11)}$$

Where φ is the potential distribution, Z is the charge valence of the ion, n is the bulk concentration and $\varepsilon = \varepsilon_0\varepsilon_r$ is the dielectric constant of the ionic solution. The simplified potential distribution for symmetric electrolyte[32] through smaller nanochannels is given by the equation 1.12.

$$\varphi^* = \zeta^* \exp(-\frac{y}{\lambda_D}) \quad \textbf{(1.12)}$$

Where both $\varphi^* = e\varphi/K_BT$ and ζ^* is the dimensionless potential and zeta potential respectively, y is the distance from the surface of nanochannels and Debye length [λ_D] is the distance from the surface to some point where the potential difference goes to zero. For a monovalent ion the Debye length[32] is given by,

$$\lambda_D = \sqrt{\frac{\varepsilon_r \varepsilon_0 K_B T}{2nZ^2 e^2}}. \quad \textbf{(1.13)}$$

Where ε_r the relative permittivity of an ionic fluid, ε_0 is the dielectric constant of vacuum, K_B is the Boltzmann constant, e is the electronic charge, T is the temperature in kelvin and others mentioned above. Equation 1.13 can be used to estimate Debye length for a 0.1M concentration of monovalent ions and it is found to be less than 1 nm. Significant role of surface charges on this ionic motion can only result if the diameter of the channels is as small as the Debye length of an electric double layer. For example, in the case of porous alumina nanochannels having diameter 20-100 nm and 0.1M monovalent ionic concentration, net bulk charge inside the

channel is practically zero. However for smaller nanochannels and at dilute concentrations, there can be a net variation of charge inside the channel as shown in figure 1.4.

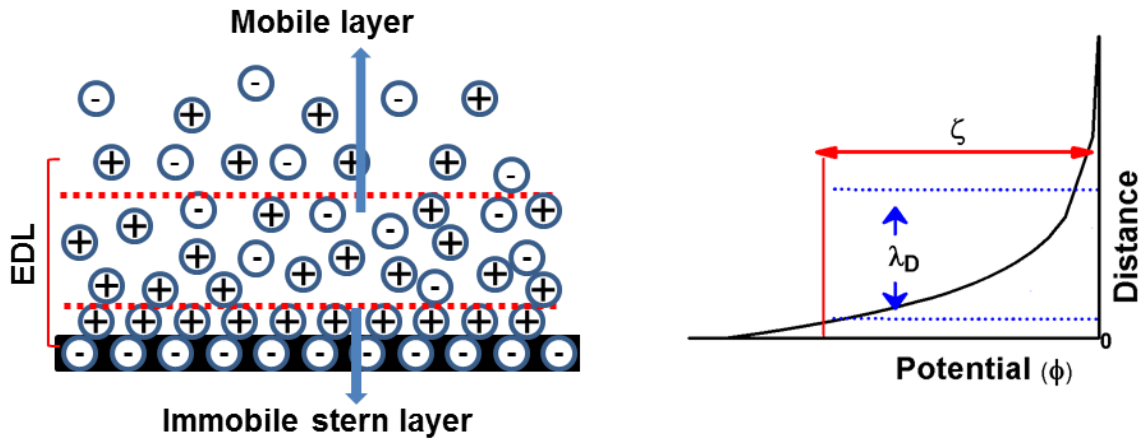

Figure 1.4: Charge distribution of an ionic solution inside a charged nanochannel surface[32]. And also shows the Debye length [λ_D], where the potential goes to zero.

1.14.3 Nanofluidics

In general, usual nanofluidic regime begins when the size of nanochannel become comparable to Debye length of electrolyte used. This will result in a selective flow of counter ion with opposite charge to the surface and preventing the flow of co-ions [figure 1.5]. Nanofluidic behavior of ionic transport can be observed in nanochannels with diameter of 100 nm and for a dilute concentration (< 1mM) of electrolyte. Surface charge density also plays an important role in such type of ion selective flow. Our synthesis environment is much beyond this classical nanofluidic regime, and we will neglect the role of nanofluidics and electric double layer particularly in nanofabrication process of cadmium sulfide nanotubes using porous alumina nanochannels.

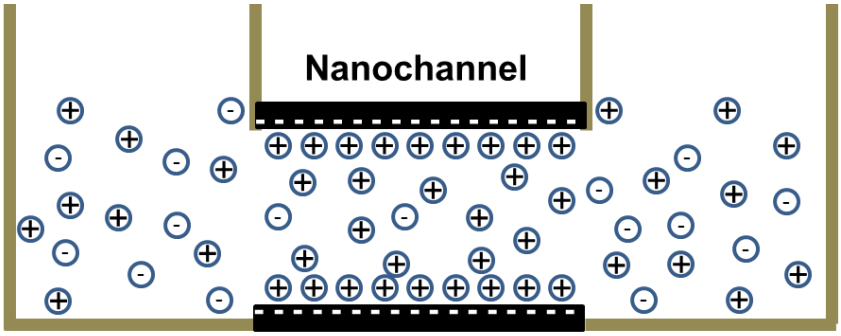

Figure 1.5: Transport of ions through a nanochannel in nanofluidic regime. Only charges opposite to channel surface charges are allowed to pass.

1.15 Hydrodynamics in nanochannels: Mixing of ions

1.15.1 Diffusion and Fick's law

Random motion of molecules[31,32] in a fluid is viewed as diffusion. Overall speed of this random molecular motion through smaller nanochannels is determined by its diffusion coefficient[32] [D] as in equation 1.14, which can also affected by surface forces. Smaller ions with high diffusion coefficient move quickly through nanochannels as compared to bigger ones. Concentration gradient [dc/dx] on an interface or across nanochannels can also add to the diffusive motion. Flux of ion [j] passing through nanochannels can be estimated with the use of Fick's law [equation 1.15] [31,32]. Later on we will use Fick's equation to determine the flow rate of cadmium and sulfur ions through nanochannels of porous alumina.

$$D = \frac{K_B T}{6\pi\mu R} \tag{1.14}$$

$$j = -D\frac{dc}{dx} \tag{1.15}$$

1.15.2 Fluid mixing process

In bulk, fluids can mix together by advection and also by concentration gradient of ions [diffusion], which is together called as convection[31,32] process. This inherent nature of fluid to mix together with surrounding fluid or chemicals[31,32,38] is known as passive mixing. Advection is prominent for enhancing the mixing of fluid at a scale much above micro dimensions. For a scale much below the micro scale (nano and microchannels), where the surface forces are dominant, mixing of fluids are expected to govern by the diffusion process only. In these smaller nano or microchannels, the mixing is very slow and can enhance only by external pressure differences or by other forces. This forced process is known as active mixing. However, we will see later that diffusion controlled flow alone cannot explain all aspects [say growth rate] of nanofabrication and self-assembly of ligand free CdS nanotubes.

1.15.3 Dimensionless numbers to understand the fluid mixing process

Usually in classical fluid dynamics, mixing process of fluids is scaled by dimensionless Peclet number [Pe] [equation 1.16][31,32], which is defined as ratio between advection and diffusion time scale. This usually predict a diffusion dominant mixing process in smaller dimension and also from equation 1.16, it is clear that Peclet number reduces with size [L] or ions having high diffusion constant. To understand the mixing process in microchannels of length L=100 μm, we estimated the Peclet number for a simple metal ion flow with a velocity [v] 100 μm/s and the estimated value is around 0.01 or it can go even less.

$$Pe = \frac{Diffusion\ time}{Advection\ time} = \frac{L^2/D}{L/v} = \frac{Lv}{D} \qquad \textbf{(1.16)}$$

Normally, we can observe an advection dominant process in mixing only if the Peclet number reaches much above 100 and this can vary upon different conditions. This will clearly support the diffusion dominant mixing at such small length scales. Only way to enhance mixing in these nanochannels are by a strong external forces [e.g. pressure gradient, high electric field or strong chemical reaction] applied to the system to initiate such advection process. This can lead

to turbulence[32] in narrow channels which are not commonly observed in a fluid flow at small length scales.

1.15.4 Active mixing

One way to mix fluids efficiently and thereby increasing the reaction rate of chemicals in nanochannels or microchannels is by advection process[38]. However in nanochannels, it is usually difficult to achieve a dominant advection process for fluid mixing. Usually for a viscous dominated flow (low Re Number), it is classically difficult to develop turbulence and instability in nanochannels and micro channels. But external parameters like pressure gradient, high electric field and fluids with different density and chemo-hydrodynamic disturbances may create forced fluid motion. One can observe a destabilized interface between two fluids when they come to contact with each other having significant variation in interfacial tension, pressure gradient and concentration. These can create regions of instability of hydrodynamic origin, usually observed for flows with high Reynolds number or in an interface of two different fluids with variation in viscosity like two of our aqueous reagents used to make CdS. In general, it is not impossible to observe instability at interface[39-45] having large variation of viscosity, density gradients, concentration gradient, surface tension, under high electric field [nanochannels], pressure gradient etc. In this thesis, we will ultimately try to explore whether nanoconfined motion of two reactant fluids indeed give rise to similar chemo-hydrodynamic perturbation due to local variation of temperature and concentrations.

1.16 Types of hydrodynamic instabilities

1.16.1 Marangoni instability

Temperature or concentration gradient can create surface tension gradients in aqueous solutions and this can generates strong perturbation of fluid motion across the gas-fluid interface

due to interfacial instability of particular kind known as Marangoni instability[39]. Particles or fluids located in low surface tension [high temp] region is pushed towards a region having higher surface tension [low temperature], which mainly occurs across interfaces with a gradient of temperature. This process of replacing fluids become continuous and get amplified giving rise to instability. Simple visualization of this particular instability is a pattern formation of convection cells[39,46,47] as seen in figure 1.6 by evaporation of liquid from a free surface. All the above process is a competition between surface tension gradient and viscous forces which will determine the nature of convective flow and instability. These two forces are related through a dimensionless numbers called Marangoni number [M][equation 1.17], which can predict a possibility of such instability. For a threshold critical value[46-50] above M = 80, where the tension gradient forces dominate over the viscous forces the onset of instability begins. It is usually very difficult to observe Marangoni instability much below 80, where viscous forces dominate over tension gradient forces. So it is usually very difficult to observe this type of instability in viscous dominated flows through nanochannels or even with surface gradient tensions.

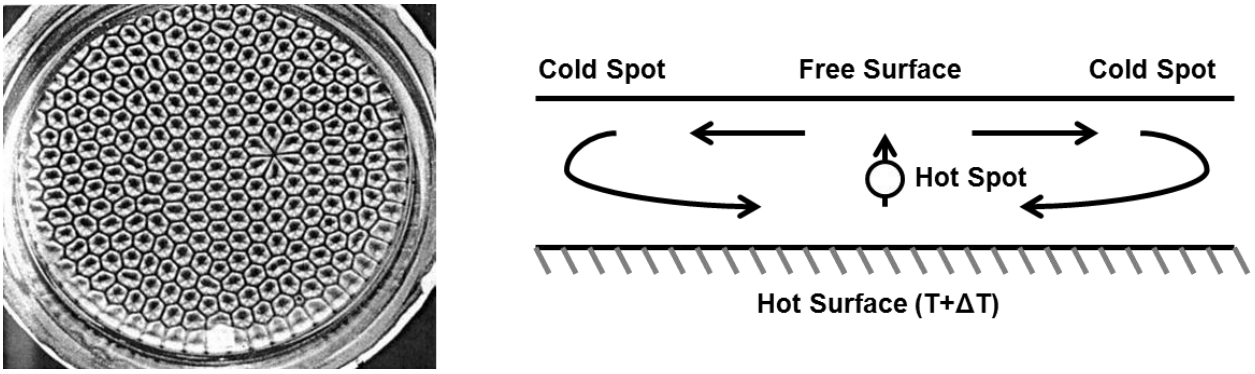

Figure 1.6: Pattern formation by Marangoni instability occurs during evaporation process is shown in the left hand side and the fluid flow under tension gradient on the interface is shown in the right side. This famous picture is taken from F. charu, Hydrodynamic Instabilities[39].

Thermal Marangoni [M_{Th}][51] number can be calculated using the equation 1.17, where γ is the surface tension, h is the thickness of fluid, μ is the dynamic viscosity and κ is the thermal diffusivity.

$$M_{Th} = \frac{-\left(\frac{\partial \gamma}{\partial T}\right) h \Delta T}{\mu \kappa} \quad \textbf{(1.17)}$$

Concentration gradient[52,53] can also sustain such type of instability and it is observed as a propagating reaction front in a high concentrated acid-base interface. This convective motion can speed up the reaction rate and also sometimes leads to a self-organization of chemo-hydrodynamic patterns.

1.16.2 Viscous fingering

In a porous media or Hele-shaw cell[39,40,54-57], viscosity gradients can destabilize the interface by the displacement of a high viscous fluid with a less viscous fluid. This instability leads to fingering of patterns across the interface as seen in the figure 1.7 and is influenced by chemical reaction, surface tension gradient and density gradients in a porous medium. For a porous layer of thickness h and width w, the aspect ratio h/w and viscosity ratio determine the width of the fingering[55]. Higher the viscosity differences, more the width of fingering pattern and similarly it increase with thickness or diameter of the system. Usually for immiscible fluids it is easy to predict the shape and width of the fingering but for miscible fluids, we can only predict the fingering tips not the width[41]. In most of the cases stable interface is observed for a displacement of less viscous fluid by a high viscous fluid.

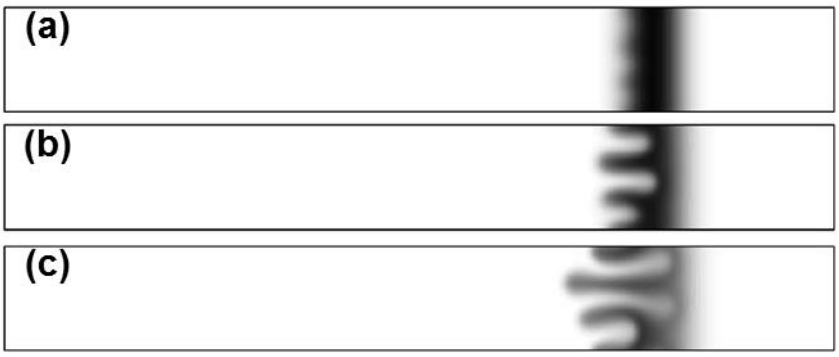

Figure 1.7: Viscous fingering simulation of two miscible fluids with different viscosity. This figure from the top to bottom shows the viscous fingering pattern with time. This is taken from A. De Wit, Miscible viscous fingering with linear adsorption on the porous matrix[57]**.**

1.16.3. Electrokinetic instability

Concentration polarization layer [CPL][45,58] developed on perm selective membrane or nanochannel surface can gives rise to unstable flow at high applied voltage [>10 V]. Instability originated at nanocannel interface due to CPL formation can leads to micro vortices[45,58-61] at high applied voltages. This is experimentally observed from a nonlinear ohmic behavior[61] [I-V] of ionic transport through nanochannels having size equivalent to Debye length. For initial low voltages, ions show ohmic behavior followed by limiting current at moderate voltages and finally at high voltage there is an over limiting current, which shows the signature of instability. Limiting current is mainly due to depletion of counter ions from one side of the membrane. CPL mainly depends on the zeta potential, Debye length and the applied voltage. In the case of small diameter channels with overlapping Debye layer it is possible to create instability at low voltages[60]. Mixing speed of fluids in smaller nanochannels can be enhanced by creation of such micro vortices at high applied electric field.

1.16.4 Chemo-hydrodynamic instability

Coupling of chemical reaction and hydrodynamics at an interface can create a propagating pattern which amplifies with time. This propagating velocity of chemical products cannot simply explained by reaction-diffusion[53] dynamics. Spatial distribution of mass created and heat generated by exothermic reaction changes the viscosity, density and surface tension of the reacting interface and there by an unstable interface. It is important to note that for porous structures the coupling between reaction dynamics and hydrodynamics play an important role for self-organization of nanostructures at the interface. We are trying to understand the role of such chemo-hydrodynamics in nanoscale self-assembly of cadmium sulfide nanotubes.

1.17 Semiconductors

In general, semiconductors are identified by their electrical resistivity which lies in the range ~10^{-2}-10^{9} Ω-cm[62]. Interaction of neighboring atoms of the lattice results in overlapping electron wave functions and there by clustering of closely spaced energy levels widely known as energy band as in the figure 1.8, which is separated by a nominally forbidden region for electrons in an ideal case with an energy gap ranging from fraction of eV to few eV. Upper energy region above the gap is known as conduction band with mostly vacant electron energy levels and lower region below the forbidden gap is called as valence band, where majority of energy levels are filled by electrons at room temperature. Nanostructures of inorganic semiconductor alloys with interesting physical application are from II, III, VI, V group elements in the periodic table[4,63,64]. Some of these compound semiconductors like cadmium sulfide [CdS] tend to crystallize either in zinc blende and wurtzite hexagonal packed crystal structure[64]. Our work is mainly focused on CdS nanotubes, which is a member of II-VI compound semiconductor and crystallizes in any of the above two forms. These II-VI compound semiconductors generally occur in nature as ionic crystal[62,63] with main bonding of atoms are by electrostatic attraction. Presence of more electronegative group VI elements like sulfur makes way for dominant ionic bonding, where as in other compound semiconductors bonding can be partial ionic and partially covalent.

Nanomaterial's of group II-VI semiconductors [eg. CdS, CdSe, CdTe etc] having band gaps in visible spectrum can be a potentially good material for fabricating low cost optical and electronic devices. In general for II-VI semiconductors[65], the electro negative [group VI] element usually forms the valence band and group II elements makes the unoccupied conduction band at 0 K. Intrinsic conductivity of semiconductor is mainly determined by the ratio E_g/K_BT, when this ratio is large, the concentration of free electrons decreases and thereby conductivity. The best method for determining band gap was optical absorption experiments[62,63] of the material from ultraviolet to infrared region [350 nm-1200 nm]. The significant visible absorption at particular frequency [ν] determine the band gap $E = h\nu$. Semiconductors having a conduction band minima and valence band maxima at same energy-momentum [E-k] space point are called direct band

gap semiconductor[62,64] [eg: GaAs, CdS, CdSe]. There direct optical absorption of photon can take place by exciting an electron from valence band maxima to conduction band minima.

In case of indirect absorption, the band extremum of the semiconductor [say Si or Ge] are separated by a finite wave vector k, thus a phonon with less energy as compared to band gap is involved to conserve the momentum and thereby creating electron and hole. These types of semiconductors are called as indirect band gap semiconductors[62] and they need the help of phonons to complete the optical absorption in a two-step process. Therefore, photo absorption as well as light emission in indirect band gap semiconductors is less efficient than those in direct band gap materials.

Photoexcited electrons can relax and recombine with holes to emit a photon with energy equivalent to band gap energy or lesser value. This is generally called as radiative recombination process and shown in figure 1.8. Energy of emitted photon is significantly affected by the presence of empty energy levels near the band edges mainly by impurity or defects in the crystal, which can trap electrons and holes, located in forbidden region and thereby influence the recombination process.

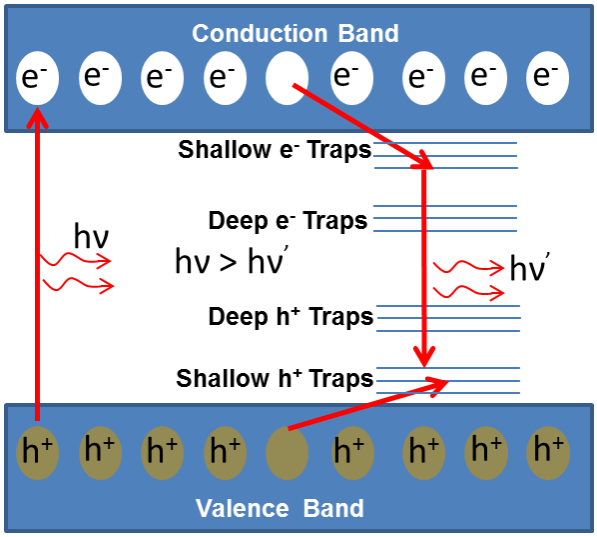

Figure 1.8: Energy band diagram of a Semiconductor. The figure shows excitation of electron from valence band to conduction band by absorption of a photon (hν) and further recombination processes of those excited electrons and holes which subsequently emit a photon of lesser energy (hν').

In general, defects as a departure from ideal periodic arrangements in crystals occur mainly as point defects and line defects[63]. Point defects are created by isolated atom or vacancy in the crystal and line defects have contribution from row of atoms [e.g dislocations]. One of the most common point defect[63] occurs in a crystal by a missing atom with some intrinsic charge is widely known as vacancy. Other types of point defects are mainly from the atoms located on interstitial sites and Frenkel defects which are formed by pairing of vacancy and interstitial atom. Vacancy in semiconductor crystal is intrinsic in nature and defects created by impurity or foreign atoms are extrinsic in nature. The energy levels of these defects lies in the forbidden region of the semiconductor as shown in figure 1.8. Defect states with energy level close to either valence or conduction band behave like shallow traps for holes and electrons. Deep trap states are located at the middle of the band gap region. These types of defects are commonly observed in almost all semiconductors.

1.18 Cadmium sulfide

Cadmium sulfide (CdS) is a direct band gap semiconductor[62,64] with direct electronic transition possible from valence band maxima to conduction band minima. High quality crystalline CdS with excellent photoluminescence and charge transport properties have potential applications and widely used for fabricating window layer for solar cells[12,13,66], nano-lasers[2,67,68], light emitting diodes[2] etc. In nature, CdS occur as either wurtzite [W] or zinc blende [ZB] crystal structure[63,64]. Most stable form of CdS in bulk state was wurtzite due to its reduced energy per atom [fraction of meV] as compared to ZB structure[69-71]. Under certain external thermodynamic condition[69] both structure can transform into each other as the energy difference is small. Standard lattice constant[64] values for WZ CdS are a=b=4.1A, c=6.7A and similarly for ZB CdS where all lattice constant are equal in size with a=b=c=5.8A.

Cadmium sulfide nanostructures are mainly grown from the precursors containing S^{-2} and Cd^{+2} ions[72-75] during wet chemical synthesis. The outermost electronic energy levels of Cd and S which took part in forming the energy bands of CdS are shown in figure 1.9. These are configured as[76,77] $4d^{10}5s^2$ and $3s^23p^4$ respectively. The middle regions of valence band have

mainly contribution[76] from the Cd 4d orbital with small mixing of 3s and 3p, whereas the top valence band is mainly from the S 3p state. The conduction band which lies above the Fermi level have main contribution from the Cd 5s energy state with non-negligible mixing of S 3p states. From experimental and theoretical calculation the band gap for the both crystalline phases are close to each other. Fundamental bulk band gap for these two crystalline phases WZ and ZB are 2.41 and 2.5 eV respectively[78]. Normally the band gap of CdS is determined from optical absorption spectroscopy.

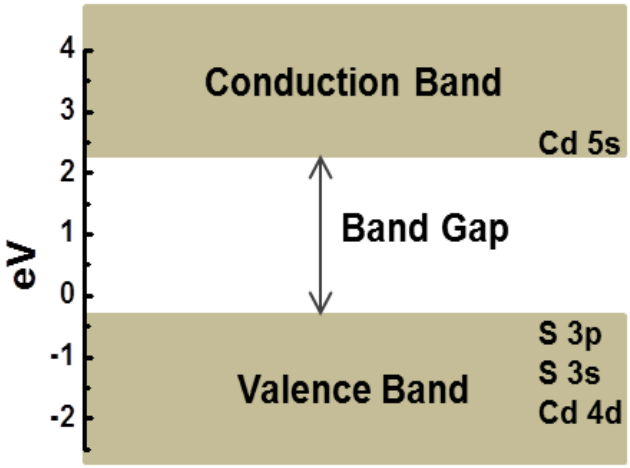

Figure 1.9: Shows the energy band diagram of CdS with individual contribution from Cd and S orbitals. Left side shows approximate energy scale of CB and VB with respect to NHE[76].

1.19 Electronic and optical properties of CdS

Presence of defects, strain, excitons and quantum confinement in CdS can result in novel electronic and optical properties. CdS with a predominant sulfur deficiency[79-81] behave like an n type semiconductor whereas it is extreme difficult to make highly conductivity p-type CdS. Recombination of electrons and hole at the conduction band minimum and valence band maximum is known as band edge emission. Extra energies gained by electrons in the conduction band are lost by non-radiative decay through lattice phonon interaction. Coulomb interaction of

electrons in the conduction band and the holes in the valence band result in formation of bound state named exciton, which creates extra energy levels below the conduction band. Various defect levels in the forbidden region of CdS can act as traps for the electron and holes and there by reduces the energy of emission by recombination.

Photoluminescence properties of CdS are widely influenced by inherent defects and its nature. Most of the defects in the CdS act as a radiative or non-radiative trap centers for the exited electrons and holes and thereby cause red shifting of emission peak from the absorption maximum[63,77,82]. Most abundant defects in CdS are due to vacancy of the lattice atoms or interstitial atoms of the constituent compound. In the case of any nanoparticles, main contribution of defects is from surface due to missing atoms or dangling band which act as trap states for excited charge carriers. CdS grown from Cd or S rich condition can give rise to S or Cd vacancy or excess atoms located on interstitial sites. Such defects can be identified from the presence of extra peak or broadened nature of the photoluminescence spectra[63,83]. These types of defects in CdS are generally treated as deep[63] traps with energy level close to the middle of the forbidden band region. Experimental and theoretical studies are done on these defect state energy levels and found out that optical emission from CdS mainly consists of - (i) a green emission band[83-86] [due to excitonic emission, shallow traps, band edge emission etc] around 2.38 eV-2.55 eV, (ii) a yellow emission band[82] around 2.0 eV-2.2 eV and (ii) a red emission band[87] [due to deep defects] around 1.7 eV-1.9 eV. Typically for CdS nanostructures, defects levels in sub band gap regions are originated from some stoichiometric imbalance in alloy composition. One is - (a) sulfur vacancy[88-92] [or excess cadmium in the form of Cd interstitial donor levels] state which is located within 0.4 eV-0.7 eV below the conduction band edge and the other is - (b) from cadmium vacancy states[93] which is found around 1.2 eV above the valence band edge. Position of the energy levels of some defects is shown in figure 1.10.

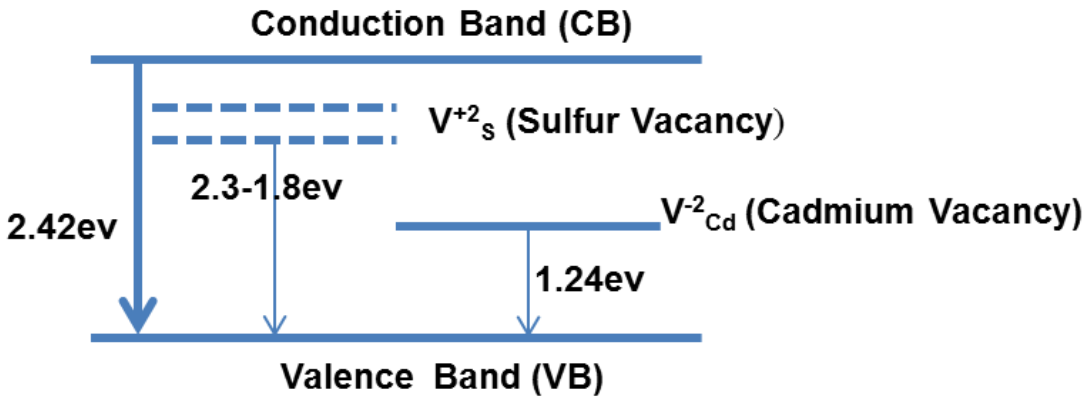

Figure 1.10: Typical photoluminescence process of CdS in the presence of various intrinsic defects.

1.20 Optical process in nanostructures

Quantum confinement effect becomes dominant when the size of CdS nanocrystal reduces to Bohr exciton radius[86,94,95] [3 nm] such that excited electron and holes form a hydrogen atom like bound state named exciton inside a semiconductor material. This lead to discreet energy levels and such formations are generally visible by resonant peak like feature in the optical absorption spectra of such materials. A sharp well-formed resonant peak provides a testimony to the good optical quality of the material. Size dependence of such peak is observed by blue shift in absorption spectrum which results from a net increase in the band gap due to quantum confinement effects. Another factor which control optical process in nanostructures is surface effects. As particle size decreases, most of the atoms are located near to the surface. The optical processes which are very important for application are therefore easily affected by electronic defects introduced by surface states. Experimental and theoretical observations have shown that defect states located at the surface play an important role in optical emission and there by affecting the efficiency of the optical process. Photoluminescence can be quenched in a nanocrystal by non-radiative process. Most of the defects at surface are usually passivated by

ligands/capping agents and thereby neutralizing such defects[96-98], which enhances the photoluminescence.

Depending on the size of CdS nanotubes or nanowires, quantum confinement of charge carriers along two spatial directions and high percentage of surface atoms influence the optical properties. These types of structures can be fabricated by different types of nanofabrication methods. Growth process can be influenced additionally by the effect of strain[98] in these nanostructures which will play an important role in shifting the position of lattices from the ideal one and thereby the optical process it undergoes when excited. These nanotubes or nanowires are efficient models to study the strain effects on band position, defect energy levels and finally band gap. In general Strain[98-102] can be originated by both compression and elongation [tensile] in these structures during the growth process or by bending of nanowires by external forces. Compressive strain can increase the band gap[99] and in case of tensile strain it is the opposite. Strain can also shift the PL peak systematically but in the real case it is difficult to separate effects of strain from all the other process which is involved in optical emission process. In the last part of the thesis, we will be trying to understand the role of inbuilt electronic defects and strain during growth nucleation of ligand free nanotubes for shifting the photoluminescence peak with varying diameter and length.

1.21 Outline of the thesis

This thesis is mainly focused on two related studies: In the first part [chapter 2-4], it contains a description of a novel nanofabrication process of ligand free cadmium sulfide nanotubes using nanochannels of porous alumina as nanoreactors and further investigations towards the chemo-hydrodynamical origin of nanoscale self-assembly. Finally the other part [chapter 5-6] is devoted on the role of crystalline strain and electronic defects in photoluminescence process of these ligand free CdS nanotubes as a consequence of such nanoscale growth process.

In the next **chapter 2**, we will discuss the concerned nanofabrication route and experimental techniques used in the studies in detail. Fabrication process includes synthesis of

porous alumina nanochannels and using these as nanoreactors to study the nanotubular self-assembly of ligand free CdS. We will briefly explain the working principle of instrumental techniques like Scanning electron microscopy, X-ray diffraction, UV-Visible Spectrophotometer etc in this chapter. Necessary analysis procedures required to understand the optical absorption and photoluminescence measurements are discussed there. We will also discuss the estimation of crystalline size and micro strain using x-ray diffraction spectra to understand the role of in-built stain and defects in photoluminescence spectroscopy of CdS nanotubes.

In **chapter 3**, we will describe directionally asymmetric self-assembly of CdS nanotubes on one side of porous alumina template using a home built two-chamber fabrication setup. Possible reasons for such one sided growth are discussed in this chapter. Nucleation sites for CdS nanotubes are identified from scanning electron microscopy images and further used for understanding the tubular growth mechanism. The strong exothermic reaction between the reagents within a nanoconfined space can create strong local variation of temperature, reactant concentrations etc. We will also indicate the plausible role of such chemo-hydrodynamic perturbations in such nanotubular growth of CdS.

We will show some more important findings in **chapter 4** to further probe the growth mechanism of CdS nanotubes. Measuring the length of CdS nanotubes using scanning electron microscopy images shows a significant increase in growth rate with increasing growth duration and also with decreasing diameter. We will argue that coupling of nanoscale exothermic chemical reactions and hydrodynamics can create such a chemo-hydrodynamic perturbation which amplifies with time. We indicate that these events cannot be explained by standard diffusion based models. Moreover, our experiments on varying concentration of precursors show the importance of Na_2S concentration in growth process, whereas the other precursor $CdCl_2$ is not influencing the growth elongation that much. Overall these experiments indicate the importance of chemo-hydrodynamically triggered instability during nanofabrication of CdS nanotubes. This also clearly highlights the requirement to study such important issues and the need to quantify the details of growth dynamics even further.

Optical quality of this ligand free CdS nanotubes are investigated in **chapter 5** using photoluminescence measurement. Ligand free CdS nanotubes show enhanced

photoluminescence as compared to CdS nanocrytallites prepared by bulk mixing of the same precursors. We will argue the possible role of directional nature of light emission and reduced non-radiative recombination centers in nanotubes as compared to CdS nanocrystallites for such enhanced photoluminescence as a possible cause for such enhancements.

In **chapter 6**, we will report the role of minority defects and crystalline strain responsible for significant photoluminescence shift from CdS nanotubes with different diameter and length. Our optical absorption and x-ray diffraction studies rules out the possibility of any quantum confinement effect which usually observed for such structures with crystallite size comparable to that of Bohr exciton radius. These as grown CdS nanotubes are prone to inbuilt strain during its typical growth process and thereby create electronic defects which can influence the photoluminescence process. Crystallite size and strain is estimated from powder x-ray diffraction pattern. Estimation of micro strain also shows a systematic increase in inbuilt strain with increase in nanotube size [diameter and length] which subsequently cause the observed photoluminescence red shift. Theoretical density functional calculation also supports this role of cadmium vacancy minority defect [2^{nd} most abundant] in controlling the photoluminescence process as compared to other more abundant defects and how it is affected by crystalline strain. This understanding corroborates our observed photoluminescence shift with varying nanotube diameter and length.

In last **chapter 7**, we will end with a summary of the thesis work with a brief discussion on future research plans.

Chapter 2

Experimental and Characterization Techniques

2.1 Introduction

This chapter gives a brief technical introduction of the nanofabrication process, operating principles of various techniques utilized to probe these nanostructures and also relevant data analysis methods used in this thesis. Most of these experiments are done to understand nanotubular self-assembly of ligand free CdS and the observed shift in photoluminescence peak from these CdS nanotubes having different lengths and diameters. First part of this chapter, section 2.2 & 2.3 has the details of the synthesis procedure for nanoporous alumina membrane and also the nanoreactor based nanofabrication setup used for CdS nanotubular growth. Working principle of field emission scanning electron microscopy used for nanotubular growth studies is described in section 2.4. Optical experiments like absorption and photoluminescence measurements are used to get some information about the material quality, the role of electronic defects and also to identify any size effects. These are discussed in section 2.5 & 2.6. Crystalline size, phase and microstrain are identified using powder x-ray diffraction and it is described in section 2.7.

2.2 Fabrication of porous alumina

Nanochannels of porous alumina [AAO] as shown in figure 1.1 were fabricated using 99.99% aluminum foil having thickness 0.3 mm [from either Merck or Alfa Aesar] by one step and/or two step anodization procedure[22,23]. Two step anodization processes is a time consuming one and reasonably well ordered CdS nanotube can also be grown on porous alumina fabricated by one step anodization process. Aluminum foil was first annealed at 400 - 450˚ C for 4-5 hours to improve the structural ordering of pores as described in section 1.7. Annealed aluminum foils were then cut into small [2.5 cm X 2.5 cm] pieces and then cleaned with ultrasonic bath in

acetone. As discussed in section 1.7, surface roughness of the foil was reduced by electro-polishing in 4:1 mixture of ethanol and perchloric acid at 20 V for 1 minute. After this, a circular portion [1.5 cm^2] of the aluminum foil [figure 2.1 & 2.2] was exposed in acid for anodization process in a K0235 Flat electrochemical cell from Princeton Applied Research. This experimental setup was kept at a temperature of 4-7˚ C inside an ice bath. Appropriate acids and voltages are chosen for making different pore diameters of porous alumina for CdS nanotubular growth and also for other experimental studies in chapter 3 to chapter 6.

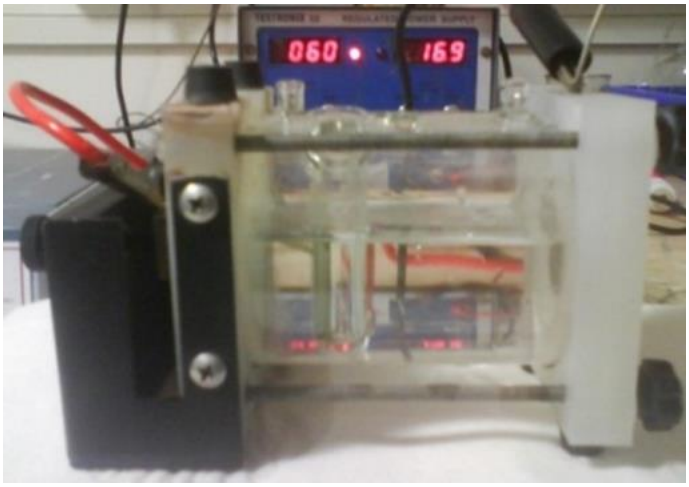

Figure 2.1: Experimental setup used for synthesis of porous alumina.

First step anodization process was carried out in voltages 40, 50 and 60 V in 0.3 M oxalic acid for 12, 5, 2 hours respectively. Pores having smaller diameters were fabricated using 0.3 M sulfuric acid at voltage 18 & 25 V for duration 12 & 5 hours. Anodization duration was optimized for a specific acid and voltage applied to achieve a thickness of 10-30 μm. After first anodization process, back side of the aluminum [1 cm^2] was exposed and etched in saturated $CuCl_2$ solution for a circular and transparent nanochannel membrane having aluminum support along its periphery. This support can be used for holding the membrane inside a teflon O-ring for CdS nanotube fabrication and will be discussed in the next section 2.3. Without a proper support, the membrane usually breaks down due to mechanical stress. Remaining alumina barrier layer was removed by etching with phosphoric acid [5 vol. %] for 1.5 hours and time reduces up to 45 minutes for lesser diameter pores to open the pores at the other end. Figure 2.2 shows the schematic picture of as prepared porous alumina membrane with aluminum support.

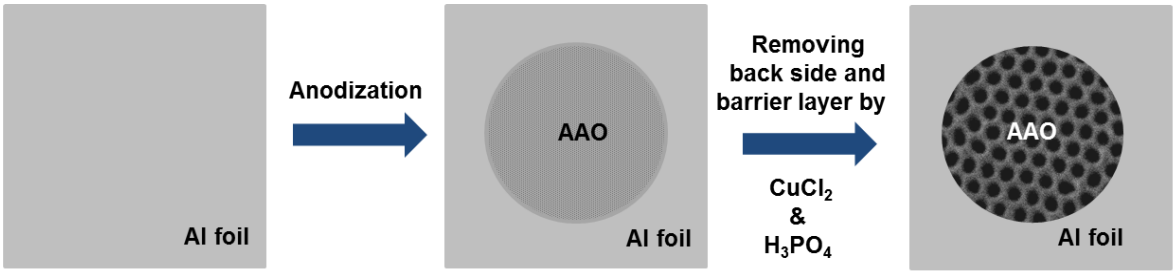

Figure 2.2: Aluminum foil at different stages of anodization process to achieve a transparent AAO membrane. Circular area is anodized porous alumina with Al support.

2.3 Fabrication of CdS Nanotubes

AAO nanochannel membrane with the attached peripheral aluminum support was then used as nanotemplate for synthesizing CdS nanostructures by two chamber synthesis technique[103-108]. First step is to place AAO template between two teflon rings and then clamp this in a two chamber setup as shown in figure 2.3. Precursor solutions of Na_2S and $CdCl_2$ having identical concentrations[109,110] [0.1 M to 0.005 M] in de-ionized water were poured simultaneously into the respective chambers. To maintain an equilibrium pressure on both sides, the solutions were kept at the same height. Time dependent CdS growth varies on the concentration of reactants and also on diameter of pores. This can be directly visualized by a transition from yellowish to orange tinge of CdS on the transparent AAO membrane. No additional surfactants or capping agents were used in this synthesis. After the synthesis, sample was taken out and washed thoroughly in de-ionized water to remove any residual byproducts for further characterizations. We call this method as '*nanoreactor'* based synthesis of CdS nanotubes.

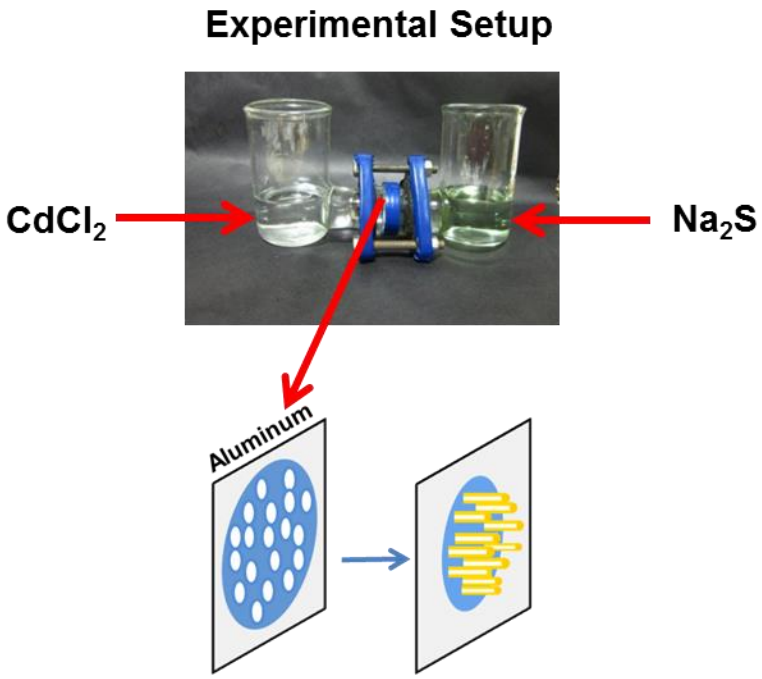

Figure 2.3: Experimental set up used for investigating the growth of CdS nanotubes on porous alumina.

2.4 Scanning electron microscopy

2.4.1 Working principle

Scanning electron microscopy [SEM][111] is one of the most important tools used for imaging nanostructures. Interaction of incident electron with the nanoscale matter can provide lots of extra information like chemical composition, lattice constant etc. Working principle of SEM[111] is similar to optical microscopy. Instead of a light source in optical microscope, SEM uses a focused electron beam to illuminate the sample with the help of electromagnetic lenses for imaging smaller features in micrometer and nanometer length scales. After interacting with the material, the reflected electron beam is collected by various detectors for imaging and analyzing the material composition. To observe high resolution images and also for various scientific analyses, electron beam is accelerated to a high voltage [1-30 kV]. Such high voltages yield

smaller wavelength of incident electrons which allows for better spatial resolution than light microscopy.

Electron can interact with a material[111-113] mainly by two ways; one is elastic scattering interaction with atoms without any energy loss and also by inelastic interactions with a significant energy loss of electrons. Elastic scattering of electrons occurs by nucleus of the atoms and also by outer electrons having similar energy, which can deflect its path. Electrons deflected by an angle more than 90˚ is known as back scattered electrons [BSE] and have valuable information about the material. High energy incident electrons can excite electrons to higher levels within an atom by inelastic interaction and also produces secondary electrons [SE] which is finally used for surface imaging. All these type of inelastic scattering also produce characteristic x-rays for determining elemental composition known as Energy Dispersive X-ray Spectroscopy [EDS] and luminescence known as Cathodoluminescence.

Every electron microscope[111-113] has an electron source, condenser lens, objective lens and detectors as shown in the figure 2.4. Electron gun can emit a continuous stream of electron beam. Along with electron focusing lens and electron optics, these gun columns produce electron beams having high stability, high electron current, small spot size and less energy spread. Typical electron sources are made from tungsten filament which has a work function of 4.5 eV and emit electrons at higher temperature. Filament is heated by applying higher current and the electron can escape from the surface. Modern SEM uses filament made of lanthanum hexaboride [LaB_6] which has a lesser work function [~2.4 eV] as compared to the conventional tungsten filament. LaB_6 can give a better electron emission and less energy spread for better high resolution images. These thermionic sources of electrons depend on the temperature used to overcome the work function of the metal. Even though these metals are inexpensive and can work in low vacuums, the energy spread, life time and low brightness makes a disadvantage for some applications. In modern electron microscopes, field emission gun [FEG] is used instead of a thermionic one for high resolution images. In general FEG can be of three types, one is cold emission gun which operates at room temperature, second one is thermally aided field emission gun and other one which is made from a very sharp tungsten filament tip coated with zirconium and electrons are drawn by Schottky field emission while the filament is kept at high temperature. These Schottky emitters are used in modern field emission electron microscopy.

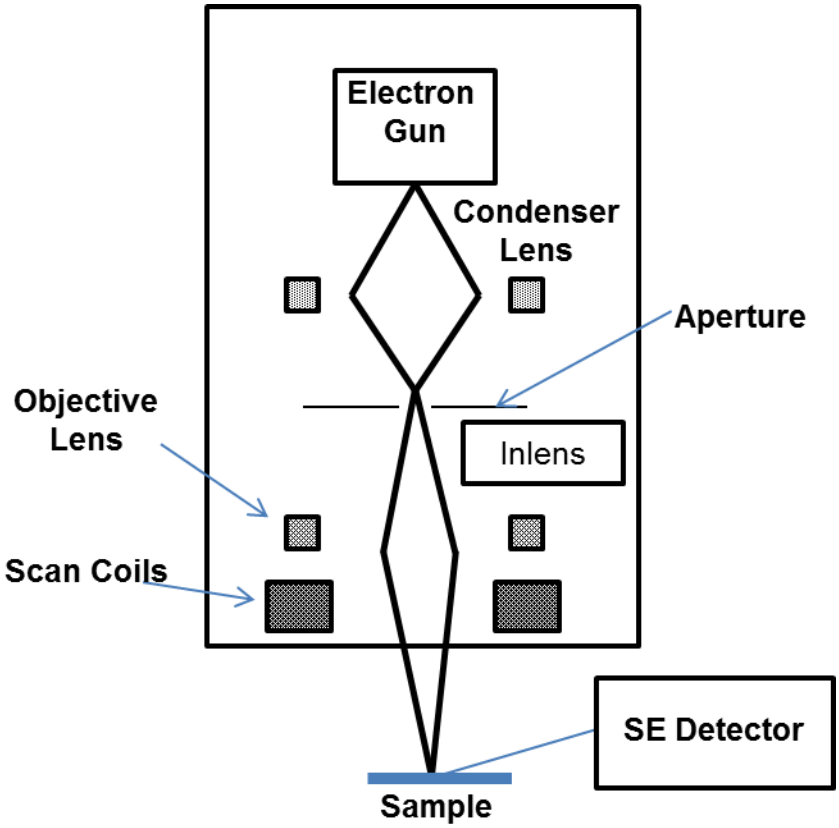

Figure 2.4: Schematic diagram of scanning electron microscope[112].

Electron trajectory is controlled by electrostatic and magnetic lenses in the SEM[111-113]. Even though the magnetic lens has higher abbreviations as compared to optical lenses but it is still better for achieving good resolutions. These electromagnetic lens focus the electron beam by combined effects of electrostatic and magnetic field. Focal distance can be changed by varying the current and thereby the magnetic field in the coil. After passing through anode the electrons get deviated from its path and the beam is converged into a parallel one with the help of condenser lenses which is located beyond the electron source. This has two circular iron pieces wounded by copper wires which will provide the magnetic field and the beam is passed through the center of the two pole pieces. Focus of the beam is adjusted by controlling the current through the condenser coils. An aperture is used to exclude the unwanted inhomogeneous and scattered electrons. Position of aperture is below the focal point of the condenser lens.

As seen from figure 2.4, main function of another objective lens is to converge and focus the electron beam which is diverged below the aperture[111-113]. The beam diameter [spot size] is determined by the choice of demagnification of lens and also the aperture size. Electron beam diameter of our Carl Zeiss ULTRA PLUS FESEM can go to less than 1 nm for high resolution images. As the aperture size increases from 10 µm to 100 µm the current also increase [pA to nA] which will also affect the resolution. The high resolution SEM images shown in this thesis were taken with aperture size 30 µm and accelerating voltage of 5 to 20 KV.

At higher magnifications, lens defects cause the beam cross section to vary in different shape and this effect is known as astigmatism[111-113]. Magnetic field variation in x-y plane due to inhomogeneous pole pieces affects the motion of the electron. Electron beam experiences different focal power on the same x-y plane and in ideal cases all the electrons are to be focused on a same probe point. Astigmatism effect can easily identify from a high resolution image, where the image size [nm] can be visualized by a stretching effect in one direction for example like an elliptical one. In electron optics, this effect is corrected by stigmator made from weak electrostatic quadrupole lenses. By adjusting the four potential of four electrodes through X and Y stigmator, the two focal point F_x and F_y can brought to a single point and thereby stretching in both direction can minimized for a better image. Normally stigmator is not required for low magnification images.

2.4.2 Depth of focus

Samples can have irregular surface geometry and features with sizes from nm to few µm and in such cases it requires a better depth of focus for high quality images. Depth of the focus[111,112] of an SEM can be affected by parameters like beam energy spread, lens current, aperture size, working distance [WD] and chromatic aberration of electron lenses. Focus depth is also dependent on the beam convergences angle and the beam spot size. As the beam convergence angle is reduced, the depth of the focus is improved. This can be achieved by increasing working distance between the sample and lower point of the gun. But in case of less working distance, the beam convergence angle is higher and spot size is also significantly changed. Typical way to increase the depth of focus is to reduce the aperture size, which further

reduces the converging angle and thereby the current. This will finally lead to lesser current and thereby reduced signals as a result of lesser interaction of electron with matter. Therefore optimized values are chosen for better resolution and also for depth of focus.

2.4.3 Scanning of image

Imaging process is done with the help of point by point scanning of the area of interest by the incident electron beam[111-113]. Signals from the single spot interaction of electron beam is collected by using a detector and for a full image the beam spot is scanned across the whole area. This is achieved by a scanning coil which can deflect the electron beam spot along x and y axis, and whole process is known as a raster scanning and causes the beam to cover a rectangular area of the specimen. Magnification of the image is defined as the ratio x, y scan distance on the specimen and the scan distance on displayed image[112].

2.4.4 Electron accelerating voltage and penetration depth

Sample penetration depth depends on the energy of the electrons. Distance that an electron[111-113] can penetrate within a material mainly depends on the accelerating voltage and the composition of the matter. Kinetic energy of the electrons is reduced while passing through a material and finally come to a rest position below a certain depth from the surface known as penetration depth. Interaction volume of the sample where the elastic and inelastic scattering of electrons occurs is shown in the figure 2.5. This volume of interaction is very small for low voltages and also with higher atomic elements of the sample. One of the main reasons for this is due to backward elastic scattering, which is proportional to the atomic mass [Z] and thereby reducing the forward motion of the electrons. Average penetration depth for an electron beam with 5, 10 and 20 KV accelerating voltage used for imaging and elemental analysis lies in the range 500 nm to 5 µm.

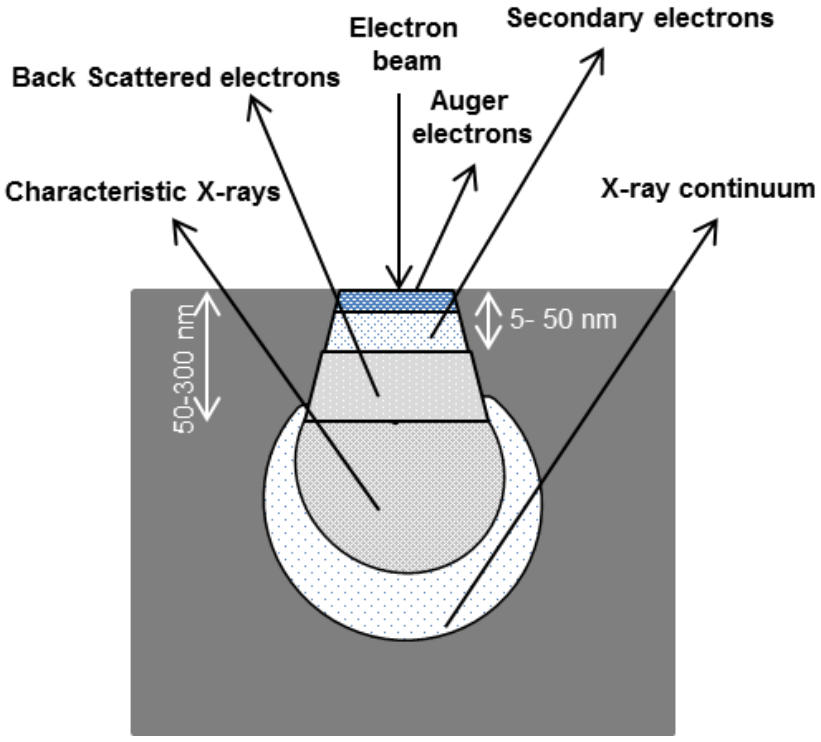

Figure 2.5: Shows the interaction volume of the electron beam on a sample and also the regions from the variety of signals generated by interaction[111].

2.4.5 Detection of signals

As shown in the above figure, the interaction of electrons produce a lot of signals due to back scattered electrons [BSE], secondary electrons [SE], characteristic x-rays and auger electrons etc. Most of the Secondary electrons having energy of the order 100 eV are rested in the interaction volume itself. Only SE electrons which are generated within a 1 - 3 nm depth from the sample can escape from the material and can be detected for a better resolution of surface topography[111-113]. Contrast difference visible on the image depends on the intensity of SE signals from the interaction area. Atoms with higher atomic numbers can produce more SE electrons and thereby increase the contrast in the SEM images. Number of electrons escaping from the surface after bombardment by the primary beam is known as secondary electron yield and it is in the range 0.1 to 10, which also depend on the energy of the electron and the chemical composition. This yield is less for an electron beam incident perpendicular to the surface[112] due

to its reduced escape volume and it increases for an incident angle. BSE are detected by scintillator/photomultiplier (PMT) detector and secondary electrons are detected by Everhart and Thornley detector and characteristic x-rays are detected by the EDS detector[111-113]. In this thesis, the high resolution images of CdS nanotubes described in next few chapters was taken mainly using SE detectors.

2.4.6 Secondary electron detector

Strong signal can be detected by using the Everhart - Thornley detector[111-113] named after the scientist who had designed it for modern SEM. This detector have three parts, one is a scintillator which will collect the SE electrons by applying a few hundred volts for energizing the electrons for sufficient light emission. After that the light is collected through a pipe which is placed inside the chamber and finally this light is collected by PMT tube placed outside the chamber for imaging. In our instrument this detector is known as SE2 detector and the sample is placed at a working distance of above 5 mm to get better images. This detector is placed on one side of the chamber and surface of sample, which is facing the detector have more signals with higher contrast as compared to other side. For surfaces like vertical nanowires arrays grown on substrates, the quality of images can be improved by optimizing the voltage and current.

One more detector known as Inlens [In-column secondary electron] detector[111,112] is used for high resolution images. Secondary electrons generated close to beam axis have elliptical trajectories with a radius more than the incoming electron and BSE traveling on the beams axis are collected by this detector. Inlens can be used for detecting the SE signal from the sample which is lying close to the magnetic field of the objective lens and it is effectively used to detect the signal from the material kept at a distance 0 to 8 mm from the bottom end of the column. These signals passing above the objective is collected by applying a positive voltage and the surface image will not show any directional or shadowing effects.

2.4.7 Sample preparation for FESEM imaging

Specimen is usually grounded[111-113] to take away the extra electrons accumulated on the sample. These accumulated charges can repel the incoming electrons and there by the image resolution, so better resolved image can be obtained from conducting sample. For samples like insulating porous alumina used as a substrate for CdS nanotube synthesis can result in electron-electron scattering from the accumulated charges on the surface and thereby reducing the resolution known as charging effect. This can be avoided by coating the surface with metal films like gold and platinum by sputter deposition to take away the extra electrons. To avoid the charging effect, CdS nanotubes attached on porous alumina is coated with 15 nm gold films for high resolution images. Another way to reduce such charging is to use less accelerating voltage, where the secondary and back scattered electrons have higher probability to escape from the surface. But in the case of higher voltages, most of the secondary and back scattered electron created in the depth cannot escape and accumulate within the sample. These negative charges on the samples actually deflect the incoming electrons and there by distort the SEM images. To avoid charging effects, working with a voltage in the range of 3 to 5 KV and coating the sample with gold is a good choice for our CdS nanotubes prepared on porous alumina. To provide a conductive path for extra charging electrons to ground, CdS nanotubes on insulating porous alumina are placed on a conducting carbon tape [less resistivity] which is attached to a metallic stub in the sample holder. Scanning electron image of as prepared porous alumina is shown in the figure 2.6.

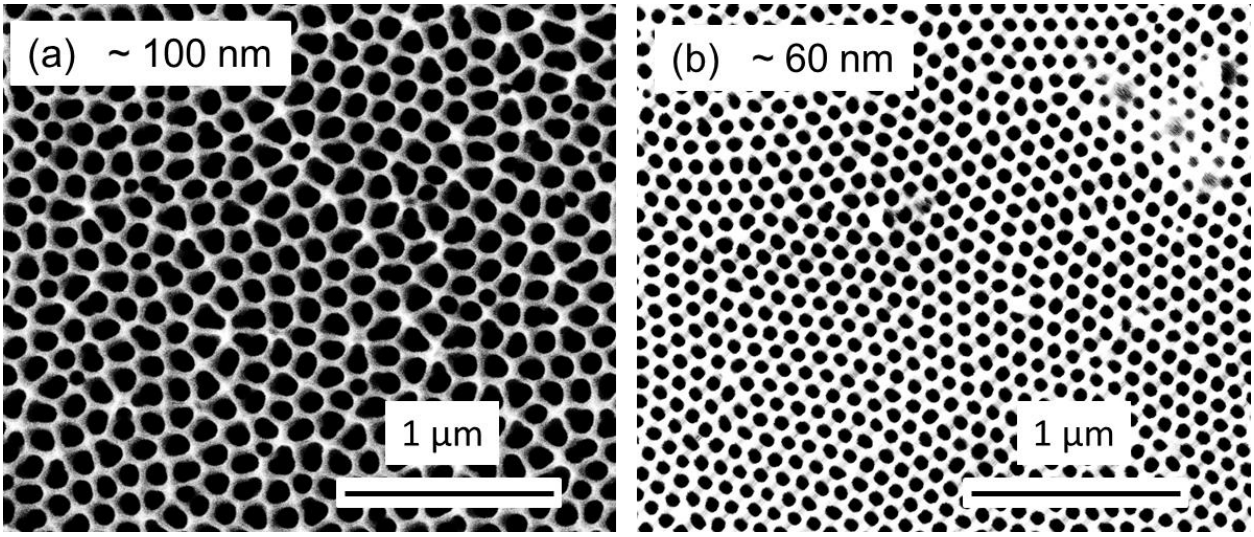

Figure 2.6: (a) Scanning microscopy image of porous alumina prepared by anodization at 60 V (b) and at 40 V.

2.4.8 Characteristic x-ray detection

In general x-rays are generated from an element as a result of the excitation of inner core electrons by a high energy electron beam[111-113] and subsequently these vacant electronic levels in the inner shell are filled by outer electron giving rise to emission of x-rays as shown in the figure 2.7. The energy released in the form of x-rays is the characteristic of the typical atomic transition and dependent on particular atomic mass of the element. These x-rays generated are represented by a sequential way, for a transition from L [n=2] to K [n=1] shell is denoted by K_α and for M to K shell is represented by K_β and similarly for the other outer transition. These characteristic peaks of x-rays have lot of background noise from bremsstrahlung radiation. This occurs due to acceleration of electron towards nuclei which will produce x-ray of continuous energies. The intensity is low but it is visible for low characteristic x-ray energies in the spectrum.

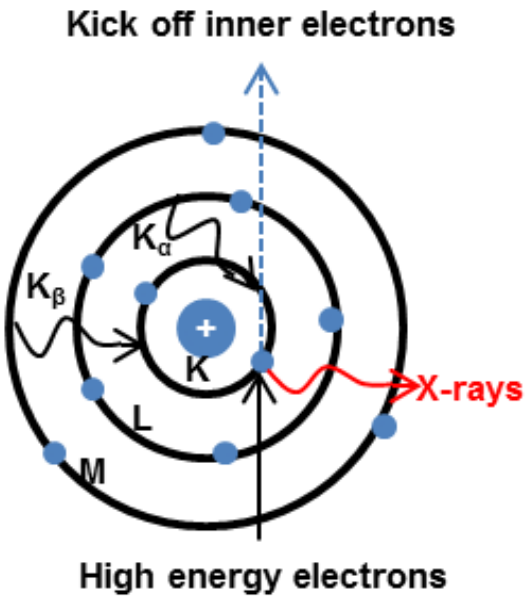

Figure 2.7: Schematic representation of X-ray generation by a high energy incident electrons.

Energy Dispersive X-ray Spectroscopy [EDS] detector[111-113] [our FESEM uses 80mm^2 Oxford EDS detector with concentric electrodes] is a semiconductor diode made from a single crystal silicon for collecting the x-ray signals. X-ray penetrates into the p and n region and its energy is used for the release of valence electrons. This charge creation is proportional to the electron-hole pair generation by the x-ray energy [N=hν/ΔE] and can be collected by applying a reverse bias. Optimized working distance, voltage and detector position is chosen for better x-ray signal collection. In compound samples, accelerating voltage used should be more than two times the characteristic energy [KeV] of the heavier element[111] for better compositional studies. Lower voltage reduces the interaction volume and also the x-rays signals. By increasing the voltage the interaction volume is increased and also the x-ray signals. All these above parameters are optimized for a better elemental analysis for the CdS nanotubes.

2.5 Optical absorption spectroscopy

2.5.1 Band gap determination

One of the simple ways to determine the band gap of a semiconductor is to use optical absorption spectroscopy[4,62,63,99]. Photons having energy higher than the band gap energy can

excite electrons from the valence band to conduction band. This results in a net decrease in the intensity of the light along its propagation direction. As the incident light interact with the material some of them get reflected from surface, also get absorbed or scattered by the atoms and the remaining is passed through the sample. From the classical electrodynamics, dielectric constant of the material can be divided into imaginary and real parts for an electromagnetic wave which interact with the medium. Real part is the refractive index [n] and imaginary part [k] is known as the extinction coefficient or can be related to absorption. Attenuation of the light by absorption in the material is described by Bears-Lambert law[99,114] [equation 2.1], which relates the incident and transmitted light.

$$I = I_0 e^{-\alpha h} \tag{2.1}$$

Here I is transmitted intensity, I_0 is the incident intensity, h is the thickness of the sample and α the absorption coefficient is related to the extinction coefficient[63,99,114] by equation 2.2.

$$\alpha = \frac{4\pi K}{\lambda} \tag{2.2}$$

In general for a liquid sample the law is given by equation 2.3.

$$I = I_0 e^{-\epsilon c L} \tag{2.3}$$

Here ε is the molar absorption in the unit mol^{-1} cm^{-1}, c is the molar concentration [M] of the absorbing molecule or compound. L is the length [cm] of the liquid, where the light is passing through. The transmission of light is expressed in terms of absorbance by equation 2.4 and this can be used for measuring the absorbance and transmittance of the sample used.

$$A = \ln\left(\frac{I}{I_0}\right) = \varepsilon c L \tag{2.4}$$

2.5.2 Absorption coefficient

Absorption spectra as shown in the figure 2.8 are divided into three parts[99,115]. In region I, rise of absorption coefficient is due to the presence of impurities and defect states in semiconductor. It is well known that this region mainly depends on the structural property of the

material. Region II is mainly due to tail in the density of states in the conduction and valence band. This tail is known as urbach tail and can occurs due to dangling bonds or disordering in the material, which can give extra density of states in the forbidden band near to both bands and absorption coefficient α is proportional to exp ($\hbar\omega/E_u$). E_u is the width of the tail. A sharper tail and smaller E_u represent less disordered sample.

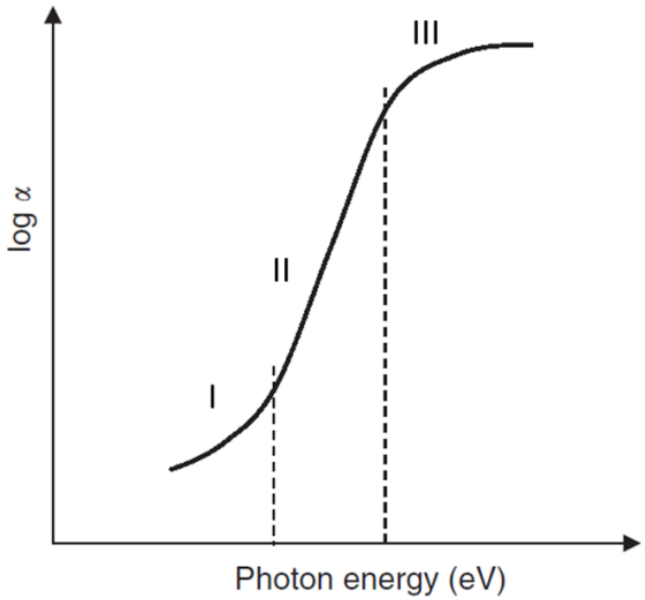

Figure 2.8: Three regions for an absorption coefficient in a disordered semiconductor. Taken from Jai Singh and Koichi Shimakawa, Advances in Amorphous Semiconductors[99,115].

The third region is the strong absorption region where the band edge absorption begins above a certain energy threshold. In general the relation between the absorption coefficient and the energy of the photon is given by

$$(\alpha\hbar\omega)^n \propto \exp(\hbar\omega - E_g). \quad \textbf{(2.5)}$$

E_g is the band edge absorption and the n value varies for different semiconductor. The plot between $(\alpha\hbar\omega)^n$ and $\hbar\omega$ is known as Tauc plot[64,81,99,115] and the maximum slope which intersect with the $\hbar\omega$ axis give the band gap of the semiconductor. For a direct band gap semiconductor like CdS the value of n is approximately 2[115,116,117].

2.5.3 UV-Visible spectrophotometer

Spectrophotometer as shown in the figure 2.9 has a source of light, optical elements like monochromator for dispersing its different constituent wavelengths, sample holder and detector for collecting the transmitted photons[114]. Quartz tungsten halogen lamp has board spectra with a span of wavelength having similar intensities are used for absorption studies at visible ranges. For UV illumination, this instrument uses deuterium lamp. Monochromator is used to select a particular wavelength for a particular time period and sends through the sample for absorption analysis. At the end a detector is used to measure the intensity of the signal passing through the sample, its main function is to convert light signal into electrical signal. Spectrophotometer either uses photomultiplier tube or photo detector made from a semiconductor diode for detecting the signal. Both can detect signal form UV to entire visible range. For a low absorbing media photo detector is the best one with less output noise. We use Perkin Elmer's Lambda 950 spectrophotometer to measure absorption of CdS nanotubes on porous alumina.

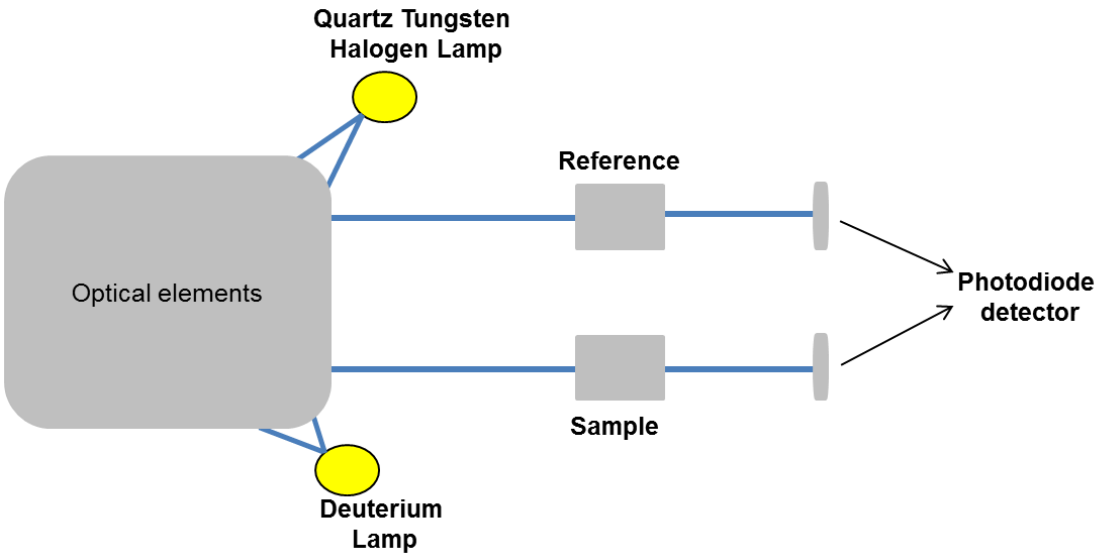

Figure 2.9: Schematic of a dual UV-VIS spectrophotometer used for absorption studies[118].

2.6 Photoluminescence (PL)

Interaction of semiconductor with electromagnetic radiation with energy above band gap excites the electrons from the valence band to conduction band. Excited electrons lose some of their energy with lattice interaction and then finally by recombining with the holes in the valence band by emitting photons. This radiative transition can be measured using photoluminescence [PL] spectroscopy[2,4,63]. Defects in the crystal can act as trapping center for these excited holes and the electrons and thereby reducing the energy of emitted light through non-radiative processes[2,4,63]. Thus the efficiency of PL process is dependent on the nature of defects. Emission spectrum can also broaden and red shifted from the absorption edge due to defects and energy levels close to the conduction and valence band. Similar to UV absorption spectroscopy, the PL measurement is done with exciting the material with a selected wavelength from xenon lamp by using a monochromator. Usually an entrance slit is used for the incoming radiation and exit slit to measure the intensity of optical emission. PL with different wavelength is selected by a monochromator and finally a detector for intensity measurement. We use Horiba Jobin Yvon's Steady-State Spectro-fluorometer to measure PL**.**

2.7 X-Ray diffraction

2.7.1 Bragg diffraction

In general x-ray diffraction is one of the best methods used to identify the crystal lattice, crystalline size and lattice distance between planes in a crystalline solid. Diffraction of X-ray having wavelength of the same order of lattice constant from a regularly arranged atoms or planes results in an intensity pattern at different angles[4,119-121]. X-ray diffraction or actually scattering of x-rays by atoms have intensity only at a particular angle θ which is defined by equation 2.6 known as Braggs law[4,119,120]. This usually provides the information on crystal phase, distance between two planes and also the [hkl] plane from where the x-rays are scattered. In general the x-ray diffraction pattern is measured by rotating the crystal with respect to the

incident x-rays and intensity pattern is observed at various Bragg angle θ. But in the case of powder sample, the random orientation of the planes is provided by the random placement of the small fragments. This is equivalent to rotating crystal, so powder samples can be mounted on a holder and the incident beam is diffracted from the planes. This intensity is measured by moving the detector around a circular path 2θ with respect to the incident beam and will give the Bragg diffraction patterns.

$$n\lambda = 2d\ sin\theta \tag{2.6}$$

Most of the powder x-ray diffractometer work in θ – 2θ and θ - θ geometry known as Bragg-Brentano arrangement[120]. In our Bruker D8 advanced X-Ray Diffractometer monochromatic x-rays [K_α = 1.5 A] is produced from an x-ray source which is designed to rotate in θ angles. These incoming x-rays are scattered from the powder sample which is fixed inside a holder and finally a detector is used to measure the intensity of diffracted beam. Detector can rotate in a circular path with a specified θ value. Diffracted x-ray intensity is recorded against the 2θ value which can be used for further material characterization. Figure 2.10 shows a simple model of the x-ray diffractometer used. The intensity peak observed for various planes in the x-ray diffraction can be broadened due to instrumental error, variation in the lattice constant, particle size and also some time non uniform strain in the crystal[119,120]. The lattice constant of hexagonally packed cadmium sulfide can be calculated using the equation 2.7.

$$\frac{1}{d^2} = \frac{4}{3}\left(\frac{h^2 + hk + k^2}{a^2}\right) + \frac{l^2}{c^2} \tag{2.7}$$

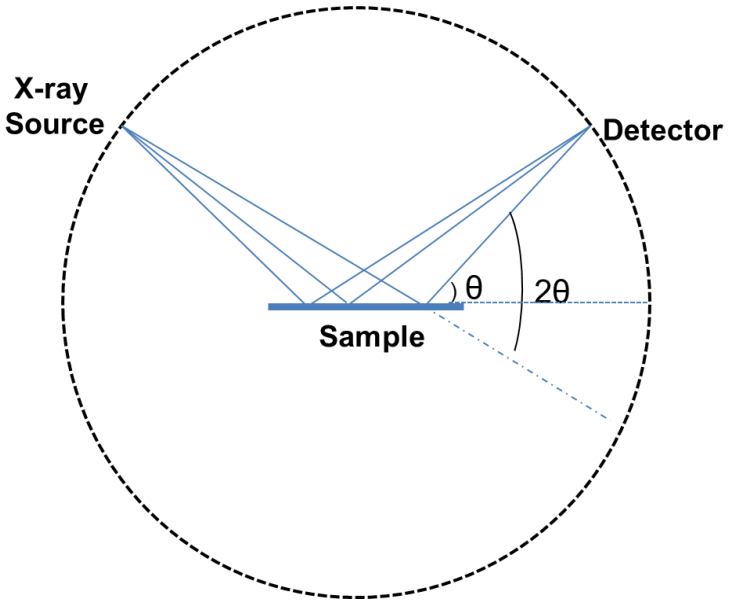

Figure 2.10: Schematic of powder x-ray diffractometer in θ - θ geometry [119,120].

2.7.2 Broadening of X-ray peaks

X-ray peaks are broadened due to slit widths of the instrument, imperfect focusing of x-rays, unresolved peaks and these are collectively known as instrument broadening[119,120]. In modern x-ray diffractometer, broadening due to instrumental part other than sample is negligible compared to the small particle size effect, micro strain and unresolved peaks. Broadening of x-ray peak can be used to determine the particle size by Debye-Sheerer method[119,120] for crystallite size < 100 nm. Overlapping peaks from small crystallites is a problem for exactly determining the size and also the exact crystal phase. In the case of CdS nanotubes the neighboring peaks of wurtzite crystal phase around 26.7º overlap due to nanocrystalline nature which can also exactly matches with the single peak from the Zinc blende structure at that particular angle. In this case it is extremely difficult to identify the exact crystal size and also the phase.

2.7.3 Crystalline size

It is experimentally observed that the width of the peak decreases with particle size. Incident x-rays which are not parallel but have a range of incidence angle θ_1 and θ_2 can shift the

pattern from the Bragg angle θ[119,120] . These two angles will not produce a complete destructive or constructive interference patterns. Path difference of half wavelength of x-ray diffracted from two planes at angle θ can complete a destructive inference and leads to negligible diffraction intensity. But in case of the very thin sample or small particles there are planes missing in the crystal and can leads to incomplete destructive interference around the Bragg angle θ. This leads to broadening of the peak around the Bragg angle[119,120] and can be further used for determining the particle size by using Debye-Scherrer formula [equation 2.8].

$$D = \frac{k\lambda}{\beta cos\theta} \quad \textbf{(2.8)}$$

Here D is the particle size, β is the full width half maximum in radians or can be integral breadth of the peak, λ is the x-ray wavelength, θ is the Bragg diffraction angle and k is the shape factor which depends on the crystalline shape. Normally the value of k is close to 1 and in the most of the cases the chosen value is around 0.9.

2.7.4 Micro strain

Local variation in d_{hkl} due to strain [ε] in the crystalline grains occurs due to external forces like pressure, lattice defects etc. Compositional variation of the alloy crystals is also another reason for the broadening of x-ray diffraction peak[119,120]. In general strain can be divided into uniform or non-uniform deformation as in the figure 2.11. These strains inside the crystalline material are by stretching or compression of planes of atoms from their original lattice position. Tensile strain will increase the bond length and there by shifting diffraction angle to a lesser side. But in the case of compressive strain the bond length is decreased and similarly the diffracted angle θ is shifted to a higher side. We can experimentally view a systematic shift in the diffracted angle from the measurements. For example in one dimensional structures, this type of uniform strain can be developed by applying an external forces to bend the nanowires[102] and thereby creating regions of compressive tension and tensile strains. But in the case of non-uniform strain which is mainly due to the residual strain in grains can lead to regions of both compressive and tensile regions. This is experimentally observed by broadening of the x-ray diffraction. Non-

uniform strain[119,120] is calculated using the equation 2.9, where β is the integral breadth of the peak.

$$\varepsilon = \frac{\beta}{4tan\theta} \tag{2.9}$$

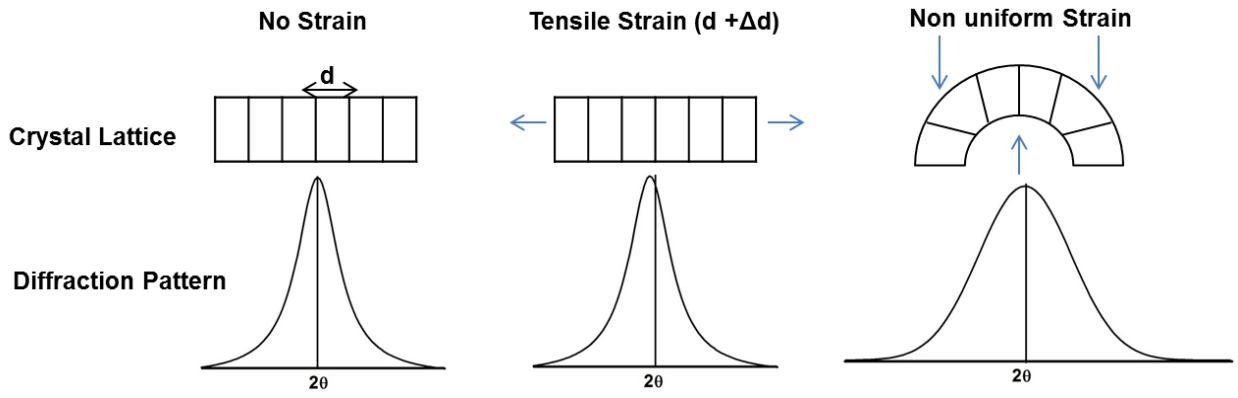

Figure 2.11: Influence of strain in the crystals can be observed from the x-ray diffraction peak[119,120].

In the case of nanocrystals, broadening occurs due to micro strain and particle size. Both methods would not give the exact size and strain. There is a method known as Williamson-Hall[120] method used for determining both size and strain effects in small crystals. Williamson-Hall equation 2.10 is actually a straight line, whose slope can be used to calculate the strain and the intercept on the βcosθ provides an estimate of the particle size D.

$$\beta_{hkl}cos\theta = \frac{k}{D} + 4\varepsilon sin\theta \tag{2.10}$$

2.8 Summary

In this chapter, required fabrication techniques and procedures needed in synthesis process of porous alumina and ligand free cadmium sulfide nanotubes are discussed. We also briefly described the working principle of necessary microscopic and spectroscopic techniques like scanning electron microscopy, energy dispersive x-ray spectroscopy, absorption spectroscopy, photoluminescence spectroscopy and x-ray diffraction used in this thesis work. Standard ways of

identifying the band gap of semiconductor using absorption spectroscopy is also discussed in this chapter. Similarly, micro strain and crystalline estimation of nanostructures using powder x-ray diffraction pattern is discussed in detail.

Chapter 3

Directionally Asymmetric Growth of Ligand Free CdS Nanotubes using Alumina Nanoreactors: Need for chemo-hydrodynamic instability at nanoscale

---

3.1 Introduction

In general, liquid-liquid and liquid-solid interfacial forces play vital roles in self- assembly of nanostructures. It is important to understand the role of interfacial hydrodynamics in self-organization of nanostructures near such interfaces, where growth nucleation happens. One way to probe such interfacial effects on nanofabrication is to grow self-assembled array of ordered nanotubes and quantitatively estimate different growth parameters under various conditions. We made similar attempts by growing these structures using nanoporous alumina[22,23] based nanotemplates as discussed in chapter 1 and 2. We use a particular nanofabrication route [figure 2.3] to synthesize and self-assemble ordered arrays of cadmium sulfide [CdS] nanotubes and then finally to understand the interdependence of hydrodynamics and chemical reactions in this nanofabrication process.

Interestingly, we found a directionally asymmetric growth of CdS nanotubes on one side of porous anodic alumina by horizontal capillary flow of two different chemical reagents from opposite directions through the nanochannels. Uneven flow of chemical precursors through the porous alumina nanochannels initiates this asymmetric growth. Structural evidences observed from scanning electron microscopy images suggest that it requires chemically triggered hydrodynamic instability for the prolonged nucleation of CdS nanotubes. However, standard estimates of dimensionless numbers used to quantify the onset of hydrodynamic instabilities are not sufficient enough to explain the role of such non-laminar flow in the nucleation process at such small length scales. This certainly shows that further understanding of the origin of such chemo-hydrodynamic instabilities at nanoscale is essential.

3.2 Directionally asymmetric growth

As discussed in section 2.3, flow of chemical precursors [0.1M $CdCl_2$ & 0.1M Na_2S] kept at opposite side of few micrometers thick porous alumina template and subsequent reaction within such a nano-confined space result in self-organizations of CdS nanowires [figure 3.1], later we identify this is actually hollow nanotubes. It was expected that two different precursors [0.1 M $CdCl_2$ & 0.1 M Na_2S] flowing horizontally through nanochannels from opposite sides of AAO membrane mix and react to form solid CdS and this could block further growth. However, directionally asymmetric growth[109]of CdS nanowires oriented along one direction on porous alumina facing Na_2S solution is observed during such nanoreactor based chemical synthesis. These nanowires are imaged by scanning electron microscopy [SEM] and elemental composition was characterized by localized energy dispersive x-ray spectroscopy [EDS]. Heights of these two aqueous precursors placed in respective chambers are kept at the same level to avoid any pressure difference on both sides of the AAO membrane.

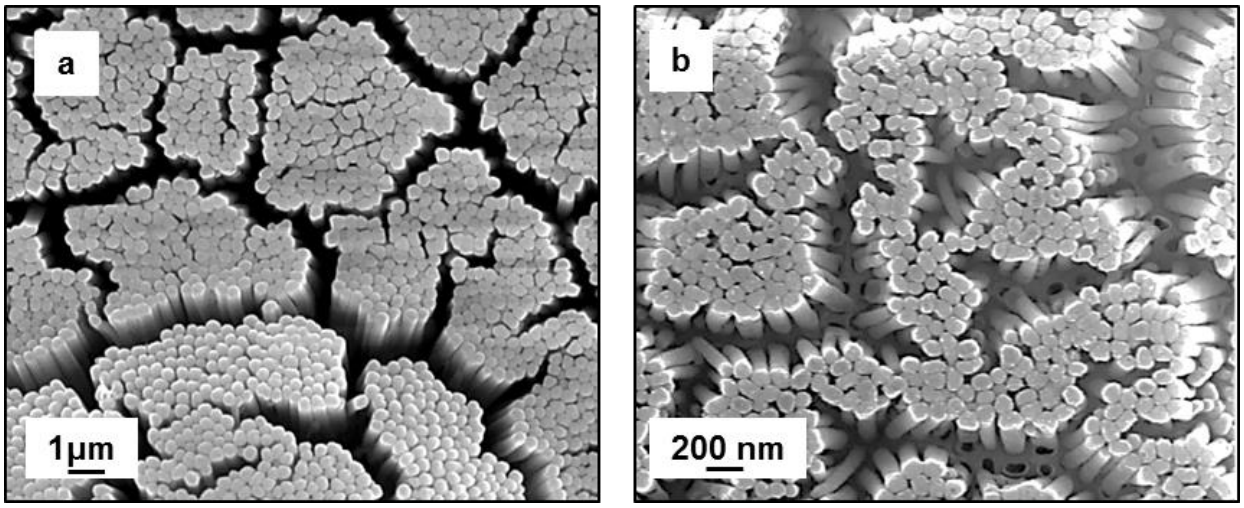

Figure 3.1: Surface topography of CdS nanowires with diameter a) ~ 200nm b) ~100nm growing horizontally from one side of the AAO membrane facing Na_2S solution.

Scanning electron microscope images [figure 3.1] clearly show that CdS nanowires grow horizontally only on one side of porous template facing 0.1M Na_2S solution and extend to few micrometers in length [figure 3.2] after few hours of growth. However, from figure 3.2(b), we

see very little presence of these elements on the other side of porous alumina facing $CdCl_2$. We also studied the elemental composition on these CdS nanowires grown in Na_2S side of porous alumina using energy dispersive x-ray spectroscopy. These insets show the presence of both elemental sulfur and cadmium.

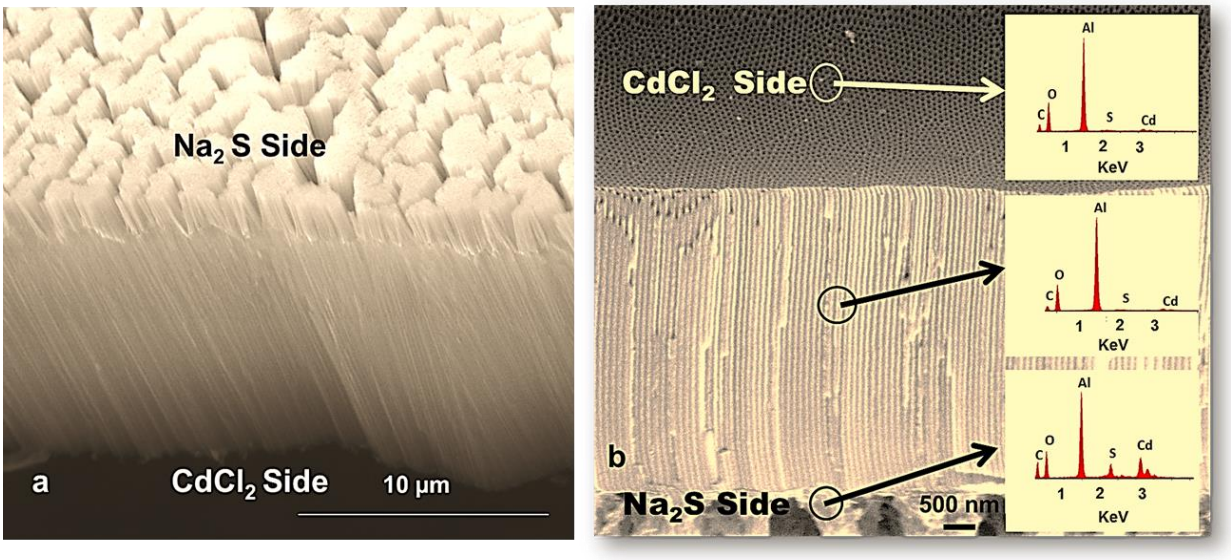

Figure 3.2: (a) Cross-sectional SEM image of as grown CdS nanowires on the top side of AAO template of pore diameter ~ 100 nm [anodization voltage 60 V] facing Na_2S during the two-chamber nanoreactor synthesis process. (b) SEM image shows the clear absence of nanowire outgrowth on the top side of AAO having pore diameter ~ 60 nm [anodization voltage 40 V] facing $CdCl_2$ solution. EDS spectra taken from various parts of this AAO template do not show any significant presence of both Cd and S atoms on the $CdCl_2$ side of the template. Circles and arrows indicate the portion of the AAO template used for cross-sectional EDS scan.

3.3 Structural observation from FESEM images

Next we presented the topography of CdS nanowires [figure 3.3(a) , (b) & (c)] grown on AAO nanotemplate having different pore diameters and using 0.1 M $CdCl_2$ and 0.1 M Na_2S as a reacting precursors. One sided growth is also visible [figure 3.3(d)] by diluting both chemical

precursors to 0.005 M. However, it takes longer growth duration [around 24 hours] to make micrometer sized lengths using this two chamber 'nanoreactor' synthesis at lesser concentrations.

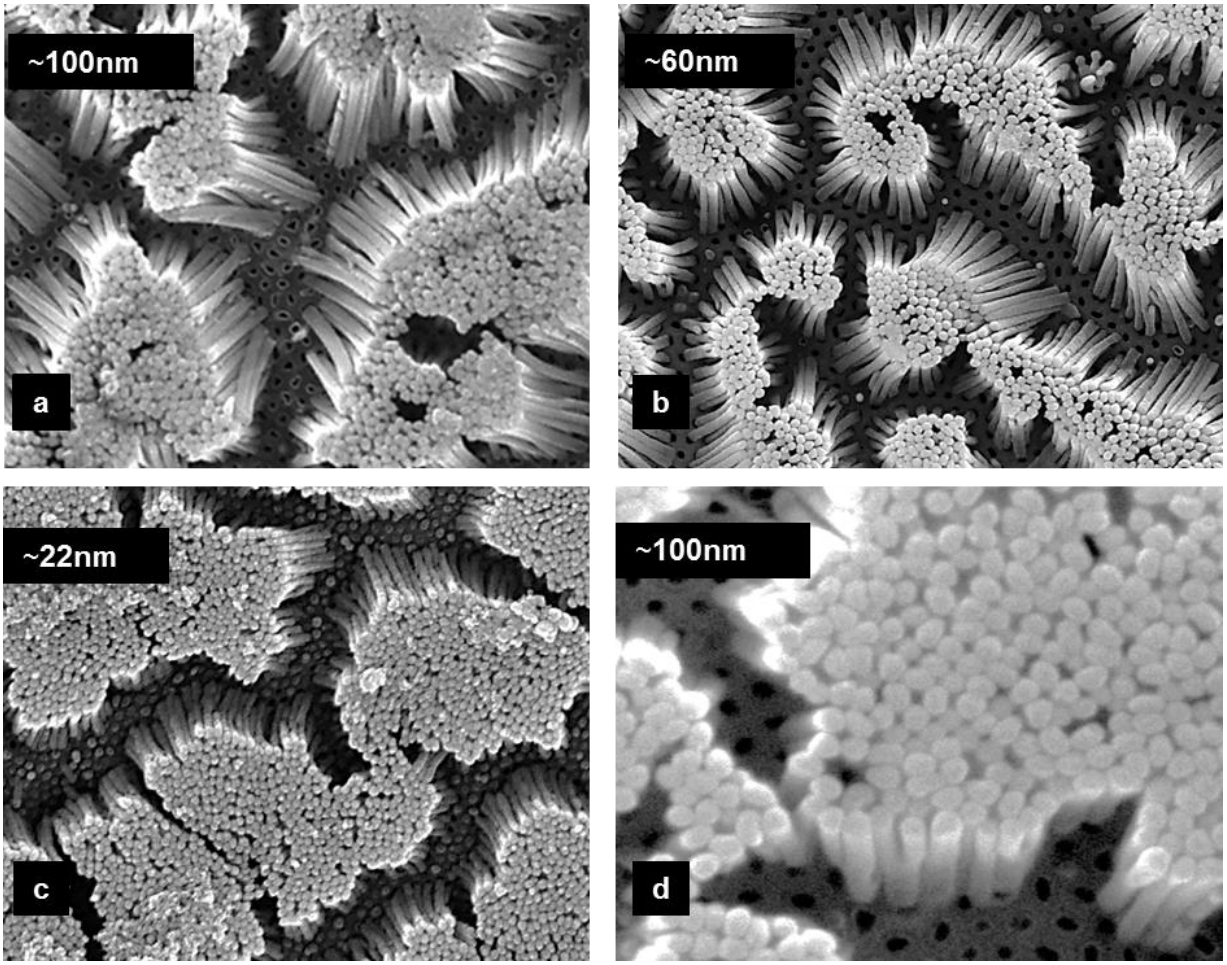

Figure 3.3: SEM images of CdS nanotubes grown on AAO pores fabricated in 0.3M oxalic acid under anodization voltage of (a) 60 V, (b) 40 V, and (c) 18 V [0.3 M in H_2SO_4] and further synthesized with 0.1M $CdCl_2$ and 0.1M Na_2S. (d) CdS grown on 60 V anodized AAO and using dilute concentration of [0.005M $CdCl_2$ and 0.005M Na_2S] precursors. The top end of each of these nanotubes is also closed.

We also noted some important structural observations: 1) first we see from figure 3.3, the top end of each nanowire like structure is closed, 2) then we also notice from figure 3.3(a) that there is visible cylindrical wall like formations on the top surface of porous channels and finally 3) we can clearly see from figure 3.4(d) that CdS nanowires are indeed hollow nanotubes and not

solid nanorods. So we can assume that the nucleation and subsequent growth processes of these CdS nanotubes happen at AAO-Na_2S interface. Additionally, from FESEM images [figure 3.3], we can clearly measure the width [~20 nm] of these nanotube walls, which is not affected significantly by changing the diameter of AAO pores or with varying concentration of reactants.

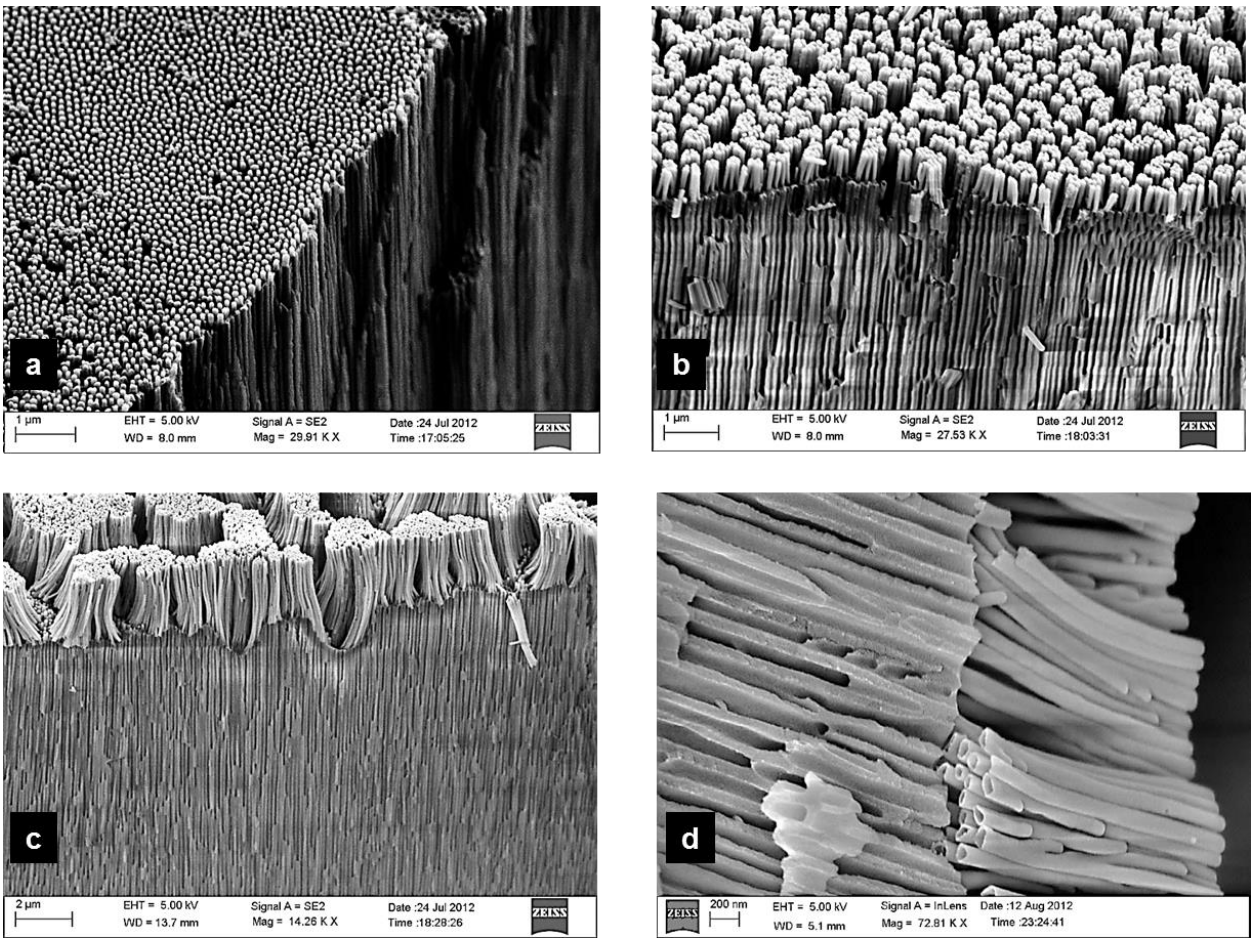

Figure 3.4: SEM images of CdS nanotubes synthesized on the top surface of AAO pores of diameter ~100 nm for different time durations: (a) 30 min, (b) 1.5 h, (c) 2 h and (d) 3 h. Figure (d) clearly shows the nanotubular growth. Top ends of all these nanotubes are closed. However, these nanotubes are still growing in length from 30 minutes to 3 hours of synthesis duration.

3.4 Role of hydrodynamics in growth process

3.4.1 Is there any nanofluidic flow?

All these above FESEM images lead us to assume that flow of cadmium ions [such as Cd^{++} or $[CdCl_4]^{-2}$ complexes] through these nanoporous channels is initiating this directionally asymmetric growth. Normally, we expect these mixing of chemical reactants to cause clogging of the AAO pores and thereby preventing further directional asymmetric growth of CdS. However, we see the growth only on Na_2S side of the nanochannels. Therefore, we guess that these cadmium ions flowing through the nanochannels eventually reach the other end of the AAO, react with sulfur ions [such as S^{--} or HS^-] near the Na_2S side of AAO template. Otherwise CdS formation should also be present on the side of AAO facing $CdCl_2$ precursor. So, one main reason for such one side growth is the reduced flow of sulfur containing anions through these nanochannels as compared to cadmium containing ions. This will be discussed more in Section 3.4.2.

In order to understand the mechanism of nanotubular growth process, we first thought of any plausible nanofluidic effects [as discussed in section 1.14.3][32,36]. Here the charged inner surface of AAO nanochannels can affect the ionic flow and also any subsequent reaction of chemicals in these nanochannels. Usually such nanofluidic effects can be explained by electric double layer [EDL] formation [section 1.14] on charged surface of AAO nanochannels, where at low ionic strengths, formation of EDL can effectively prevent co-ions and allow counter-ions to flow through the pores[36]. Estimated EDL thickness or Debye length [λ_{Debye}] for nanochannels with diameters ~100 nm is found to be less than 1 nm for 0.1M solution[36] used in the synthesis. Similarly for a 0.005M salt solution estimated λ_{Debye} hardly increases to a few nanometers only, which is much smaller than the pore diameter of porous alumina used in our nanofabrication process. For a completely ionized salt solution, the estimated λ_{Debye} values are much smaller compared to the average outer inner diameter of these AAO nanochannels [d ≈ 20-100 nm]. Therefore, we conclude there is no effect of EDL induced standard nanofluidic processes[35,122] in these nanochannels. Interestingly the wall thickness of these nanotubes is ~20 nm and this value

is not significantly varying with concentration. Thus we can ignore comfortably the EDL effects on the ionic flow of reactants and also tubular wall formation on AAO nanochannels.

3.4.2 Directionally asymmetric growth is driven by increased flow rate of cadmium ions through AAO nanochannels

For further understanding, the pH of the solutions are measured and found out to be 6.5 for 0.1M $CdCl_2$ and 13 for 0.1M Na_2S. It is also well known[34,123] that the surface charge of AAO is determined by pH of the solution. The isoelectronic point [section 1.14.1] of AAO is generally around a pH of 8-9. Therefore, it is possible that capillary flow rates of these chemical precursor[124] ions through these AAO nanochannels can be driven by the existing imbalance of chemical potential on both side sides of AAO nanochannels. It is expected that the high pH of 0.1M Na_2S can increase the density of negative charges on AAO nanochannels and thereby produce an additional hindrance to the flow of S^{--}. On the other hand, cadmium ions with less pH of 6.5, have to face a less flow resistance inside these narrow nanochannels as compared to sulfur anions. So we argue that these negatively charges developed on the surface at such high pH levels can actually slow down the flow of Na_2S precursors within these AAO pores as compared to the faster flow rate of $CdCl_2$.

We had done a simple experiment to verify the above arguments by permitting one precursor at a time (a) 0.1M $CdCl_2$ or (b) 0.1M Na_2S to flow through identical AAO nanotemplates of pore diameter around 100 nm for 1 hour in two separate experiments. In all cases, (a) 100 ml of 0.1M $CdCl_2$ or (b) 100 ml of 0.1M Na_2S is placed on one side of AAO template while the other side of the chamber [Section 2.3] with 100 ml of 18.2 MΩ-cm de-ionized water only. These $CdCl_2$ [Na_2S] then flow through the AAO nanopores and finally reach the other side, which is the de-ionized water bath. After 1 hour duration, the trace amount of $CdCl_2$ [Na_2S] in de-ionized water bath was taken out. Then 6 mL of this collected solution is mixed with 2 mL of 0.05M Na_2S [0.05M $CdCl_2$] solution to form CdS. These 2mLs of 0.05M Na_2S [0.05M $CdCl_2$] is sufficient enough to react with all the traces of $CdCl_2$ [Na_2S] in the collected 6ml of solution to form CdS. It is also noticed that such flow through these nanochannels is negligible to change the pH of the de-ionized water in a significant way. Later

on, optical absorption experiments [figure 3.5(a)] clearly show a higher optical absorbance for a flow of (a) only $CdCl_2$ as compared to the (b) only Na_2S through identical AAO membranes.

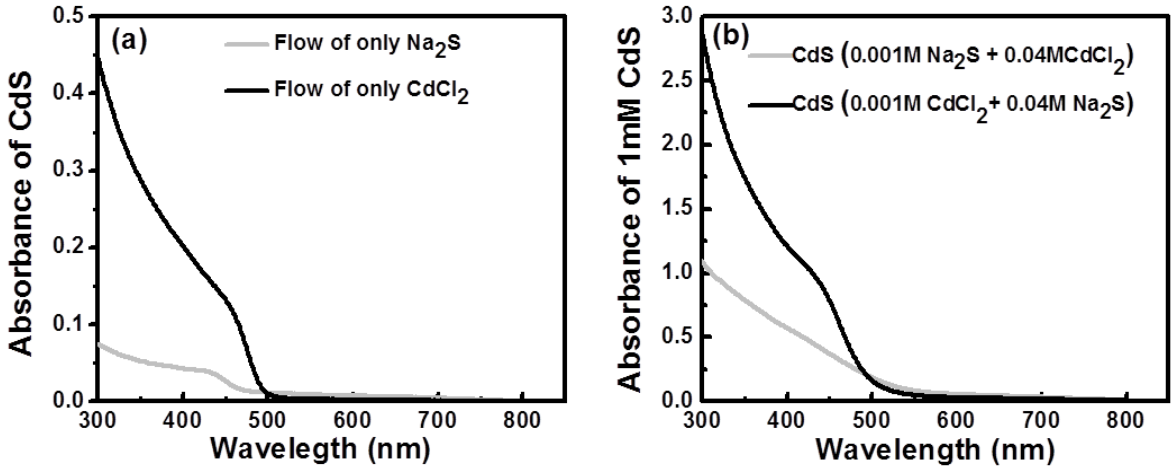

Figure 3.5: (a) Optical absorption spectra showing higher amount of CdS formation due to increased flow rate of $CdCl_2$ as compared to Na_2S through AAO nanochannels. (b) Optical absorption spectra to determine the molar extinction coefficient of CdS formed by bulk mixing of $CdCl_2$ and Na_2S [with one precursor in excess amount] in respective cases.

Optical absorbance [A] as discussed in section 2.5 is directly related with the concentration of CdS in the solution as $A = \varepsilon Lc$ [equation 2.4], where ε is the molar extinction coefficient of CdS, L is the absorption length of the solution [=inner diameter of the cuvette], and c is the concentration of CdS in moles. It is well known that, the value of ε depends on various parameters during the formation of CdS. We observed a slight variation of molar extinction coefficient for solid CdS in the de-ionized water prepared by two different ways, one solution of CdS having excess Na_2S [by mixing 0.001M $CdCl_2$ and 0.04M Na_2S] and the other solution of CdS having excess $CdCl_2$ [by mixing 0.04M $CdCl_2$ and 0.001M Na_2S]. By using the particular absorbance spectra [figure 3.5(b), at 445 nm], the estimated ε for CdS in excess amount of Na_2S is found to be around 8.9×10^2 L mol^{-1} cm^{-1}. Similarly, the ε for CdS formation in excess amount of $CdCl_2$ is found to be around 3.8×10^2 L mol^{-1} cm^{-1}. Using the above values of ε and absorbance [A] point at 445 nm as in figure 3.5(a), we can estimate the concentration of Cd or S [same as CdS] in 100 ml of de-ionized water for a flow of (a) only $CdCl_2$ and (b) only Na_2S through alumina nanochannels for similar time duration. These estimated values are respectively

a) 0.22 mM and b) 0.132 mM. Thus the concentration of CdS estimated in separate flow clearly shows the excess flow of 0.1M $CdCl_2$ through these smaller AAO nanochannels as compared to 0.1M Na_2S. Therefore, we argue that the main reason for initiating the directionally asymmetric structural elongation of CdS nanotubes is possibly due to the difference in their flow resistance [e.g., viscous drags] of these two chemical precursors as evident from individual flow rates.

Additionally, we can estimate diffusion coefficient using Fick's law [section 1.15.1] $J = -D\frac{\partial c}{\partial x}$, where J in mol/cm^2 s is the flux of ions estimated from the concentration of CdS formed in 100 mL de-ionized water, D is the diffusion coefficient, c is in mol/cm^3 and $\frac{\partial c}{\partial x}$ is the concentration gradient of 0.1M across 30 µm length of these nanochannels in both cases. From this, the estimated value of diffusion coefficients of Cd^{++} and S^{--} ion flowing through alumina nanochannels is found to be around 5.8 x 10^{-7} cm^2 /s and 3.5 x 10^{-7} cm^2 /s, respectively. Influence of both pH and concentration of precursors on growth process of CdS nanotubes is visible from figure 3.3(d), where reducing the above will require more time [24 h] to reach up to a particular length of nanotubes.

On the other hand, one can also mention that the observed faster diffusive flow of Cd^{++} ions [ionic radii: ~ 0.109 nm] as compared to S^{--} ions [ionic radii: ~ 0.184 nm], is possibly due to the difference in their size. However in these nanochannels, size controlled diffusion of Cd^{++} and S^{--} can begin only after the two chemical precursors mix together and react to form CdS. It is also implausible that the elongation of tube like structures visible from SEM images can make from such diffusion dominated bulk flow through AAO nanochannels. In a real case, formation of solid CdS can block any flow of these precursors through nanochannels and thereby preventing any such bulk diffusion and mixing of ions. We will discuss more about the roles of diffusion in chapter 4, where we will argue that diffusion alone is not enough to explain the elongation of CdS nanotubes.

3.4.3 Mechanism of CdS nanotube nucleation at the edges of AAO nanochannels

Similar to a fluid flow in narrow channels [section 1.12], the first capillary meniscus containing cadmium ions may have plug like profile at the exit end of the AAO nanochannels.

This will react with sulfur ions to form a closed end structure on its exit. This is visible from figure 3.4(a) and also illustrated in figure 3.6(a), which shows an early "cap" like structure of CdS formation. This happens only when the meniscus of cadmium precursor solution react with the sulfide ions at the nanochannel exit and thereby initiating the elongation of nanotubes. Otherwise, we can see a clogged AAO nanochannel with a random aggregates or cylindrical structure of CdS strongly attached to inner pores. This will ultimately stop the physically mixing of chemical precursors separated by the clogged pores and finally the elongation of nanotubes. Interestingly from scanning electron microscope images [figure 3.4], we observed an elongation of nanotubes after few hours. Moreover, SEM images having thin walled nanotubular structures [figures 3.3(a), 3.4(d)] on porous alumina exit, is a clear indication of nucleation in the form of nanotubes. It is again clear from the SEM images; the top ends of these nanotubes are closed from the starting process of nucleation. Most importantly, our understanding of growth nucleation is further proven for CdS nanotubes grown with different time durations [figure 3.4] of nanoreactor synthesis.

As evident from SEM images [figure 3.4] the length of these nanotubes grown horizontally is increasing with time duration of synthesis [30 min to 3 h]. So, nucleation of this observed elongation happen near the edges of AAO, with top end of these CdS nanotubes are already closed [figure 3.4(a)]. To support the above growth process, we also noted an important structural fact from SEM images [figure 3.3 & 3.4], that the appearance of broken edges of nanotubes only on AAO surface. So clearly, this is the place where the anticipated nucleation of such tubular growth actually takes place. Thus, the joint of CdS nanotubes with AAO edge can be regarded as weakest structural points of these nanotubular CdS and it is where the nucleation takes place for further elongation. As a result, most of these nanotubes break only from these joints or clumped together by van der Waals interaction during the post growth washing and drying sequences. If the location of nucleation sites is at top end of these nanotubes as per figure 3.6(b), then such uniformity of nanotubes should not be visible by un-confined mixing of chemical precursors. Therefore, the observed closed end structure of CdS nanotubes having uniform geometry clearly rules out the possibility of nucleation at the top ends of nanotubes for further elongation as shown in figure 3.6(b).

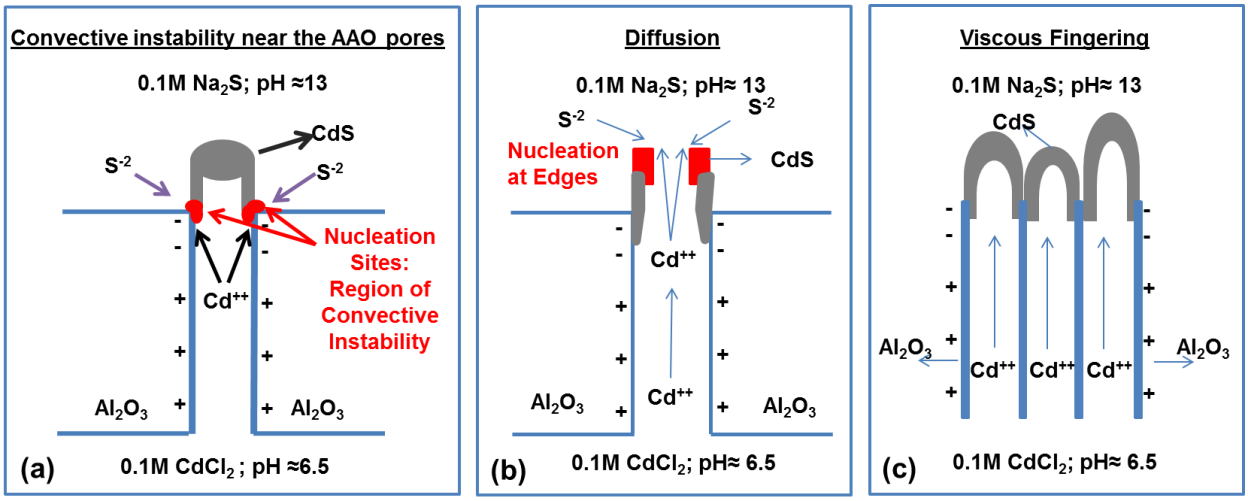

Figure 3.6: Three possible growth mechanisms for CdS nanotubes. (a) Schematic diagram shows presence of convective interfacial instabilities near the peripheral end of AAO nanochannels with CdS junction where the nucleation process happen. (b) Diffusion of Cd^{++} responsible for nucleation at the edges of these open ended nanotubes. (c) Viscous fingering effect nucleated by the ordered nanopores of AAO which can result in self-assembled growth of CdS nanotubes.

3.4.4 Need for hydrodynamic instabilities for sustained nucleation

Any laminar flow of cadmium ions at the exit point of AAO will not sustain such elongation of CdS nanotubes [as seen in figure 3.4] for few hours. Solid formation of CdS [figure 3.6(a)] can physically separate the two precursor solutions and block further intermixing of chemical precursors essential for the growth of CdS nanotubes at the periphery of porous alumina. For further elongation of nanotubes, there is a need of active presence of convective instabilities at liquid-liquid [$CdCl_2$-Na_2S] reactive interface around the peripheral edges of AAO nanochannels. This can continually drive the cadmium and sulfide ions to mix near the periphery of porous alumina [see figure 3.7] and react to form solid CdS nanotubes. As discussed in section 1.16, these types of instabilities are sustained by local variation of surface tension and also with viscosity gradients. However, these chemical precursors with different values of pH may also result in surface tension gradients as well as viscosity gradients of both $CdCl_2$ and Na_2S precursors around this reactive periphery due to ongoing chemical reaction. Additionally, this

strongly exothermic chemical reaction between these precursors can also contribute to the variation of local temperature and concentration gradients of solutes at the interface. It is possible that it can continue to drive such instability. We will discuss more about this in Section 3.4.5. As from the figure 3.6 (a) and 3.7, such gradients can vary from the center of nanochannels and drag more Cd ions towards the peripheral edges of AAO.

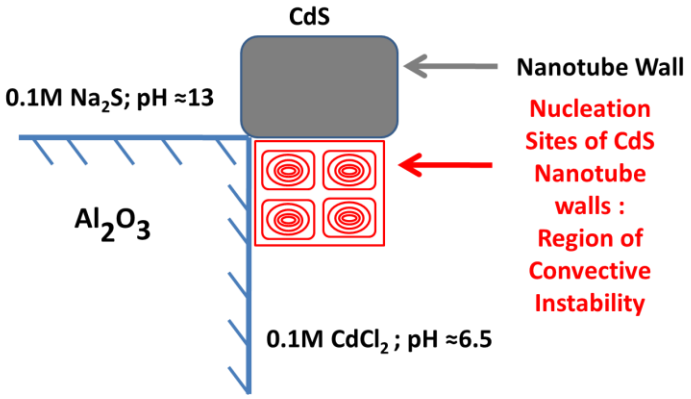

Figure 3.7: Schematic diagram of suggested convective interfacial instability at the liquid-liquid reactive interface consisting of Na_2S and $CdCl_2$ solutions and CdS particulates. A large portion of this instability may reside inside the $CdCl_2$ precursor solution because of its low viscosity. Sustained nucleation of CdS nanotubes requires the intermixing of the reactants by such convective interfacial instability.

To sustain such instability there is a need of convective process near the peripheral edges of AAO pores to efficiently drive the chemical precursors and thereby intermixing. This type of convective motion of $CdCl_2$ and mixing of precursors is necessary for prolonged [few hours] elongation of nanotubes. Such instability of chemo-hydrodynamic [section 1.16] origin can result in differential shear and generate vortices around the reactive periphery interface of AAO. We assume that most of the convective instability [vortices] may exist in $CdCl_2$ side of reactive interface [figure 3.7] due to its reasonably lesser viscosity and lower pH [Section 3.4.2]. It may possible that the wall thickness [~20 nm] of these CdS nanotubes visible on the edges of AAO may be connected to characteristic size of hydrodynamic instability, which can define the mixing area of precursors and finally react to from CdS. So we expect, this hydrodynamic instability can sustain the continuous nucleation process at AAO interface having multi-fluid components

composed of i) Na_2S ii) $CdCl_2$ precursor solutions and also iii) CdS particulates in solution phase. However, it is important to investigate and come up with rigorous quantitative analysis to prove such hydrodynamic instability at such small length scales. Further work in this direction will be presented in Chapter 4.

3.4.5 Conventional description may not be sufficient to explain the occurrence of instabilities at nanoscale

In order to understand hydrodynamic instability at small scale, we begin by ignoring the role of buoyancy induced Rayleigh type[39,43] instabilities. These instabilities usually can result in visible undulation of wall thickness on all sides of CdS nanotubes during the horizontal growth process, which is not observed in FESEM images. Subsequently as discussed in section 1.16, we thought of Benard-Marangoni[39] instability at peripheral reactive interface as a plausible reason for the nucleation of CdS nanotubes. In order to probe the reasons for such instability, we looked at the wall thickness of these nanotubes at different molar concentration of chemical precursors [figures 3.3 (a) and 3.3 (d)] and observed a negligible change in the width. This may indicate that temperature induced Marangoni type instability may be playing a major role as compared to instability induced by concentration gradients. These gradients of temperature can easily come from following sources: (i) Heat generated during CdS formation[125] [ΔH_{CdS} = -161.9 kJ/mol [exothermic reaction]] as well as (ii) aggregation of CdS particulates dispersed in solution phase to form CdS nanotubes. This localized increment in temperature by exothermic reaction may be a plausible triggering force that sustains hydrodynamic instabilities of this type, which can help to mix the reactants continuously and elongation of CdS nanotubes for few hours. However, local variation of temperature will be negligible for tubular growth of CdS in dilute concentration of reactants as shown in figure 3.3 (d).

Similarly there are reports[52,126,127] on interfacial instabilities of chemo-hydrodynamic origin driven by exothermic chemical reactions. It is known that, nonequilibrium coupling[127] of chemical reactions and hydrodynamic fluctuations can initiate interfacial convective instability. In this case, the strongly reactive interface of chemical precursors can act as a chemical generator to locally destabilize the fluid flow. There are reports[127] on similar exothermic reactions, which

can sustain instabilities and can leads to pattern formation similar to viscous fingering. Therefore, chemo-hydrodynamic coupling at the nanoscale as a consequence of the reactive nature of fluid components may be plausible reason for such convective instability at interface. Likewise, both thermal and concentration induced instability can add to the initial chemo-hydrodynamic influence, which is the trigger force for the necessary mass flow across the reactive interface to sustain such nanotubular growth.

To get a better picture on hydrodynamic instability, which is necessary for prolonged nucleation of CdS nanotubes, conventional Marangoni number [section 1.16.1] is used to estimate the presence of convective instability. We use the standard parameter of NaCl-water solution as a reference to predict the onset of such convective instabilities in a similar salt solution of [e.g., $CdCl_2$, etc] confined in AAO nanochannels. To estimate the Marangoni number [equation 1.17], the average diameter of AAO pores is taken as fluid thickness [h]. We use typical bulk or macroscopic values such as thermal gradient[51] of surface tension where $\sigma_T = \frac{\partial \gamma}{\partial T}$ = 0.161 x 10^{-3} N/m K for a NaCl-water mixture, ΔT = 1 K, h = 100 nm, dynamic viscosity μ = 0.798 x 10^{-3} N s/m^2, and diffusivity κ = 1.467 x 10^{-7} m^2/s for further calculations. However, the estimated value of the thermal Marangoni number (M_{Th}) is around ~ 0.137 which is much smaller than the usual critical value of M_C= 80 required for the onset of such classical fluid dynamical instabilities.

Also in an extreme case of insulating boundaries the mass of CdS by-product produced and the mass of heated portion by exothermic chemical reaction, however small but nearly the same. In order to estimate the thermal gradients, we start with calculating exothermic heat of reaction ΔH_{Total} for $CdCl_2 + Na_2S = CdS + 2NaCl$ using values such as ΔH_{CdS} = -161.9 kJ/mol, $\Delta H_{CdCl_2} = -391.5\,\mathrm{kJ/mol}$, $\Delta H_{Na_2S} = -364.8\,\mathrm{kJ/mol}$, and $\Delta H_{NaCl} = -411\,\mathrm{kJ/mol}$, which is found to be -226.7 kJ/mol = 1.117 kJ/g. Furthermore by using $\Delta Q = ms\Delta T$, the heat produced (ΔQ) during the formation of 1.4 x 10^{-17} g of CdS (estimated from 0.1M concentration in 100 nm^3 volume of porous alumina) is estimated using ΔH_{Total} and found to be around 1.57 x 10^{-14} J. Similarly we use the mass (m=10^{-15} g) of water located in 100 nm^3 volume of porous alumina and specific heat (s) of water as 4.1813 J/g K. By using all the above value, our rough estimate of ΔT is around 3.7 K. Finally, the estimated value of thermal Marangoni number (M_{Th}) is around

~ 0.50 and still less than critical threshold instability number (M_C = 80). Similar estimates of Marangoni number on nanofilms[48] are found to be around 10^{-8} and it is usually difficult to predict any convective instability at nanometer length scales using these instability threshold numbers. Chemo-hydrodynamic driven instability at nanoscale may not be addressable from the classical description of Marangoni type dimensionless number to predict the conditions required for instability. However, it is also possible that the values of surface tension, viscosity, and thermal diffusivity are varying with size[128,129] to initiate such instability. Interestingly, at small length scales this fluid dynamical instability may be influenced by surface tension gradient, as well as the viscosity gradient, which is mostly affected by the rate of interfacial chemical reactions. To understand the instability in this case, we can equate the reaction rate to evaporation rate of liquid-gas interface, which usually observed in Marangoni effects. In the same manner, liquid-liquid interface having reactive precursors can also result in a strong convective motion and thereby the growth.

As discussed in section 1.16.2, it is also possible that viscous fingering effect[127,130,131] at the miscible fluid-fluid reactive interface can be self-assembled and nucleated by nanopores of AAO template. This can start only if the particular ion diffuse faster through an interface between two fluids and react with other precursor ions. Therefore, chemical kinetics and the difference[131,132] in diffusion coefficients of ions is necessary [figure 6(c)] to initiate such structural growth of CdS nanotubes by a similar way. However, to sustain such tubular growth, there is a need of continued nucleation process happening at peripheral edges of these nanotubes located on the surface of porous alumina. From these observations, we still argue in favor of chemo-hydrodynamic instability occurring at junction between CdS nanotube and AAO nanochannel as the driving force for such sustained nanotubular growth of CdS. It is hard to separate and estimate quantitatively the individual contributions of different convective interfacial instabilities occurring at AAO-multicomponent reactive interface.

It has been noted in fluid-fluid interface[131,132] that chemo-hydrodynamic influence can not only add to the existing viscous fingering instability but they can also initiate one, which may depends on relative viscous parameters of the reactive fluids. Therefore, it is true to argue that chemical kinetics can affect both the surface tension and viscosity gradient in the surrounding area of reactive interface which subsequently can lead to chemo-hydrodynamic instability at such

small length scales. These well-ordered growths of nanotubular CdS requires a deep understanding on growth process with the help of theoretical modeling, which can take care of the nucleation and structural growth at nanoscale. Detailed quantitative estimates of such multi-component reactive flow of reactants inside these nanochannels and thereby convection of chemo-hydrodynamic origin along with tubular growth process is surely needed at this stage.

3. 5 Summary

In summary, we presented the structural evidence to understand the role of hydrodynamics in nanotubular growth process of CdS oriented in one direction, where nanochannels of porous alumina were used as a nanochemical reactor in the synthesis process. Using two chamber nanofabrication processes, we reported a directional asymmetric growth of CdS nanotubes only on one side of porous alumina facing Na_2S solution. We also discussed the role of dissimilar flow rates through the alumina nanochannels, which is responsible for such one sided growth. We also identified the nucleation sites at AAO-Na_2S interface for the further elongation of nanotubes. We demonstrated the presence of strong chemo-hydrodynamic coupling as a plausible cause for the sustained nucleation of nanotubes for few hours. We also argued in favor of chemo-hydrodynamically driven instability at the AAO-Na_2S reactive interface as mostly the mechanism for such sustained horizontal growth of CdS nanotubes. However, preliminary estimates imply that the usual description of hydrodynamic instabilities [e.g., Marangoni effects, etc] cannot account for the onset of such instabilities at the nanoscale. Therefore, all these results and analyses need more experimental and theoretical works to prove the interconnected roles of hydrodynamics and chemistry in the nanoscale growth mechanism. Further studies done in this direction will be discussed in the next chapter.

Chapter 4

Understanding the Role of Hydrodynamics in Nanofabrication

4.1 Introduction

Most nanomaterial synthesis and self-assembled nanofabrication routes, specifically the wet chemical ones actually take place in a fluid medium. However, the precise function of fluid dynamics in nanofabrication process still remains a difficult challenge. Hydrodynamics at the interface as well as the chemical nature of two different reacting liquids both can play important role in nanofabrication of solid structures. In general, for micro/nanochannels[31,32,38], it is usually believed that the mixing of two different chemicals/fluids is governed by traditional diffusion process only where molecules undergo some sort of random walk. This is because one generally tends to directly extrapolate the usual dimensional arguments characterized by dimensionless numbers valid in large scale [mm to meter range] to very large scale [few to many km] fluid motions to such small nanometer length scales and then by default tend to conclude that the advective mixing of two fluids is mostly negligible. As described in the first chapter, these smaller nanochannels are expected to have laminar type of flow only and there is hardly any notion of turbulence and instability formation as per the existing classical fluid dynamics theory. However, we have indicated in the last chapter that sustained mixing of chemical solutions through nanochannels may require presence of instability or turbulence for advection dominated fluid flow too. Therefore, further experiments were necessary to directly prove the scalability of standard fluid dynamics in nanostructural growth process and also to understand the possible role of chemo-hydrodynamic convective instability for nanotubular growth at the porous alumina-Na_2S interface.

From our experimental observations, this chapter will discuss why a nominal diffusion process alone may not be sufficient to explain the sustained growth elongation of CdS nanotubes at the porous alumina-Na_2S interface. First in section 4.2, we start with a brief description of the simple diffusion based models which tried to explain our nanofabrication results[109]. Then we

describe some experiments to further probe the reason behind such type of prolonged nucleation and also to obtain a picture how the fluid dynamics as well as chemical reactants are interconnected in this nanofabrication process. If the nanochannels of nanoporous alumina get clogged with the formation of solid CdS, then the two reactants no longer mix and further growth of CdS nanotubes can actually stop. The fact that these nanotubes continues to grow from only one side of the AAO template may indicate that chemo-hydrodynamic forces can play a significant role in sustained mixings of the reactants inside such smaller nanochannels. To understand such growth process, we measured the length of these nanotubes and most importantly observed some type of ever increasing 'runaway growth rate' with increasing time duration. Similarly length of these CdS nanotubes also increases with decreasing nanochannel diameter. We will present some results in section 4.4 to show how particular chemicals are playing different roles for such type of nanoconfined growth and observed that Na_2S have a major role in such nanotubular growth of CdS for extended duration. We will also show in section 4.5 that this type of nanotubular growth is possible even in the presence of surfactants which are typically used during the synthesis of CdS nanoparticles capped with organic ligands. Finally, we will argue that still there is a need for deeper understanding of such growth process based on fluid dynamical aspects and also how the chemical reactions are involved in tuning this.

4.2 What is the role of diffusion?

Usually in nano and micro channels, mixing of the fluids and subsequent reaction of chemicals are known to be mainly controlled by diffusion [section 1.15.1]. As discussed in section 1.15.3, rough estimate of peclet no [Pe] for precursors passing through the channels with a speed of 10 μm/s lies in the range of 0.01[133] or even can go very small with less speed[31,32]. As per classical fluid dynamics, advection induced mixing can be dominant over diffusion process only if the fluid moves with a speed much greater than 10^5 μm/s through these smaller nanochannels. External forces [high electric field, pressure etc] are usually required for enhancing the mixing of chemicals[31,32,38] or fluids across these nanochannels. However, these external forces can also create a convective instability at the interface [section 1.16]. The aim of

our investigation is to understand whether chemo-hydrodynamic forces at nanoscale are playing any such role similar to these external forces.

Considerable amount of theoretical modeling were done based on our work[109]. There are few recent reports[133,134] of theoretical investigations to explain our nanoreactor based self-assembly of ligand free CdS nanotubes. All of these reports used simple diffusion based models relying on some ad hoc assumption of nanochannel induced one directional flow of cadmium ions along with reaction-diffusion dynamics, which can lead to ordered cylindrical structures. They used different values for density and diffusion constants for both the precursor ions to study the mechanism of nanotube formation. Their work primarily requires a jet like strongly diffusive flow of Cd^{++} ions trough AAO nanochannels and then how this faster flow interacts with slower but diffusive S^{--} ions to form CdS nanotubes. Finally, CdS material, so formed by a combination of diffusion-reaction process, aggregate in cylindrical shaped structures. Reasons for such tube like formation of CdS are mainly due to presence of faster Cd^{++} ions along the nanochannel axis which drives the growth elongation and also due to the deficiency of S^{--} ions at the center due its slow lateral diffusion. They extended the work[134] to further understand the influence of other neighboring nanotube nucleation sites on individual growth sites. According to this model, after certain growth duration, there can be a deficiency of sulfur ion at AAO interface and thereby preventing further growth. However, we will see that our experimental results cannot be fully be explained by these diffusion based growth mechanism as discussed in section 4.3. Moreover, we will also argue in chapter 6 that based on electronic structure calculation it is reasonable to expect that these CdS nanotubes will have a dominant presence of sulfur interstitials on the surface as compared to the sulfur deficiency predicted by these diffusion based models.

4.3 Effect of increasing growth rate of nanotubes – does it signify the presence of fluid dynamical instability?

As per the simplistic diffusion based models described in the last section, it is apparent that the crucial assumption of this jet like outward flow of cadmium precursors is actually responsible for the tube like elongation of CdS nanostructure. However, for sustained growth, spanning over few hours, this increasing bulk of the CdS nanotubes have to be pushed outward to make space

for mixing of precursors and consequent horizontal growth nucleation of nanotubes at the periphery of AAO nanochannels. It is apparent that this jet like flow of cadmium ions has to gradually slow down as a result of the increasing bulk of solid CdS nanotube structures which is always blocking such flow. Therefore, any slowdown in the jet like flow of cadmium ions will also slow down the growth elongation of ligand free CdS nanotubes with time. In order to understand these more qualitatively, we did some experiments to study how the length of these nanotubes is actually varying with growth duration and also with diameter of porous alumina nanochannels.

To study the growth rate, we used AAO nanochannels having diameters around 100 nm and also maintained the same concentration [0.1M] of precursors on both side. Length of these CdS nanotube prepared at different time durations was measured ex-situ using FESEM. Interestingly from figure 4.1(a), we notice an increasing length of these nanotubes with growth duration. Moreover, in figure 4.1(b), we see that the growth rate also increases in complete contradiction with the simplistic diffusion based models. In those theoretical models, the ad hoc requirement of jet like flows of Cd^{++} from AAO nanochannels into Na_2S bath actually drives the horizontal growth nucleation and can eventually slow down with time due to reasons mentioned above. In fluid dynamics, any kind of unstable equilibrium is characterized by the dynamics of the system irreversibly moving away from the equilibrium point. Therefore, every onset of fluid dynamical instability or turbulence is also characterized by similar runway time evolution of small perturbation[135]. By studying the observed runaway growth rate of CdS nanotubes, we comprehend that such runaway growth will also require ever increasing supply of chemical precursors towards the nucleation sites. We further extend this argument to understand that the modulus of amplitude of the velocity flow of precursor ions towards the nucleation center most likely tends to increase steadily with time which eventually can lead to the disruption of steady and laminar flow and result in instability during growth nucleation.

Therefore, we propose that our results in figure 4.1(b) certainly indicates the presence of similar runaway instability in the form of ever increasing growth rate during sustained nucleation of these CdS Nanotubes. Therefore it seems clear that such nanofabrication need not always be explained in terms of simplistic diffusion based models only. However, it is also important to

consider whether any enhanced rate of fluid flow from these nanochannels can lead to higher rate of chemical reactions and thereby lead to higher growth rate of CdS nanotubes from the AAO-Na_2S interface. In smaller nanochannels, instability at interface can be observed from the non-linear behavior of current[58,59] with applied voltage [10-100 V] and similarly we hypothesize that the nonlinear growth shown in figure 4.1(a) and 4.1(b) may also be a signature of such instability only. Whether this increasing growth rate can actually relate to some signature of instability is still to be probed in detail. Further work is going on to gain quantitative understanding of such growth process based on possible presence of chemo-hydrodynamic triggered instability.

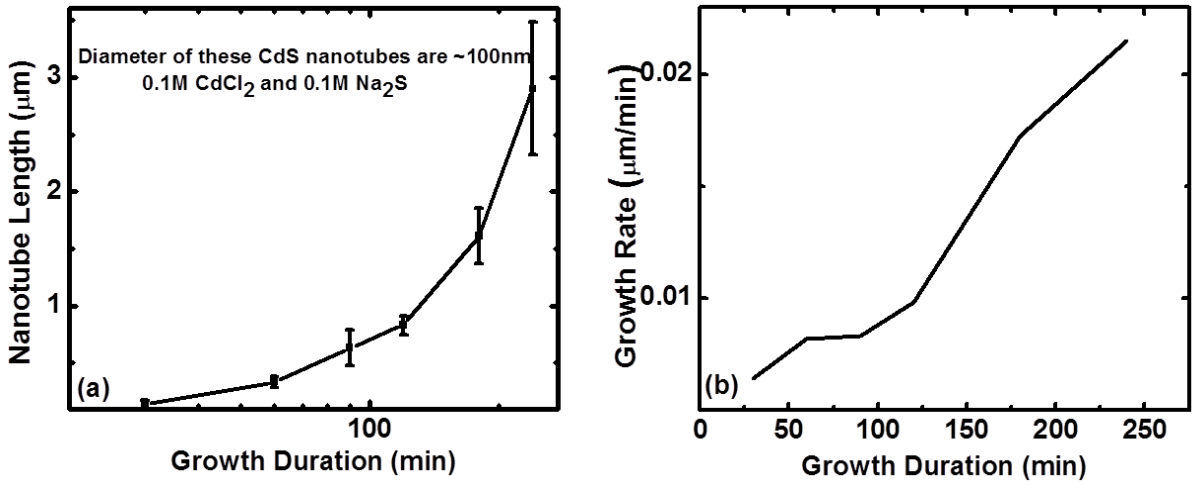

Figure 4.1: a) Shows an increased length of nanotubes with time duration b) Growth rate of nanotubes. Length of these nanotubes is measured using scanning electron microscopy images. These growth rates suggest that diffusion itself is not enough to explain the nanotubular growth.

In addition to these results, we also observed that the length of these nanotubes increases with decreasing AAO diameter, while keeping the growth duration and concentration of reactants same. Results are shown in figure 4.2. For normal flows, flow resistance of fluids usually increase with decreasing cross sectional area of the tube/channel except possibly in cases of surface tension mediated capillary flow. However, the dimensions of our AAO nanochannels (20-100 nm) are much bigger compared to any flow guided by electric-double layer at the inner walls of the channels. This is because the characteristic Debye length [< 1 nm] of reactant fluid

at such [say 0.1M] concentrations is very small. Therefore we need to probe this result in more detail to understand the possible origin of Cd^{++} jet in the first place.

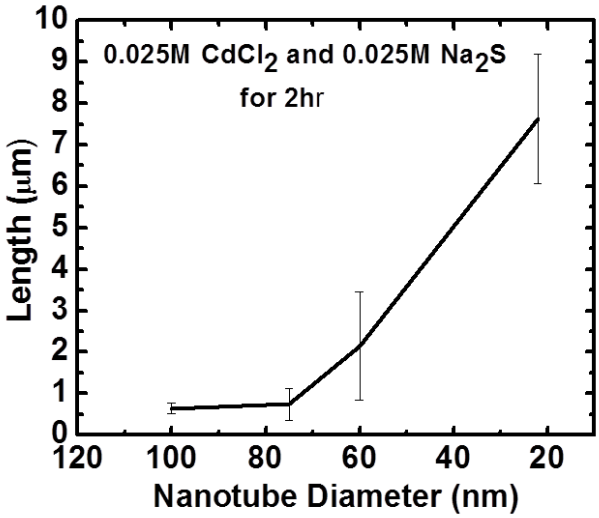

Figure 4.2: Decreasing size of nanochannels can lead to increasing growth as compared to bigger nanochannels. This growth needs more understanding from the aspects of crystal growth and also from hydrodynamic influence.

4.4 Role of precursors in chemo-hydrodynamic cause for growth nucleation

As usual, chemical concentration can play an important role in the observed 'runaway' flow of precursors and thereby affect the growth process of CdS nanotubes. Simple experiments are done to identify the functions of each precursor. Concentration of precursors for CdS nanotube fabrication is varied by keeping the opposite one at a constant concentration [0.1 M]. It is evident from the length of CdS nanotubes measured using FESEM images as shown in figure 4.3(a) that concentration of Na_2S significantly influences the growth of these CdS nanotubes. The growth elongation increases sharply at smaller concentrations before saturating around Na_2S concentrations of 0.1M. On the other hand, increasing concentration of $CdCl_2$ till 0.5M is hardly affecting the growth of CdS nanotubes. This indicates that concentration of sulfide ions [S^{--}] is certainly playing an important role in such type of nanotubular growth as compared to that of Cd^{++} ions. According to the diffusion based models[133,134], we expect that the amount of Cd^{++} in the incoming jet inside the active nucleation sites to decrease with decreasing Cd^{++} concentration.

It is not at all unreasonable to argue that this decrease in Cd^{++} concentration can reduce the growth rate. However, experiments shows that the growth of CdS nanotubes is hardly dependent on this concentration and this may point towards some inherent inconsistency of the diffusion based models having such ad hoc assumptions of Cd^{++} jet driving the growth as described earlier. Further experimental and computational work is being planned to fully explain such growth process.

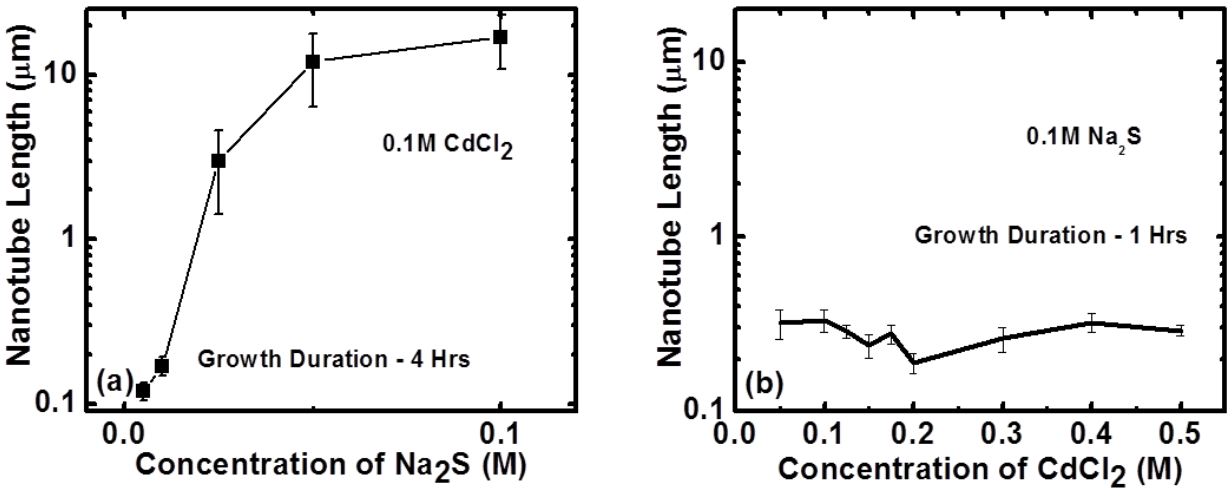

Figure 4.3: a) Length of CdS nanotubes is varying with increasing concentration of Na_2S while the $CdCl_2$ concentration was kept constant 0.1M. b) Figure shows growth rate of CdS nanotubes is not much affected by increasing $CdCl_2$ concentration. Overall growth is mostly controlled by Na_2S concentration only.

4.5 Effect of surfactants on CdS nanotubular growth

In general, surfactants are used to produce smaller nanoparticles[2,3] and their size as well as structure formation depends on the concentration of surfactant used. In most of our work with CdS nanotubes, we have not used any surfactants and the CdS nanotube clusters grown on nanoporous AAO can be categorized as ligand free nanotubes. However, in one experiment we used a surfactant named thioglycerol [TG][136]. TG is usually used as capping agents during the synthesis of CdS nanoparticles. Here we added TG into the precursors and studied its effect on nanotubular growth. Figure 4.4 and 4.5 shows the nanotubular growth of TG added only to one

of the precursors [$CdCl_2$ or Na_2S] in nanoreactor based synthesis route. One problem in adding TG to Na_2S is the formation of H_2S which can decrease the concentration of S^{--} ions and thereby the growth. We observed stronger growth of CdS nanotubes in the case of TG added to $CdCl_2$ side, whereas in the other case of adding TG only to Na_2S side shows a lesser growth. Even though TG added only to Na_2S side can affect the growth rate [by comparing figure 4.4(b) & 4.5(a)] due to reduced S^{--} [H_2S formation], but it not altering the tubular growth process. So we can conclude that the addition of TG is not affecting the nanotubular growth process.

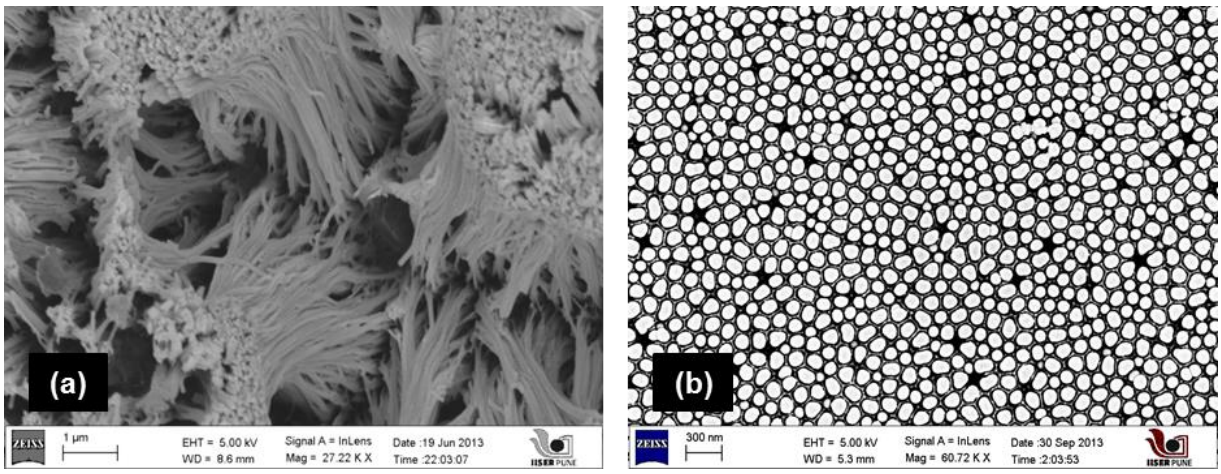

Figure 4.4: Nanotubular growth of CdS is also possible with capping agent (TG) added to the fabrication setup. a) 0.01M $CdCl_2$ is mixed with 0.05 M TG while we keep only 0.01M Na_2S on the other side of AAO and the reaction continues for 30minutes , b) 0.01 M TG is added only to 0.01M Na_2S while we keep 0.01M $CdCl_2$ on the other side of AAO and the reaction continues for 3 hours.

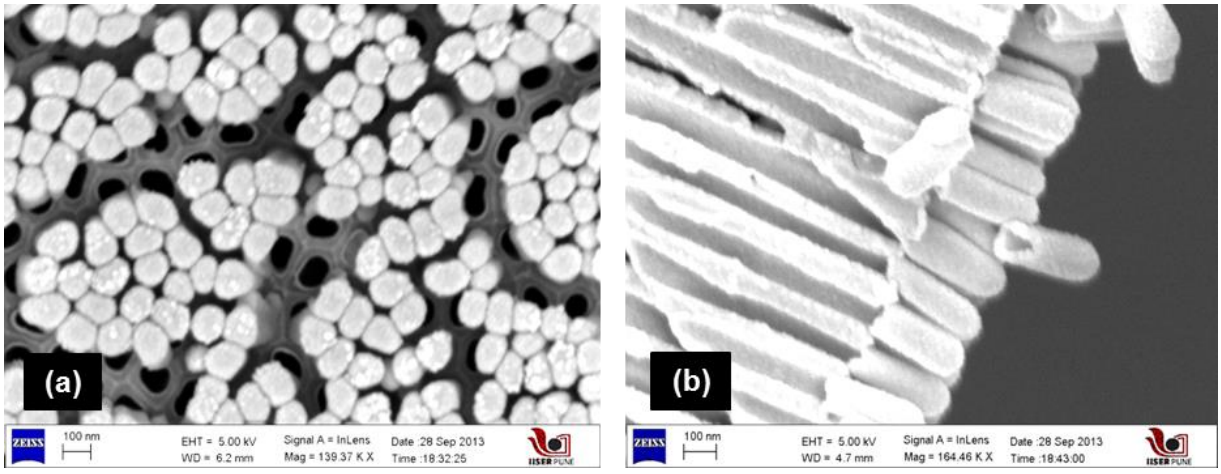

Figure 4.5: (a) & (b) Dilute concentration [0.001 M] of TG is added to 0.01M Na_2S only while we keep 0.01M $CdCl_2$ on the other side for 3 hours, nanotubular growth of CdS is clearly visible.

4.6 Summary

This chapter had given us some idea why simple diffusion based alone is not enough to explain the nanotubular growth of CdS on porous alumina. We argued that - 1) runaway increase in growth rate of CdS nanotubes is qualitatively similar to runaway time evolution of small disturbance away from equilibrium which ultimately lead to the destruction of laminar flow, 2) independence of growth rate on the concentration of $CdCl_2$ and its strong dependence of the concentration Na_2S may indicate limitations of diffusion based models with a jet like flow of Cd^{++}, and 3) finally we will show in chapter 6[137] that we expect a dominant presence of sulfur interstitials on the surface as compared to sulfur deficiency predicted by such diffusion based processes. Further work is being planned to acquire comprehensive quantitative estimates of chemo-hydrodynamic triggers for such nanoscale self-assembly of ligand free CdS nanotubes.

Chapter 5

Enhanced Photoluminescence from Ligand Free CdS Nanotubes

5.1 Introduction

Quality of ligand free CdS nanotubes can be identified from its structural and optical properties. Usually band gap of CdS nanostructures is determined using absorption spectroscopy and its optical emission quality by photoluminescence measurements. It is also well known that defect states from ionic vacancies on CdS surface plays a crucial role in controlling the optical emission from these nanostructures by trapping photo generated charge carriers. Enhancement of optical emission is typically observed for smaller nanostructures synthesized in solution mode by neutralizing the surface trap states with surfactants. These surfactants usually determine the size of nanostructure grown in particular geometry and also selectively block non-radiative recombination centers and thereby improving the optical quality of these nanostructures. However these semi-insulating organic surfactant molecules attached on the surface of nanostructures can actually resist the flow of charge carriers and limit the operational efficiency of the use of such nanostructures in optoelectronic devices.

In this chapter, we compared the photoluminescence of surfactant/ligand free CdS nanotubes grown on porous alumina with nanocrystalline cadmium sulfide particles prepared by bulk mixing of same reactants and observed a much enhanced PL in nanotubes. Unidirectional structure of these nanotubes and lesser number of non-radiative recombination centers as compared to nanocrystalline CdS drop casted on glass plate may be the reason for such enhancement. We will discuss the PL process based on the structural aspects as well as role of defects in CdS nanotubes. Size of these CdS nanotubes [wall thickness ~15-20 nm] are much above quantum confinement regime of few nanometers and can be studied on the basis of classical semiconductor theory. Later in chapter 6, we will see that electronic defects originated due to cadmium vacancy on the surface of these CdS nanotubes are playing a major role in the PL process and also for red shifting the PL peak position with increasing size.

5.2 Absorption and photoluminescence measurement

5.2.1 Absorption spectrum

Optical absorption region of these ordered arrays of CdS nanotubes are studied with the help of Perkin Elmer's Lambda 950 spectrophotometer. As discussed in section 2.3 and 2.5, CdS nanotubes grown on porous alumina of size 100 nm, which is more or less transparent, can be used for absorption studies. Absorption is measured for this sample at scan steps of 1 nm from 800 nm to 400 nm. Figure 5.1(a) shows the absorption spectra of 100 nm CdS nanotubes attached to porous alumina. Similarly for comparing the photoluminescence of these nanotubes, we prepared CdS nanocrystallites prepared by reaction of same two precursors [0.1M $CdCl_2$ & Na_2S] in aqueous solution and finally drop casted on a glass. Figure 5.1(a) shows the absorption spectra of CdS nanocrystallites drop casted on glass substrate. These two samples having similar absorbance at energy 2.95 eV were used for exciting the CdS sample for photoluminescence measurements. Effective optical band gap of CdS nanotubes is estimated to be around 2.38 eV using Tauc plot[115,116] [section 2.5.2] as seen from Figure 5.1(b), which is very close to the bulk band gap of CdS. Similarly for CdS nanocrystallites having sharp absorption edge [figure 5.1(a)], the band gap is estimated around ~2.4 eV.

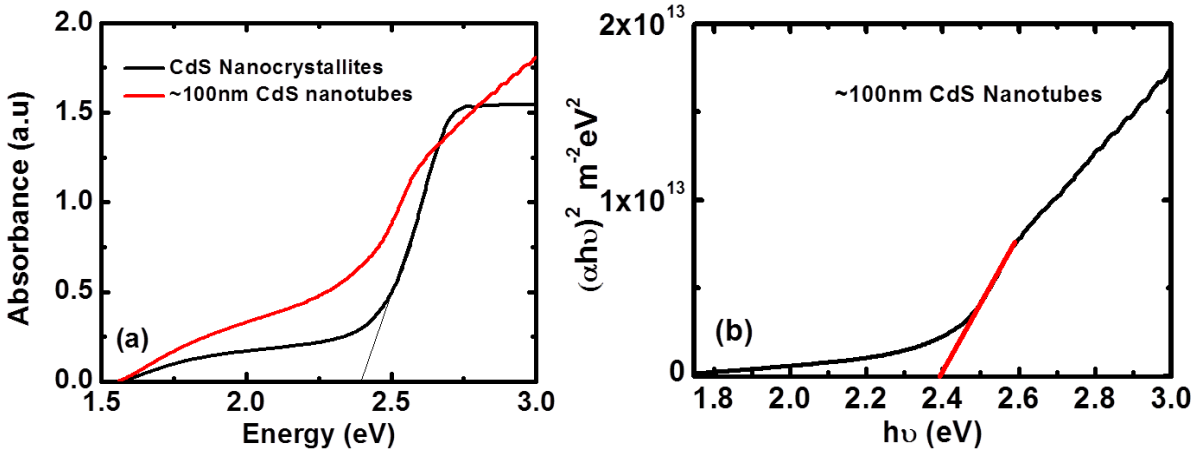

Figure 5.1: (a) shows the absorption spectra of CdS nanotubes on porous alumina and CdS nanocrystallites drop casted on glass. (b) Band gap estimation of CdS nanotubes using Tauc plot.

5.2.2 Enhanced photoluminescence

Photoluminescence spectra are measured using Horiba Jobin Yvon's Steady-State Spectro-fluorometer with scan steps of 1 nm for CdS nanotubes having diameters around 100 nm and also for CdS nanocrystallites drop casted on glass. These two samples are excited with photons having wavelength of ~420 nm [~2.95 eV] which is much above the band gap for both CdS nanostructures. Figure 5.2, shows the photoluminescence spectrum of CdS nanotubes grown on AAO template and also from the CdS nanocrystallites synthesized by simple reaction of two chemical precursors [0.1M $CdCl_2$ & Na_2S] in a beaker at room temperature. More interestingly, we observed an enhanced photoluminescence[110] from CdS nanotubes as compared to CdS nanocrystallites formed via bulk mixing and drop casted on glass, which is visible in figure 5.2. In this comparison of photoluminescence yield, we made sure that both the materials have nearly the same absorbance at 2.95 eV. Also it is clearly visible that the photoluminescence peak of CdS nanotubes is slightly blue shifted from that of CdS nanocrystals. Later we compare the structural as well as atomic composition of the material to understand the enhanced photoluminescence.

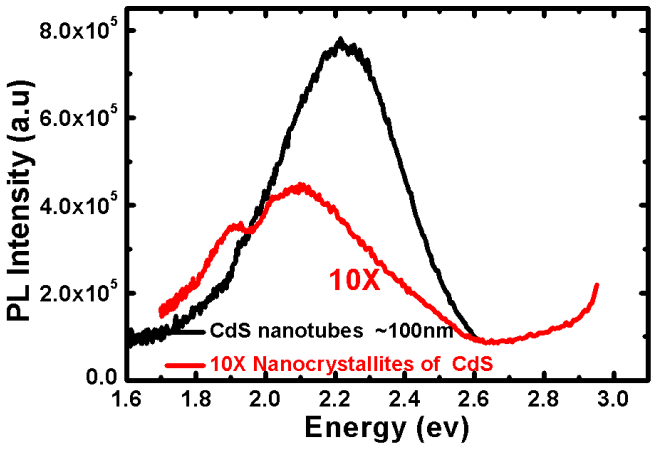

Figure 5.2: Comparison shows that the photoluminescence intensity of CdS nanotubes is much higher than that of CdS nanocrystallites having similar absorbance. The photoluminescence intensity of CdS nanocrystallites shown in the plot is multiplied by a factor of 10.The photo-excitation energy for luminescence was 2.95 eV (420 nm).

Comparing figures 5.1 and 5.2 clearly shows a red shift in PL emission peak from the absorption edge due to the participation of electronic defects[4,63] in trapping the excited charge carriers for radiative process inside these nanotubes. These defects can certainly alter the efficiency of light emission and there by quantum efficiency of nanotubes. Moreover, PL can be also affected by inbuilt strain in CdS nanotube during its growth process. We discuss these in more detail in chapter 6.

5.3 Role of defects in CdS nanotubes

CdS nanostructures with different shapes and defects states are widely studied in the past and observed that optical emission from CdS is red shifted from the absorption edge due to the presence of shallow defect energy levels[82,83,93] near the band gap. Excess cadmium or sulfur vacancy energy levels are located within 0.4 eV-0.7 eV below the conduction band edge of CdS. This usually leads to yellow emission around 2.0 eV-2.2 eV. Cadmium vacancies in CdS can lead to emission around 1.2 eV as discussed in section 1.19. It is clear from PL spectra that the peak emission maximum lies around 2.2 eV and it is very well matching with the sulfur vacancy[82,83,93] related optical emission process observed from CdS. In order to investigate the origin of this yellow photoluminescence band even further, we studied elemental composition of CdS nanotubes using energy dispersive X-ray spectroscopy [EDS] with Oxford Inca 80 mm^2 drift detector mounted on a Carl Zeiss Ultra Plus FESEM [Figure 5.3].

From the elemental composition studies, we observed that elemental sulfur [22.7%] is in a smaller stoichiometric ratio in the bulk of these ~100 nm CdS nanotubes as compared to elemental cadmium [30.0%] with an estimated S/Cd atomic ratio [figure 5.3] ~0.75. We observed an overall sulfur deficiency of ~100 nm wide CdS nanotubes, which typically varies in the range 0.7 to 0.9 within the samples used in this study. For CdS nanocrystallite particle, this S/Cd atomic ratio however, always remains well in a stoichiometric balance. This clearly shows that electronic defect states associated with the observed composition difference are playing key roles in radiative recombination and also affects broadening the photoluminescence peak. It is also well established that radiative emission from CdS nanoparticles prepared in aqueous solution is dominated by defects at the surfaces.

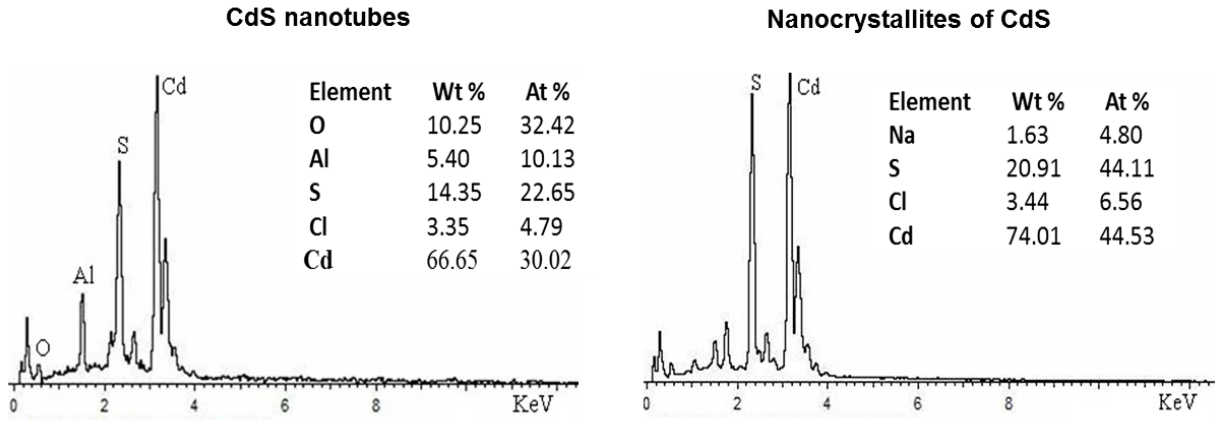

Figure 5.3: EDS spectra measured for CdS nanotubes having outer diameter 100 nm and CdS nanocrystallites. Presence of more elemental cadmium than sulfur in these nanotubes is clearly visible

From the preliminary results on CdS, one intend to think that defect mediated radiative recombination process may originate from sulfur vacancy or excess of Cd^{+2} inside the bulk of CdS nanotubes. However, we know that usually the surface composition of nanostructures always play more dominant roles in radiative recombination as compared to its bulk composition. Next chapter will show how surface composition of these ligand free CdS nanotubes actually influences its light emission.

5.4 Structural characterization

Crystalline size of these nanotubes is identified [section 2.7.3] by powder x-ray diffraction [XRD] using the Bruker D8 Advanced X-ray Diffractometer with Cu-K_α x-ray radiation [0.154 nm] and scan increment of 0.01 per step. X-ray diffraction pattern as in figure 5.4 shows the standard XRD peaks corresponding to the [002], [110] and [112] planes of wurtzite crystal of CdS. More discussion on x-ray diffraction will be seen in next chapter. Crystalline size of both are determined using Debye-Scherrer method [with a shape factor K = 0.9] to the dominant [002] peak in figure 5.4. All such x-ray diffraction studies have estimated similar crystalline size ~2.5 nm, which is also close to the Bohr exciton radius of CdS, where expected quantum effect starts. One of the reasons for such small crystalline sizes as compared to the mean outer diameter of

~100 nm and the average wall thickness of ~20 nm of the nanotubes are due to the solution processed room temperature synthesis.

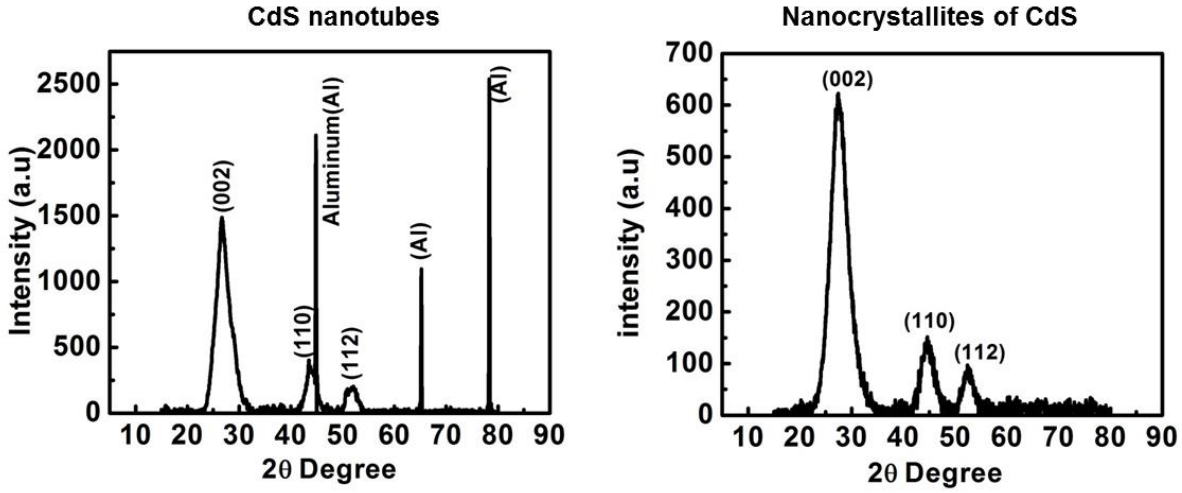

Figure 5.4: X-ray diffraction analysis of ~100nm CdS nanotubes on AAO membrane and CdS nanocrystallites. Mean crystallite size of ~ 2.5 nm was observed from these nanotubes estimated by using Debye-Scherrer method. Sharp XRD peaks of Aluminum from the AAO template are also visible.

5.5 Reasons for enhanced photoluminescence in ligand free CdS nanotubes

In general, electronic defects reduce the amount of radiative recombination or photoluminescence by trapping hole and electrons excited by light. Strain and other structural imperfections in the crystal can create such electronic defects and also reduce the same. So it is better to use capping agents or surfactants to get energetically favorable stable nanostructures which can significantly reduce the surface electronic defects and thereby enhance the photoluminescence intensity of these nanostructures. However, no such capping agents was used either in the fabrication process of CdS nanotubes or in the bulk mixing process for CdS nanocrystallites. Therefore, the strong photoluminescence yield from these CdS nanotubes is an evidence of the good optical quality of these nanostructures. Enhancement of photoluminescence from CdS nanotubes may be coming from directional nature of nanotubes as compared to agglomerated CdS nanocrystallites. This may have contributed to this enhancement through active wave guiding of the emitted light along the length of these nanotubes. These

nanocrystallites made by bulk mixing of the same reactants and then drop casted on glass may have lot of these non-radiative centers as compared to the CdS nanotubes. However, the exact connection between the optical properties of these nanostructures with their structural quality is still not clear. It is likely that the chemo-hydrodynamic influence during nucleation and growth of such nanotubes in this nanofabrication technique are also playing some vital roles in enhancing its optical properties. More details about the connection between the elemental composition and electronic defects on the surface of these CdS nanotubes will be discussed in the next chapter 6.

5.6 Summary

In this chapter, we had discussed the enhanced room temperature photoluminescence from ligand free CdS nanotubes by using our two chamber nanoreactor method. Such enhanced photoluminescence, from these ordered arrays of CdS nanotubes as compared to CdS nanocrystallites having similar crystallites sizes ~ 2.5 nm, clearly indicates better optical quality of these nanotubes. This superior optical property of these CdS nanotubes may be due to directional nature of light emission. In summary, we had clearly demonstrated that this simple two-chamber nanoreactor based synthesis technique can be a good method for fabricating ordered arrays of ligand free CdS nanotubes with nice optical quality. Further studies in this direction to pin point the nature of these surface defects influencing the PL will be presented in the next chapter

Chapter 6

Interplay of Strain and Defects in Photoluminescence Shift of Ligand Free CdS Nanotubes

6.1 Introduction

Optical properties of nanostructures and their potential applications are widely influenced by a variety of factors. It is also a well-established fact that quantum confinement of charge carriers, electronic defects in the form of vacancy and crystalline strain can tune not only the band gap but also affect the allowed energy levels available for radiative transitions and thereby change the nature of photoluminescence [PL]. There are reports on modifying the band gap and PL of nanowires[101,102,138] [CdS, ZnO] by external forces which create compressive and tensile regions within the structure. Inherent lattice strain originated during growth process of one dimensional nanostructure can also lead to tensile and compressive regions. Usually it is difficult to identify the influence of strain on defect mediated photoluminescence.

In this chapter, we investigate PL shifts[137] from ligand free CdS nanotubes having different lengths and diameters. We will identify the role of quantum confinement of charge carriers, defects and crystalline strain in a systematic way to understand the observed PL shift from these nanotubes. Most of the recent studies on CdS are focused on quantum structures and there are only very few reported works[77,100], which really deals with role of defects and strain responsible for PL shift from 1-D nanostructures of CdS beyond the usual explanation based on quantum confinement effects. Here we report[137], interplay of crystalline strain and minority cadmium vacancy defect on the surface incorporated during growth process as a major reason for such PL red shift from ligand free CdS nanotubes. Quantum confinement effects usually measured through optical absorption studies didn't show any significant shift in band gap for these nanotubes having different diameter and length. Estimation using x-ray diffraction pattern shows a systematic increase of crystalline strain with diameter and length of CdS nanotubes, which can affect the band gap and also the defect energy levels. We will also mention the necessary supporting results from density functional theoretical [DFT] calculations done by our collaborator Dr Prasenjit Ghosh to understand the individual role of defects in PL process from

these ligand free CdS nanotubes. However from structural calculations it is found that although sulfur interstitials are the most abundant ones, but it is the Cd vacancies with second lowest formation energy which are mostly participating in PL process. DFT calculations identify a systematic variation of the position of cadmium vacancy energy state with strain, which we relate to the observed red shifts of PL with increasing size of these CdS nanotubes.

6.2 Photoluminescence shift

Figure 6.1(a) shows photoluminescence spectra from CdS nanotubes having different diameters. These PL spectra were measured after photo excitation at 2.95 eV. Interestingly, PL peak positions systematically red shifts[137] over a wide range of ~0.4 eV photon energies with increasing outer diameters of these Cds nanotubes from ~20 to ~100 nm. It is well known that smaller nanostructures with size below Bohr exciton radius can show blue shift in absorption and PL due to quantum confinement effects. However, as discussed in chapter 3, the diameters [22-100 nm] as well as wall thickness [15-20 nm] of these nanotubes are much larger than the usual Bohr exciton radius of CdS [~3 nm] to have any sizable blue shift purely as a result of quantum confinement within these side walls. This leads us to study the role of defects in these nanotubes for PL shift, since quantum confinement effects may not significant. Later we will discuss the role of strain, nanocrystallite size and defects, which can also systematically influence optical properties of these nanotubes. It is well known that surface defects with distinct formation energies located at different positions within the band gap can affect the PL process.

Depending on the nature of surface trap levels introduced by cadmium or sulfur excess/vacancy in CdS nanotubes [section 1.19], PL spectrum can shift the emission peak toward yellow or red side of visible spectrum. PL from CdS nanotubes with smaller diameters [figure 6.1(a)] also show a strong emission band due to band edge emission around ~2.5 eV and other weak but even broader emission band around ~2 eV due to defects at the surface. It will be interesting to know the individual role of each defect, which may act as luminescence centers. These small structures can be influenced by quantum confinement effects and crystalline strain, it is better to understand their crucial role in PL through estimation using absorption spectrum and x-ray diffraction pattern.

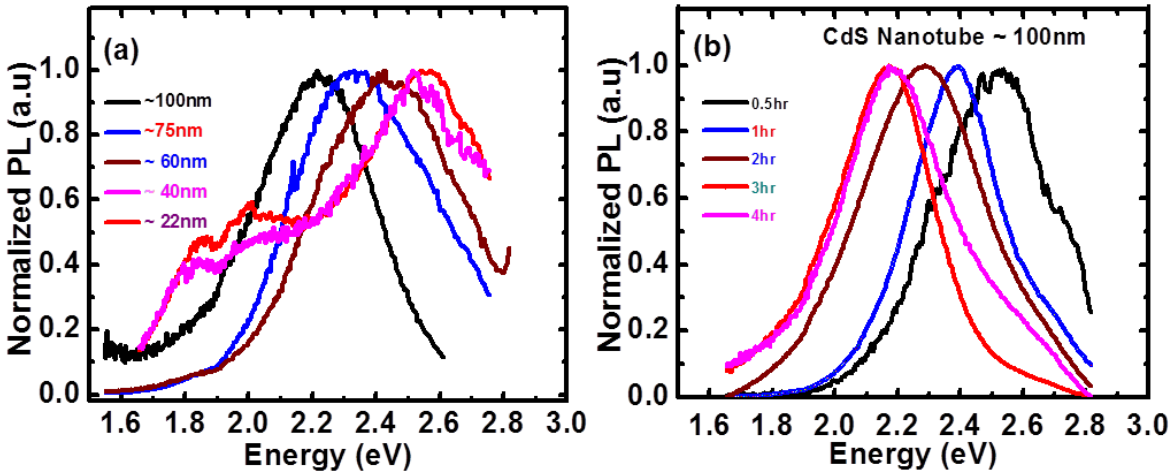

Figure 6.1 PL spectra of CdS nanotubes show a systematic shift with increasing diameter (a) and growth /length (b). It is clear from the figure that there is considerable shift in PL peak position.

Moreover, CdS nanotubes with fixed outer diameter of 100 nm but having different lengths are prepared by varying the growth duration. From FESEM images [figure 3.4] of these CdS nanotubes, as discussed in chapter 3 and 4, the length of these nanotubes also increases with increasing growth duration. Figure 6.1(b) shows the PL spectra of these ~100 nm wide CdS nanotubes grown for different duration. Similarly compared to figure 6.1(a), we can observe a red shift in PL peak position[137] with increasing length of these nanotubes. PL measured for all CdS nanotubes having different lengths are also excited at 2.95 eV.

Reported electronic defects in CdS [section 1.19] are mainly of sulfur vacancy[88] which lies in the range ~0.7 eV from the conduction band and another defect from cadmium vacancy[93] which is around ~ 1.2 eV above valence band. There are also reports of surface state defect levels lying ~0.2 - 0.4 eV[65,139] below conduction band, which are responsible for band edge emission from CdS. Without a proper understanding on the nature of these defects and their role in PL process, it is very difficult to identify and separate the individual contribution of each defect states towards the systematic red shift in PL of these ligand free CdS nanotubes. In order to probe the PL Shift, we will go further to estimate the role of quantum confinement effect within CdS nanocrystallites, defect and strain in these CdS nanotubes. This will help us to understand the overall PL process happening in these CdS nanotubes.

6.3 Optical absorption studies

To understand such PL shift, we begin with absorption studies[137] of these CdS nanotubes having different diameters and also grown at different durations having different lengths. From the absorption plot as shown in figure 6.2(a) & (b), it is clear that the absorption edge approximately located at 2.6 eV is not significantly varying with outer diameter and length of these nanotubes. Figure 6.2(c) & (d) shows a significant shift of PL peak position over a wide range of ~0.4 from the absorption edge of CdS nanotubes having different diameter and lengths.

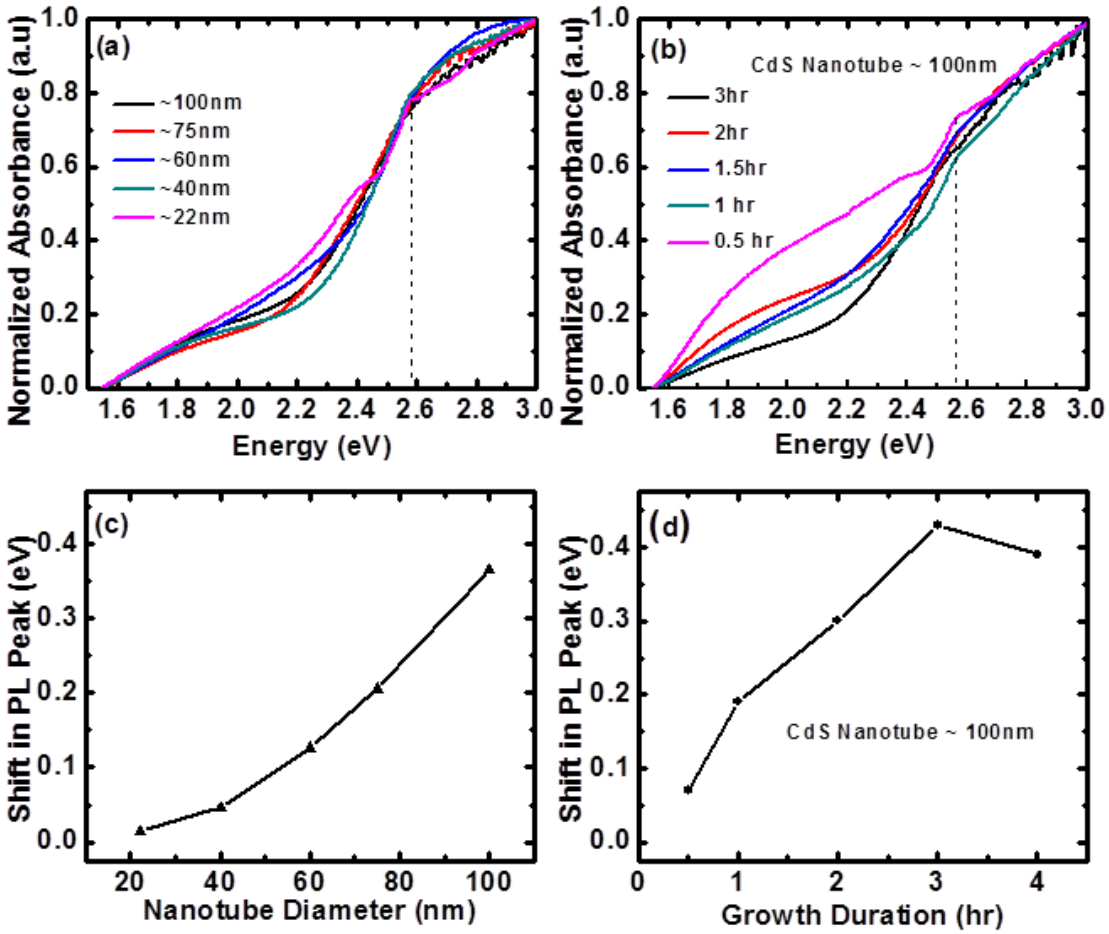

Figure 6.2: (a) Absorbance spectra of CdS nanotubes with different diameter (b) and growth durations. Calculated values of these red shifts of PL peak position from the absorbance edge of CdS nanotubes with increasing diameters and length (growth durations) are plotted in (c) and (d) respectively.

It is common to except a blue shift in absorbance and PL spectra for smaller nanostructures with size comparable to Bohr exciton radius of CdS [3nm]. However, as compared to absorbance spectra, photoluminescence is always influenced by surface conditions and defects. While absorbance directly relates to the joint density of state of a quantum confined structure, luminescence requires radiative recombination of excited electron and holes, which is strongly influenced by the presence of surface defects. To further probe the PL shift, we will identify the presence of strain and defects in these CdS nanotubes.

6.4 Elemental compositional analysis

As described in section 2.4.8, one way to identify the elemental composition is Energy dispersive X-ray Spectroscopy [EDS]. Figure 6.3(a) shows the EDS of CdS nanotubes having different diameters grown on porous alumina and most of the scanned area of samples shows excess of cadmium. It is also visible from the error bar (S/Cd >1), some areas of smaller diameter nanotubes show little excess of sulfur atom. However the average S/Cd ratio lies between 0.9 and 1 for all nanotubes. It is also possible that high energy electron can not only penetrate whole of the CdS nanotubes but also penetrate inside the porous alumina. As a result, EDS may also detect the free Cd ions attached to porous alumina during the growth process of CdS nanotubes. So it is difficult to quantitatively identify the atomic composition on the surface of these CdS nanotubes.

We have also removed nanotubes attached to the porous alumina using sonication bath and drop casted on silicon wafer. Figure 6.3(b) shows the EDS of individual CdS nanotubes having different diameter. Similarly here also, we observed a slight excess of Cd on the nanotubes. Using FESEM and EDS attachment [section 2.4.8] for samples grown at lesser duration, it is difficult to identify the exact ratio of chemical composition mainly due to less quantity of material. Removing such small nanotubes using sonication method is a difficult task. Moreover these small CdS nanotubes grown for lesser duration have the tendency of excess cadmium within its bulk but as the growth proceeds in Na_2S environment, there is a probability of excess sulfur on these nanotubes also. X-Ray photoelectron spectroscopy of these CdS nanotubes was also performed but the results were inconclusive.

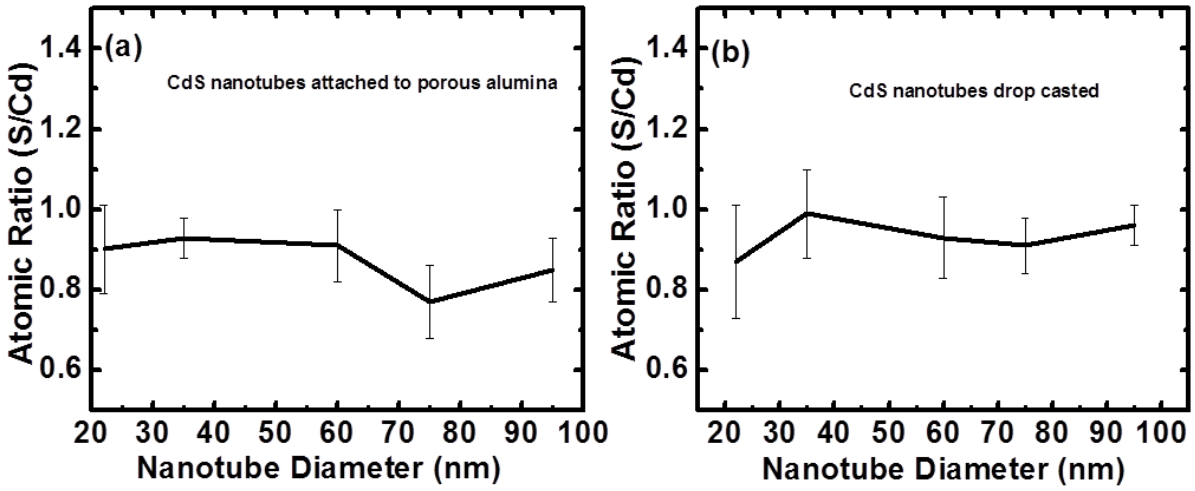

Figure 6.3: (a) Chemical composition of CdS nanotubes grown on different diameter of porous alumina and shows an excess of cadmium on CdS nanotubes. (b) CdS nanotubes drop casted on silicon wafer for chemical compositional study and also show excess of Cd ions.

6.5 Structural characterization

6.5.1 X-ray diffraction

Figure 6.4(a) show the X-ray diffraction [XRD] spectra of CdS nanotubes having different outer diameters and (b) having different lengths respectively. Smallest diameter [22 nm] nanotubes are better resolved due to overlapping peaks than those with larger diameters. In the next section we will show that the main reason for the above is due to the larger crystallite size as compared to bigger ones. The most prominent XRD peak centered on 2θ value of 26.7º can be indexed[140,141] either to 002 plane of hexagonally packed wurtzite phase of CdS [JCPDS 75-1545] or to the 111 plane of CdS cubic phase [zinc blende] [JCPDS 10-0454]. Both form a stable phase at room temperature and also the difference in formation energies[69-71] between them is very small. That makes it difficult to identify exact crystalline phase of CdS. It became more complicated for wurtzite phase, which have additional peaks from 100 and 101 planes [figure 6.4] that appear on both side of 002 peak positions, whereas cubic phase has only one peak at that range. In figure 6.4(a), we can identify these overlapping additional peaks from the shoulder like feature visible for smaller diameter CdS nanotubes. These shoulders correspond to the peaks

neighboring to the dominant 002 peak of wurtzite phase of CdS nanotubes. This shows that the preferred growth direction of CdS nanotubes along 002 planes is possibly due to wurtzite phase.

In presence of such overlapping peaks and broadening due to strain around 26.7º, Debye-Scheerer [section 2.7.3] may not be a good method to determine crystalline size. Usually, Williamson-Hall method as discussed [in section 2.7.4] is used to separate the individual contribution of both strain and crystallite size on the broadening of XRD peak. In this case also, it requires a well-formed and non-overlapping XRD peaks to differentiate strain from size related broadening. However, to understand the role of crystallite size and strain in PL shift, we estimated these in a systematic way using Debye-Sheerer and micro strain equations [section 2.7].

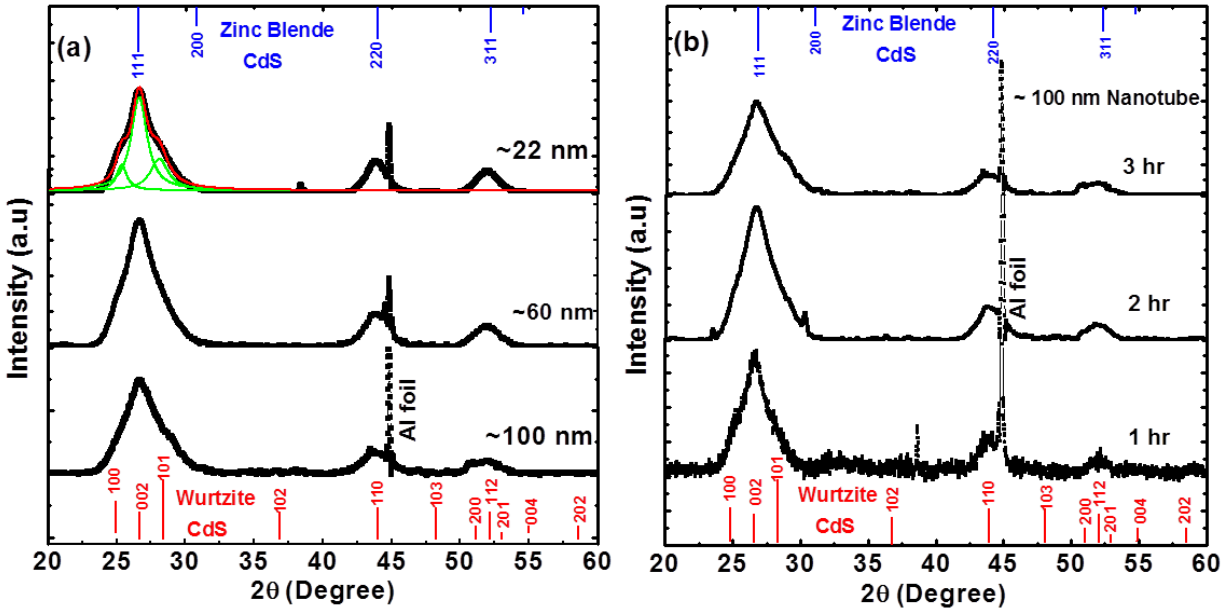

Figure 6.4: (a) X-ray diffraction spectrum of CdS nanotubes having different diameters & (b) different growth durations (or lengths) with outer diameter of about 100 nm. X-ray intensity around 2θ = 45º is due to Aluminum (Al) attached to porous alumina. As seen for 22 nm diameter nanotubes, in (a) we had de-convoluted the broadened XRD peak for all sizes to calculate the crystalline strain and crystallite size for 002 planes.

6.5.2 Crystalline size

In this work, we used Lorentzian function to de-convolute the dominant XRD peak as seen in figure 6.4(a) around $2\theta=26.7^{o}$ into three individual peaks and calculated the integral breadth $\beta = (\pi/2)$ FWHM, of the prominent 002 peak for further use. Using Debye-Scherer formula [equation 2.8] $D = K\lambda/\beta\cos\theta$ with $K=0.9$ and $\lambda = 0.154$ nm, we can estimate the crystalline size [D] of all these CdS nanotubes. From figure 6.5(a) and (b), it is clearly visible that crystallite sizes actually decreases with increasing outer diameter and length of these nanotubes respectively. If this is the case, we should observe a blue shift in PL for increasing diameter and length of these nanotubes by quantum confinement effect but our PL spectra show opposite behavior. We did similar calculation as shown in figure [6.5 c, d, e & f] at 2θ for 44^{o} and 52^{o} and observed the same result as above. We further conclude that quantum confinement effect due to crystalline size is not playing a major role in PL shift as the expected PL shifts due to size effects could have been in the other direction. We certainly observe redshift of PL (figure 6.1) with increasing crystallite sizes as compared to the blue shift usually expected from such quantum confinement effects.

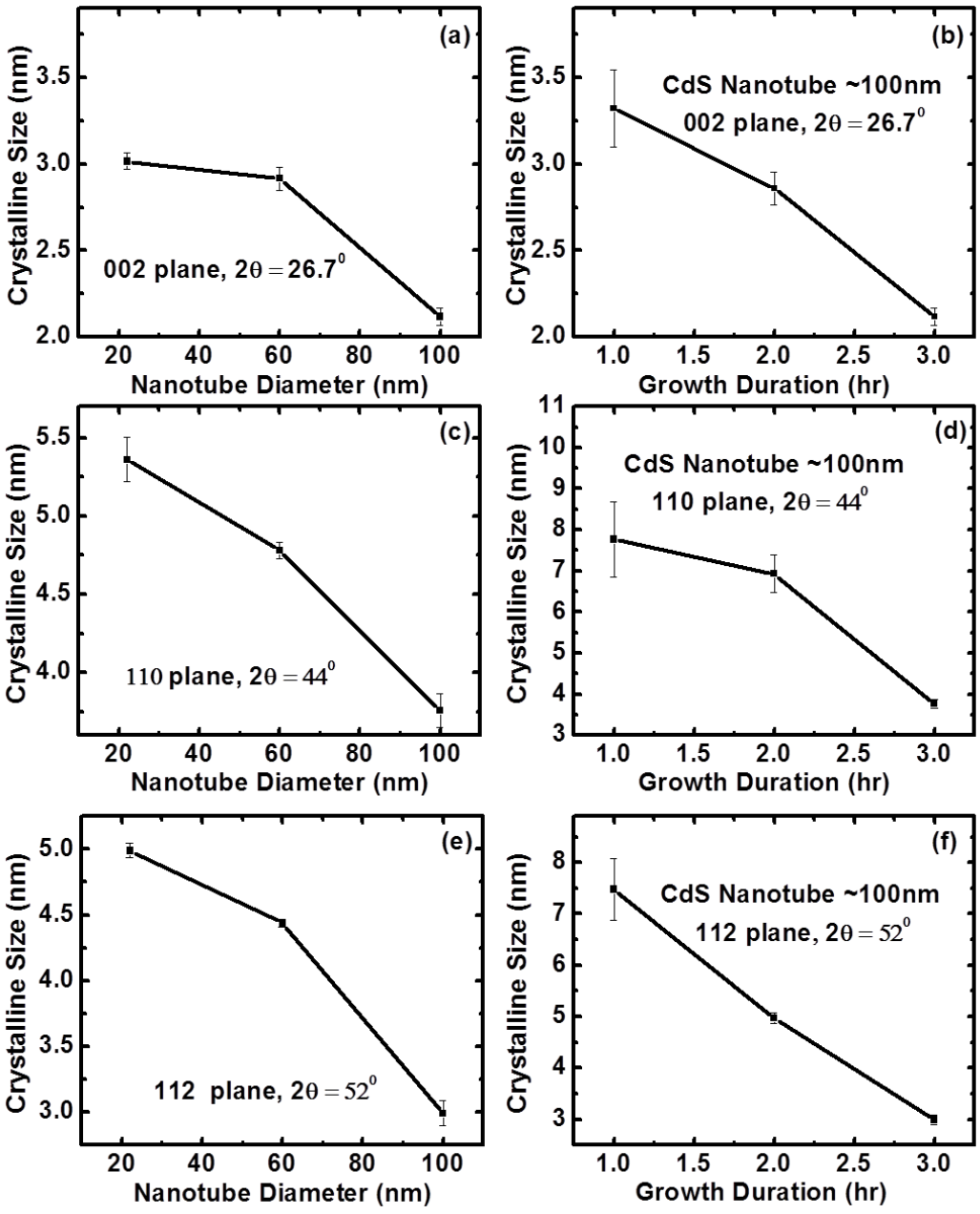

Figure 6.5 (a) and (b) are the estimated crystallite sizes of CdS nanotubes having different diameter and growth duration at 2θ=26.7º for 002 plane. Clearly it is visible that the crystallite size estimated by Debye-Sheerer method is decreasing with increasing diameter and length. Similarly, (c) and (e) are the calculated crystallite sizes of CdS nanotubes with increasing diameter at different 2θ value and shows decreasing crystallite size. Same behavior is observed in (d) & (f) for increasing length of these nanotubes.

6.5.3 Role of strain

We roughly estimate the weighted average strain [ε] in CdS nanotubes using $\varepsilon = \beta/4\tan\theta$ [equation 2.9]. Systematic deviations of these calculated micro strains are plotted in figure 6.6 with respect to nanotube diameter and growth duration [length] respectively. Observed behavior clearly predict crystalline strain gradually increases with increasing nanotube diameter and also with nanotube length. Similar estimates based on other less intensity XRD peaks also support the above systematic change in crystalline strain with increasing size of these nanotubes. Therefore, it is easy to accept that these CdS nanotubes with bigger overall dimensions [length and diameter] have more inbuilt structural strain. This assertion highlights the role of strain as well as defects in the observed PL shift of CdS nanotubes grown at different durations and also having different diameters.

We already presented in chapter 3 that the nanotubes nucleation occurs at nanotube-AAO interface. At this stage, we assume that such size dependent crystalline strain can originate during the subsequent growth nucleation from the existing bulk of the CdS nanotube already formed. Structural bending of the nanotubes under their own weight may cause these strain which certainly increases with increasing size (e.g. increasing diameter and length). Subsequently, this can result in systematic changes in the energy level of a particular defect. Finally, the combined effect of defect and strain can lead towards shifting and broadening of PL spectra if such defects are significantly affected by strain. To support our understanding, we present results from electronic structure calculations to explain the PL shift of these nanotubes.

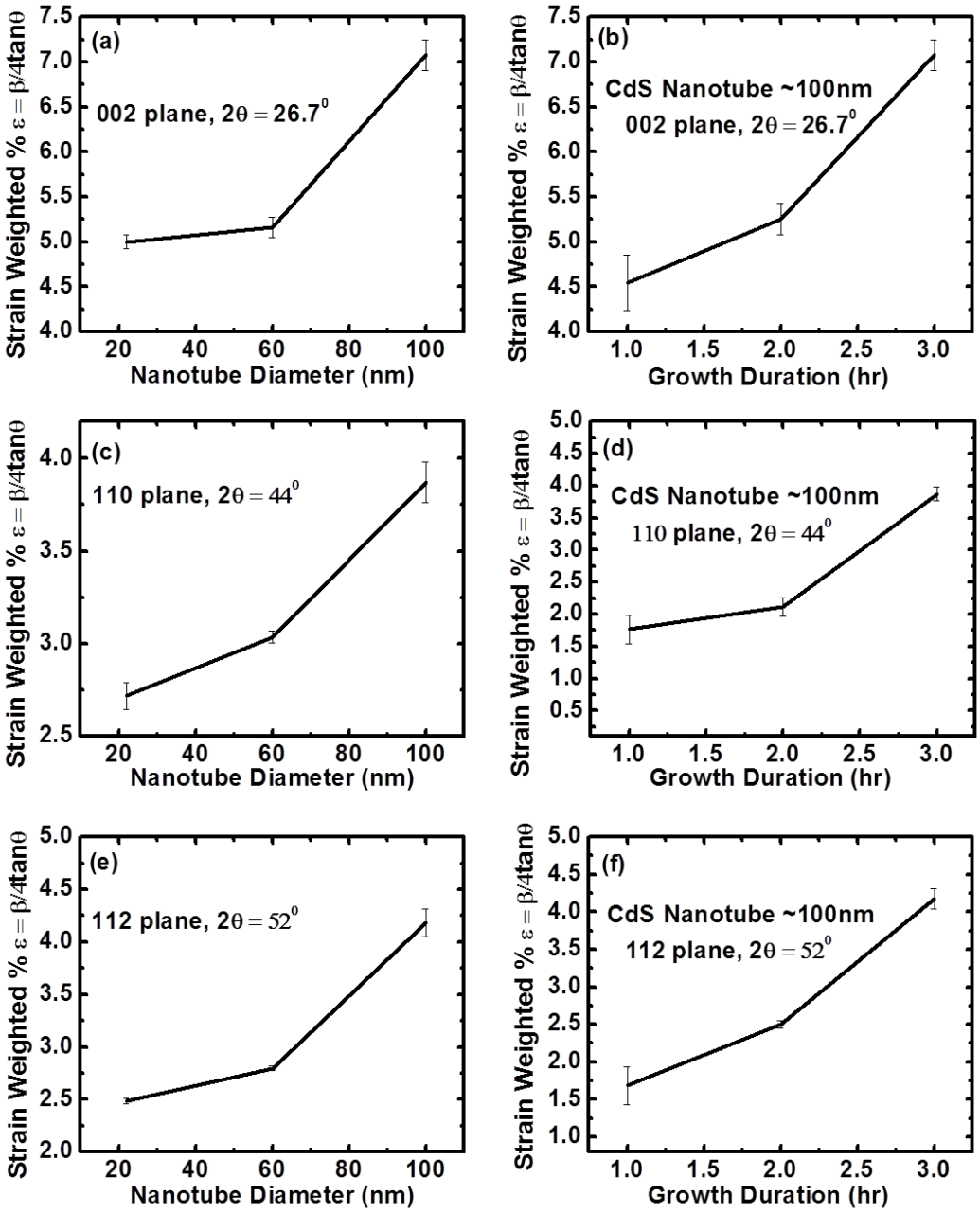

Figure 6.6 (a) and (b) are the estimated average crystalline strain of CdS nanotubes having different diameter and growth duration at 2θ=26.7º for 002 plane. Clearly it is visible that the crystalline strain estimated is increasing with diameter and growth duration. Similarly, (c) and (e) are the calculated crystalline strain of CdS nanotubes with increasing diameter at different 2θ value and also shows increasing crystalline strain. Same behavior is observed in (d) & (f) for increasing length of these nanotubes.

6.6 Role of strain and defects in PL process

Our collaborator, Dr. Prasenjit Ghosh[137] had done some theoretical modeling based on the observed PL shift from these ligand free CdS nanotubes. All such electronic structure calculations are based on density functional theory applied to a single shelled CdS nanotube [pristine nanotubes] containing six molecules. This helped us to verify the above hypothesis and to understand the role of strain and defects. We will show important points necessary to explain the observed PL shift. As these nanotubes are grown in sulfur rich environment, most favorable defects with least formation energy is sulfur interstitial [S^{nt}_{i}]. Figure 6.7 shows the defect formation energy for different possible defects for CdS nanotubes nucleated in a sulfur rich condition. Most abundant defect, sulfur interstitial is fully occupied and also optically inactive, whereas the second least probable cadmium vacancy [V^{nt}_{cd}] has two energy states [as shown in figure 6.7] is mostly participating in PL process. For a cadmium vacancy defect involved PL process, initially electrons are excited to conduction band (CB) and eventually they decay into Cd-mol-S state[137] just below CB. These electrons will recombine with holes due to partially or unfilled acceptor state arising from cadmium vacancy, which lies just above valence band (VB).

We also noted that, the strain incorporated during nucleation process is inhomogeneous and might be able to affect the position of CB, VB and defects. To understand the effect of strain, calculations are done on varying the c from -4% to 5% along the c axis of pristine nanotube[137]. For defect free nanotubes, compression and expansion is not affecting the position of VB and CB. Most importantly in this particular case, the minority defects originated due to cadmium vacancy involved in PL process shows a significant shift in its position with increasing tensile strain. Cadmium vacancy on the surface of CdS nanotubes experiences more tensile strain with increasing length and diameter and thereby the red shift in PL. Overall these calculations predict a red shift of 0.33 eV, which is well within the observed experimental data [about 0.4 eV]. We can attribute the observed red shift in PL spectra from CdS nanotubes with increasing length and diameter due to an interplay between the inbuilt strain and cadmium vacancy incorporated during growth process.

System	Defect	Defect formation energy(eV)
Bulk	V^{b}_{Cd}	2.26
	V^{b}_{S}	3.34
Nano-tubes	V^{nt}_{Cd}	0.90
	V^{nt}_{s}	2.19
	Cd^{nt}_{i}	1.79
(a)	S^{nt}_{i}	0.24

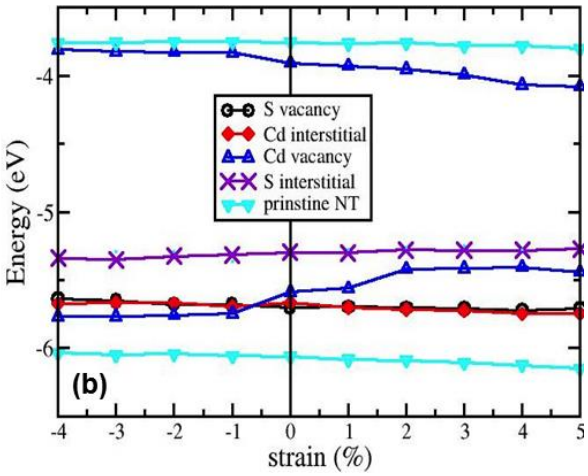

Figure 6.7: DFT result calculated by Dr. Prasenjit Ghosh[137]. (a) Tabular column show the defect formation energy in a sulfur rich environment. (b) Right hand side figure show the position of energy levels of CB, VB and various defects in strain. There is a considerable shift for Cd vacancy with strain and its means that the defect with second least probable formation energy plays an important role in PL shift. Although sulfur interstitial defect is the most abundant due to its lowest formation energy, but it hardly changes at all with increasing strain.

6.7 Summary

In summary, we had shown the photoluminescence spectra of ligand free CdS nanotubes red shifts as the length or diameter of the nanotubes increase. Significant shift in the absorption spectra is not observed because the excitation of electrons involving the valence and conduction bands is not affected by strain and quantum confinement effects. Our experimental calculation using x-ray diffraction pattern shows an increasing crystalline strain with the size of CdS nanotubes. Increasing weight of the already grown CdS nanotube possibly causing this enhanced strain at its nucleation site near the AAO template during its growth. From DFT modeling, this PL shift is identified as an effect due to interplay between the strain developed with increasing size and Cd vacancies incorporated on the surface of these CdS nanotubes during the synthesis. One of the most important observations from theoretical calculations on CdS nanotubes, is the participation of second least possible Cd vacancy minority defect in PL process, whereas other

more abundant defects like sulfur interstitials are not involved. These Cd vacancy defects although not most abundant in these nanotubes but these are mostly affected by strain and thereby a shift in PL. It is usually believed that a densely populated defect can play crucial roles in determining the optical properties of these nanotubes. Interestingly, our experimental observations and further understanding through theoretical modeling suggests that instead of the defect concentration, it is the nature of the defect which is more important for understanding the optical properties.

Chapter 7

Conclusion and Future Plans

7.1 Conclusion

Role of chemical reaction dynamics in wet chemical nanofabrication is well known and also reported extensively in the literature. Depending on the fabrication route, nanoscale growth mechanisms of reacting chemicals at interfaces can be influenced by fluid dynamics, but this is quite challenging, and also not studied well in great detail. In this work, we used a simple nanofabrication technique particularly to probe these mutually overlapping roles of hydrodynamics and chemistry in the formation of nanostructures. In this thesis, we have self-assembled arrays of 'ligand free' CdS nanotubes using two chamber fabrication route. We analyzed various physical parameters which can influence the increasing runaway growth rate with time and our results cannot be explained by simple diffusion based models alone. Our overall observations clearly indicate the need of chemo-hydrodynamically triggered instability at nanoscale for such growth process and one should need a proper understanding to further probe the growth mechanism. These ligand free CdS nanotubes, although demonstrate good optical quality in terms of substantial light emission, are also prone to having surface defects and strain which actually dictates the red shift of photoluminescence peak with increasing size. Density functional calculations also supported our hypothesis of how such in-built electronic defects can actually control the red shifts of photoluminescence peaks with increasing nanotube size. Both experimental and theoretical investigations, clearly indicated the role of cadmium vacancy 'minority' defects, although not most abundant, are affected by the inbuilt strain incorporated during the nanofabrication process itself. Therefore, this last result in some way completes the full circle of our explorations which started with a small observation of asymmetric growth of CdS nanotube on nanoporous alumina template.

Technically speaking, in the beginning, we presented structural evidences based on FESEM imaging to understand the presence of hydrodynamics in nucleation process of CdS nanotubes using nanochannels of porous alumina as a intermediary nanoreactor between two chemical precusors. Nano confined chemical reactions between two reactive fluid precursors further leads to directionally asymmetric growth of CdS nanotubes on porous alumina facing the Na_2S precursor. We had shown this using ex-situ scanning electron microscopy imaging at different stages of the growth process. This asymmetric growth was mainly due to dissimilar horizontal flow of these reactive precursor ions [Cd^{++} and S^{--}] flowing in from opposite directions through these nanochannels. It was evident that cadmium ions need to flow through these porous alumina nanochannels and then mix and react with sulfur ions on the Na_2S side of the alumina nanochannels to form these ligand free CdS nanotubes. Dissimilar flow rates of both $CdCl_2$ and Na_2S through these nanochannels were estimated using Fick's law and optical absorption studies. Based on these evidences, we also argued that coupling between chemical reaction and hydrodynamics are necessary to sustain such prolonged nucleation at CdS-Na_2S interface. We also presented a crucial observation from scanning electron microscopy, which clearly identified the location of nanotubular nucleation sites at CdS-AAO interface. We further indicated that chemo-hydrodynamic instability at the liquid-liquid reactive interface as a plausible triggering force for such sustained horizontal growth of CdS nanotubes. However, our preliminary understanding of such hydrodynamic origin was not in not in sync with standard concepts of classical fluid dynamics which cannot predict such an instability occurring at these small length scales. Therefore, we maintained that further experimental and theoretical investigations were necessary to get a better picture.

Following our work, few theoretical papers were published which tried to explain this growth process based on solely by the diffusion of precursor ions. However, our experimental results show a runaway increase in the growth rate of CdS nanotubes with growth duration and also with reducing pore size of porous alumina. Moreover, it is surprising that variation of Cd^{++} concentration during the experiment does not affect the growth at all. This is against the diffusion based understandings of the growth process which necessarily require such Cd^{++} jets to fuel the growth elongation. Therefore, these results on self-assembly of CdS nanotubes require

more detailed investigations to substantiate the precise role of fluid dynamics responsible for such extended nanotubular growth at AAO-Na_2S interface. Further experiments done by varying the concentration of precursor ions clearly indicated the dominant role of Na_2S solution in such nanoscale growth. Addition of capping agents during such two-chamber nanoreactor growth also maintained similar nanotubular formations. All these preliminary results without a doubt demonstrate that hydrodynamical effects together with chemical reaction dynamics at the interface can be playing an important role in nanofabrication process and one certainly requires further study to quantify it.

Moreover, we also reported an enhanced photoluminescence from CdS nanotubes as compared with CdS nanocrystallites made by bulk mixing of the same chemical precursors. Even though both have similar crystallite sizes, possible presence of nonradiative traps in the CdS nanocrystallites may be responsible for its reduced light emission. Reason for such enhanced photoluminescence in ligand free CdS nanotubes was argued on the basis of directional nature of light emission and radiative recombination through defects. In fact superior photoluminescence of such nicely ordered arrays of CdS nanotubes is a testimony to its good optical property.

Finally we had established the effect of inbuilt crystallite strain on surface electronic defects, which can significantly shift the energy. This leads to observed red shifts in photoluminescence peaks from CdS nanotubes having increasing lengths or diameters. Estimation of micro strain using powder x-ray diffraction pattern of CdS nanotubes, show a systematic increase with increasing diameters and lengths and was sufficient to understand its overall influence. Also during growth nucleation, CdS nanotubes having bigger diameters or larger lengths are prone to more inbuilt strain as compared to the smaller one, which finally leads to red shift in photoluminescence peak. Density functional calculations also supported this explanation that cadmium vacancy defects with second least formation energy (i.e. it is not the most abundant defect in these nanotubes) are mostly involved in this red shift of PL at varying degree of strain. Most importantly, we could establish that the nature of these surface electronic defects is more crucial in optical emission process from these CdS nanotubes as compared to the overall concentration of such defects.

In conclusion, we had developed an interesting nanofabrication process to understand the role of chemo-hydrodynamically triggered nanoscale self-assembly. We also studied the

influence of strain and surface defects on optical emission process of CdS nanotubes having sizable light emission. These preliminary studies have certainly provided enough impetus to many unanswered questions about the whole gamut of nanofabrication mechanisms and invoked strong interests and research papers from various communities dealing with nanoscience, statistical physics and soft matter etc. However, further experiments and precise quantitative estimates are necessary to gain a complete understanding.

7.2 Future plans

This particular nanofabrication route can now be explored further for growing a wide variety of materials and nanostructures for potential device applications. Similarly this can be an efficient way to study growth mechanism of such self-assembled nanostructures within a nanoconfined place and also to investigate nanoscale fluid dynamics. Further investigations and extension of classical fluid dynamics to understand nanofabrication is necessary to gain better quantitative knowledge about the growth mechanism of such complicated nanostructure. Influence of external forces like pressure, temperature, applied voltage/current and surfactants etc on the nanoscale growth process will also help us to understand the role of interfacial forces in such nanofabrication routes. We certainly hope that someday hydrodynamical effects will be used to precisely tune nanostructures and nanodevices having novel electronic and optical properties.

Furthermore, electronic properties of single CdS nanotube are currently being investigated with the help of micro/nano lithographically fabricated electrical contacts. This will help us to probe the electronic charge transport through a single nanotube and also the role of any anisotropic light emission as well as excitonic lasing if there is any. Moreover, one can certainly try to extend the above two chamber nanoreactor based self-assembly of CdS nanotubes to grow CdS/PbS, CdS/Ag etc heterostructure nanowires for their use in nano photovoltaic cells and also in hybrid dielectric-nanoplasmonic devices respectively.

References

[1] Richard P. Feynman, "*There's Plenty of Room at the bottom*", http://www.zyvex.com/nanotech/feynman.html.

[2] H. E. Schaefer, *Nanoscience: The Science of the Small in Physics, Engineering, Chemistry, Biology and Medicine.* Berlin: Springer-Verlag, 2010.

[3] Bharat Bhushan, *Springer Handbook of Nanotechnology*. New York: Spinger-Verlag, 2004.

[4] C. P. Poole and F. J. Owens, *Introduction to Nanoscience and Nanotechnology*. New Jersey: Wiley Interscience, 2003.

[5]*Characterization of Nanophase Materials*, Edited by W. Z. Lin. Weinheim: Wiley-VCH, 2000.

[6]Mostafa A El-sayed, *"Small Is Different: Shape, Composition-Dependent Properties of Some Colloidal Semiconductor Nanocrystals"*, vol. 37, pp. 326–333, 2004.

[7] Emil Roduner, *"Size matters: why nanomaterials are different"*, Chemical Society reviews, vol. 35, pp. 583–592, 2006.

[8]J. H. Davis, *The Physics of Low-Dimensional Semiconductors An introduction*. Cambridge University Press, 1998.

[9] L.S. Li, J. Hu, W. Yang and A. P. Alivisatos, *"Band Gap Variation of Size and Shape Controlled Colloidal CdSe Quantum Rods"*, Nano Lett., vol. 1, no. 7, pp. 349–351, 2001.

[10]Y. Xia, P. Yang, Y. Sun, Y. Wu, B. Mayers, B. Gates, Y. Yin, F. Kim and H. Yan, *"One-Dimensional Nanostructures : Synthesis , Characterization , and Applications"*, Adv. Mater., vol. 15, pp. 353–389, 2003.

[11]E. C. Garnett, M. L. Brongersma, Y. Cui, and M. D. McGehee, *"Nanowire Solar Cells"*, Annu. Rev. Mater. Res., vol. 41, pp. 269–295, 2011.

[12]Y. Guo, Y. Zhang, H. Liu, S.W. Lai, Y. Li, Y. Li, W. Hu, S. Wang, C.M. Che and D. Zhu, *"Assembled Organic/Inorganic p-n Junction Interface and Photovoltaic Cell on a Single Nanowire"*, J. Phys. Chem. Lett., vol. 1, pp. 327–330, 2010.

[13]J. Tang, Z. Huo, S. Brittman, H. Gao and P. Yang, *"Solution-processed core-shell nanowires for efficient photovoltaic cells"*, Nature Nano., vol. 6, pp. 568–572, 2011.

[14]A. L. Mohana Reddy, M. M. Shaijumon, S. R. Gowda and P. M. Ajayan, *"Coaxial MnO/carbon nanotube array electrodes for high-performance lithium batteries"*, Nano Lett., vol. 9, pp. 1002–6, 2009.

[15]M. Salari, K. Konstantinov and H. K. Liu, *"Enhancement of the capacitance in TiO2 nanotubes through controlled introduction of oxygen vacancies"*, J. Mater. Chem., vol. 21, pp. 5128, 2011.

[16]R. Liu, J. Duay and S. B. Lee, *"Heterogeneous nanostructured electrode materials for electrochemical energy storage"*, Chem. Commu., vol. 47, pp. 1384–1404, 2011.

[17]X. Lang, A. Hirata, T. Fujita and M. Chen, *"Nanoporous metal/oxide hybrid electrodes for electrochemical supercapacitors*", Nature Nanotech., vol. 6, pp. 232–236, 2011.

[18] C. Liu, F. Li, L. P. Ma and H. M. Cheng, *"Advanced Materials for Energy Storage"*, Adv. Mater., vol. 22, pp. E28-E62, 2010.

[19]R. Yan, D. Gargas and P. Yang, *"Nanowire photonics"*, Nature Photonics, vol. 3, pp. 569–576, 2009.

[20]H. Masuda and K. Nishio, *"Self-Organized Nanoscale Materials: Synthesis and Applications of Highly Ordered Anodic Porous Alumina"*, edited by M. Adachi and D. J. Lockwood, NewYork: Springer, 2006.

[21]V. Sadasivan, C. P. Richter, L. Menon and P. F. Williams, *"Electrochemical Self-Assembly of Porous Alumina Templates"*, AICHE Journal, vol. 51, pp. 649–655, 2005.

[22] G. D. Sulka, "*Nanostructured Materials in Electrochemistry: Highly Ordered Anodic Porous Alumina Formation"*, Edited by AliEftekhari. Wiley-VCH Verlag, 2008.

[23] O. Jessensky, F. Muller and U. Gosele, *"Self-organized formation of hexagonal pore arrays in anodic alumina"*, Appl. Phys. Lett., vol. 72, pp. 1173–1175, 1998.

[24]K. Nielsch, J. Choi, K. Schwirn, R. B. Wehrspohn and U. Gosele, *"Self-ordering Regimes of Porous Alumina: The 10 % Porosity Rule"*, Nano. Lett., Vol. 2, pp. 677-680, 2002.

[25]A. Birner, K. Nielsch and U. Go, *"Hexagonal pore arrays with a 50- 420 nm interpore distance formed by self-organization in anodic alumina",* J. Appl. Phys., vol. 84, pp. 6023–6026, 1998.

[26]C. Girginov and S. Kozhukharov, *"Surface of Alumina Films after Prolonged Breakdowns in Galvanostatic Anodization"*, International Journal of Electrochemistry, vol. 126726, pp. 1–5, 2011.

[27]S. Ono, M. Saito, M. Ishiguro and H. Asoh, *"Controlling Factor of Self-Ordering of Anodic Porous Alumina"*, Journal of the Electrochemical Society, vol. 151, pp. B473, 2004.

[28]N. Klein and V. Moskovici, *"Electrical Breakdown II During the Growth of Aluminum Oxide"*, J. Electrochem. Soc., vol. 127, pp. 152, 1980.

[29] R. S. Alwitt, *Anodizing*. Electrochemistry Encyclopedia, Boundary Technologies, Inc. < http://knowledge.electrochem.org/encycl/art-a02-anodizing.htm >.

[30]A. Yamaguchi, H. Kaneda, W. Fu and N. Teramae, *"Structural Control of Surfactant-Templated Mesoporous Silica Formed Inside Columnar Alumina Pores"*, Adv. Mater., vol. 20, pp. 1034–1037, 2008.

[31]B. J. Kirby, *Micro- and Nanoscale Fluid Mechanics Transport in microfluidic devices.* Cambridge University Press, 2010.

[32]P. Abgrall and N. T. Nguyen, *Nanofluidics*. Boston: Artech House, 2009.

[33] G. A. Parks, *"The Isoelectric Points of Solid Oxides, Solid Hydroxides, and Aqueous Hydroxo Complex system"*, Chem. Rev., vol. 65, pp. 177-198, 1965.

[34] R. Yan, W. Liang, R. Fan and P. Yang, *"Nanofluidic Diodes Based on Nanotube Heterojunctions"*, Nano. Lett., Vol. 9, pp. 3820-3825, 2009.

[35]H. Daiguji, *"Ion transport in nanofluidic channels"*, *Chem. Soc. Rev*, vol. 39, pp. 901, 2010.

[36]R. B. Schoch , J. Han and P. Renaud, *"Transport phenomena in nanofluidics"*, Rev. Mod. Phys., vol. 80, no. 3, pp. 839, 2008.

[37]A. Piruska, M. Gong, J. V. Sweedler and P. W. Bohn, *"Nanofluidics in chemical analysis"*, Chem. Soc. Rev., vol. 39, pp. 1060, 2010.

[38]D. Kim, A. Raj, L. Zhu, R. I. Masel and M. A. Shannon, *"Non-equilibrium electrokinetic micro / nano fluidic mixer"*, Lab Chip, vol. 8, pp. 625–628, 2008.

[39]F. Charru, *Hydrodynamic Instabilities*. Cambridge University Press, 2011.

[40]K. Eckert, M. Acker and Y. Shi, *"Chemical pattern formation driven by a neutralization reaction .I . Mechanism and basic features"*, Phys. Fluids., vol. 16, pp. 385, 2004.

[41]N. N. Smirnov, V. F. Nikitin, A. Maximenko, M. Thiercelin and J. C. Legros *"Instability and mixing flux in frontal displacement of viscous fluids"*, Phys. Fluids, vol. 17, pp. 084102, 2005.

[42]T. Bánsági, D. Horváth and A. Tóth, *"Nonlinear interactions in the density fingering of an acidity front"*, J. Chem. Phys., vol. 121, pp. 11912, 2004.

[43]J. T. Chen, M. Zhang and T. P. Russell, *"Instabilities in Nanoporous Media"*, Nano. Lett., vol. 7, pp. 183, 2007.

[44]S. J. Kim, Y. C. Wang, J. H. Lee, H. Jang and J. Han, *"Concentration Polarization and Nonlinear Electrokinetic Flow near a Nanofluidic Channel"*, Phys. Rev. Lett., vol. 99, pp. 044501, 2007.

[45]H. C. Chang and G. Yossifon, *"Understanding electrokinetics at the nanoscale: A perspective"*, Biomicrofluidics, vol. 3, pp. 012001, 2009.

[46] C. Stowell and B. A. Korgel, *"Self-Assembled Honeycomb Networks of Gold Nanocrystals"*, Nano. Lett., Vol. 1, pp. 595, 2001.

[47] E. Tan and S. T. Thoroddsen, *"Marangoni instability of two liquids mixing at a free surface"*, Phys. Fluids, vol. 10, pp. 3038, 1998.

[48] M. Dietzel and S. M. Troian, *"Mechanism for spontaneous growth of nanopillar arrays in ultrathin films subject to a thermal gradient"*, J. Appl. Phys., vol. 108, pp. 074308, 2010.

[49] M. Maillard, L. Motte, A. T. Ngo and M. P. Pileni, *"Rings and Hexagons Made of Nanocrystals : A Marangoni Effect"*, J. Phys. Chem. B., vol. 104, pp. 11871–11877, 2000.

[50] A. Vidal and A. Acrivos, *"Effect of Nonlinear Temperature Profiles On the Onset of Convection Driven by Surface Tension Gradients"*, I& EC Fundamentals , vol. 7, pp. 53–58, 1968.

[51]J. Zhang, A. Oron and R. P. Behringer, *"Novel pattern forming states for Marangoni convection in volatile binary liquids"*, Phys. Fluids, vol. 23, pp. 072102, 2011.

[52] D. A. Bratsun and A. D. Wit, *"On Marangoni convective patterns driven by an exothermic chemical reaction in two-layer systems"*, Phys. Fluids., vol. 16, pp. 1082, 2004.

[53] L. Rongy and A. D. Wit, *"Steady Marangoni flow traveling with chemical fronts"*, J. Chem. Phys., vol. 124, pp. 164705, 2006.

[54] C. Almarcha, Y. R. Honi, Y. D. Decker, P. M. J. Trevelyan, K. Eckert and A. D. Wit, *"Convective Mixing Induced by Acid - Base Reactions"*, J. Phys. Chem. B., vol. 115, pp. 9739–9744, 2011.

[55] R. L. Aguilar, I. Pagonabarraga and A.H. Machado, *"Three-dimensional aspects of fluid flows in channels II Effects of meniscus and thin film regimes on viscous fingers"*, Phys. Fluids., vol. 19, pp. 102113, 2007.

[56]D.A .Weitz, J. P. Stokes, R. C. Ball and A. P. Kushnick, *"Dynamic Capillary Pressure in Porous Media: Origin of the Viscous-Fingering Length Scale"*, Phys. Rev. Lett., vol. 59, pp. 2967–2970, 1987.

[57]M. Mishra, M. Martin and A. D. Wit, *"Miscible viscous fingering with linear adsorption on the porous matrix"*, Phys. Fluids, vol. 19, pp. 073101, 2007.

[58] H. C. Chang, G. Yossifon and E. A. Demekhin, *"Nanoscale Electrokinetics and Microvortices : How Microhydrodynamics Affects Nanofluidic Ion Flux"*, Annu. Rev. Fluid Mech., vol. 44, pp. 401, 2012.

[59]S. Kim, S. H. Ko, R. Kwak, J. D. Posner, K. H. Kang and J. Han, *"Multi-vortical flow inducing electrokinetic instability in ion concentration"*, Nanoscale, vol. 4, pp. 7406–7410, 2012.

[60] M. Mao, S. Ghosal and G. Hu, *"Hydrodynamic flow in the vicinity of a nanopore induced by an applied voltage"*, Nanotechnology, vol. 24, pp. 245202, 2013.

[61] G. Yossifon, P. Mushenheim, Y. C. Chang and H. C. Chang, *"Nonlinear current-voltage characteristics of nanochannels"*, Phys. Rev. E, vol. 79, pp. 046305, 2009.

[62] Charles Kittel, *Introduction to solid state physics*. Delhi: John Wiley & Sons, 1996.

[63]P. Y. Yu and M. Cardona, *Fundamentals of Semiconductors*. Berlin: Springer-Verlag, 2010.

[64]Sadao Adachi, *Properties of Group-IV, III-V and II-VI Semiconductors*. John Wiley & Sons Ltd, 2005.

[65]J. D. Levine and P. Mark, *"Theory and Observation of Intrinsic Surface States on Ionic Crystals"*, Physical Review, vol. 144, pp. 751, 1966.

[66] Z. Fan et al., *"Three-dimensional nanopillar-array photovoltaics on low-cost and flexible substrates"*, Nature Mater., vol. 8, pp. 648–53, 2009.

[67] C. H. Cho, C. O. Aspetti, M. E. Turk, J. M. Kikkawa, S. W. Nam and R. Agarwal, *"Tailoring hot-exciton emission and lifetimes in semiconducting nanowires via whispering-gallery nanocavityplasmons"*, Nature Mater., vol. 10, pp. 669, 2011.

[68] Y. K. Liu, J. A. Zapien, C. Y. Geng, Y. Y. Shan, C. S. Lee, Y. Lifshitz and S. T. Lee, *"High-quality CdS nanoribbons with lasing cavity"*, Appl. Phys. Lett., vol. 85, pp. 3241, 2004.

[69] U. Soni, V. Arora and S. Sapra, *"Wurtzite or zinc blende? Surface decides the crystal structure of nanocrystals"*, CrystEngComm, vol. 15, pp. 5458, 2013.

[70] A. Ghosh, S. Paul and S. Raj, *"Structural phase transformation from wurtzite to zinc-blende in uncapped CdS nanoparticles"*, Solid State Communications, vol. 154, pp. 25–29, 2013.

[71] R. J. Bandaranayake, G. W. Wen, J. Y. Lin, H. X. Jiang and C. M. Sorensen, *"Structural phase behavior in II VI semiconductor nanoparticles"*, Appl. Phys. Lett., vol. 67, pp. 831, 1995.

[72] B. L. Cao, Y. Jiang, C. Wang, W. Wang, L. Wang, M. Niu, W. Zhang, Y. Li and S. T. Lee, *"Synthesis and Lasing Properties of Highly Ordered CdS Nanowire Arrays"*, Adv. Funct. Mater., vol. 17, pp. 1501–1506, 2007.

[73] X. Qian, H. Liu, Y. Guo, S. Zhu, Y. Song and Y. Li, *"Field Emission Properties and Fabrication of CdS Nanotube Arrays"*, Nanoscale Res. Lett., vol. 4, pp. 955–961, 2009.

[74] S. Kar and S. Chaudhuri, *"Shape Selective Growth of CdS One-Dimensional Nanostructures by a Thermal Evaporation Process"*, J. Phys. Chem. B. vol. 110, pp. 4542–4547, 2006.

[75] S. Gorer, J. A. Ganske, J. C. Hemminger and R. M. Penner, *"Size-Selective and Epitaxial Electrochemical / Chemical Synthesis of Sulfur-Passivated Cadmium Sulfide Nanocrystals on Graphite"*, J. Am. Chem. Soc., vol. 120, pp. 9584–9593, 1998.

[76] S. P. Huang, W. D. Cheng, D. S. Wu, J. M. Hu, J. Shen, Z. Xie, H. Zhang and Y. J. Gong, *"Density functional theoretical determinations of electronic and optical properties of nanowires and bulks for CdS and CdSe"*, Appl. Phys. Lett. vol. 90, pp. 031904, 2007.

[77]Xu et al., *"Dynamics of Bound Exciton Complexes in CdS Nanobelts"*, ACS Nano, vol. 5, pp. 3660–3669, 2011.

[78] S. Adachi, *Optical Constants of Crystalline and Amorphous Semiconductors Numerical Data and Graphical Information*. Newyork: Springer Science, 1999.

[79]T . D. Dzhafarov, M . Altunba¸ A. I. Kopya, V. Novruzov and E. Bacaksız, *"Formation of p-type CdS thin films by laser-stimulated copper diffusion"*, J. Phys. D: Appl. Phys., vol. 32, pp. L125–L128, 1999.

[80] F. Gemain, I. C. Robin, S. Renet and S. Bernardi, *"Photoluminescence studies of CdS layers for solar cells"*, Physica Status Solidi C, vol. 9, pp. 1740–1743, 2012.

[81] R. Memming, *Semiconductor Electrochemistry*. Weinheim: Wiley-VchVerlag GmbH, 2001.

[82] A. E. Abken, D. P. Halliday and K. Durose, *"Photoluminescence study of polycrystalline photovoltaic CdS thin film layers grown by close-spaced sublimation and chemical bath deposition"*, J. Appl. Phys., vol. 105, pp. 064515, 2009.

[83] C. Wang, K. M. Ip, S. K. Hark and Q. Li, *"Structure control of CdS nanobelts and their luminescence properties"*, J. Appl. Phys., vol. 97, pp. 054303, 2005.

[84] T. Zhai et al., *"Characterization, Cathodoluminescence, and Field-Emission Properties of Morphology-Tunable CdS Micro/Nanostructures"*, Adv. Funct. Mater., vol. 19, pp. 2423–2430, 2009.

[85] N. Chestnoy, T. D. Harris, R. Hull and L. E. Brus, *"Luminescence and Photophysics of CdS Semiconductor Clusters: The Nature of the Emitting Electronic State"*, J. Phys. Chem., vol. 90, pp. 3393–3399, 1986.

[86] G. Shen, J. H. Cho, J. K. Yoo, G. C. Yi and C. J. Lee, *"Synthesis of Single-Crystal CdS Microbelts Using a Modified Thermal Evaporation Method and Their Photoluminescence"*, J. Phys. Chem. B, vol. 109, pp. 9294–9298, 2005

[87]A. A. Vuylsteke and Y. T. Sihvonen, *"Sulfur Vacancy Mechanism in Pure CdS"*, Physical Review, vol. 113, 1959.

[88] B. Liu, G. Q. Xu, L. M. Gan, C. H. Chew and W. S. Li, *"Photoluminescence and structural characteristics of CdS nanoclusters synthesized by hydrothermal microemulsion"*, J. Appl. Phys., vol. 89, pp. 1059, 2001.

[89] J. J .Ramsdena and M. Gratzel, *"Photoluminescence of Small Cadmium Sulphide Particles*", J. Chem. Soc., Faraday Trans. 1, vol. 80, pp. 919–933, 1984.

[90] Q. Xiao and C. Xiao, *"Surface-defect-states photoluminescence in CdS nanocrystals prepared by one-step aqueous synthesis method"*, Applied Surface Science, vol. 255, pp. 7111–7114, 2009.

[91] P. Besomi and B. Wessels, *"Deep level defects in polycrystalline cadmium sulfide"*, J. Appl. Phys., vol. 51, pp. 4305, 1980.

[92] C. T. Tsai, D. S. Chuu, G. L. Chen and S. L. Yang, *"Studies of grain size effects in rf sputtered CdS thin films"*, J. Appl. Phys., vol. 79, pp. 9105, 1996.

[93] O. Vigil, I. Riech, M. G. Rocha and O. Z. Angel, *"Characterization of defect levels in chemically deposited CdS films in the cubic to hexagonal phase transition"*, J. Vac. Sci. Technol**.** A, vol. 15, pp. 2282–2286, 1997.

[94] H. Mathieu et al., *"Quantum confinement effects of CdS nanocrystals in a sodium borosilicate glass prepared by the sol gel process"*, J. Appl. Phys., vol. 77, pp. 287, 1995.

[95] G. T. Einevoll, *"Confinement of excitons in quantum dots"*, Phys. Rev. B, vol. 45, pp. 3410–3417, 1992.

[96] P. Thangadurai, S. Balaji and P. T. Manoharan, *"Surface modification of CdS quantum dots using thiols-structural and photophysicalstudies"*, Nanotechnology, vol. 19, pp. 435708, 2008.

[97] S. Vempati, Y. Ertas and T. Uyar, *"Sensitive Surface States and their Passivation Mechanism in CdS Quantum Dots"*, J. Phys. Chem. C, vol. 117, pp. 21609, 2013.

[98] C. N. R. Rao, A. Muller and A. K. Cheetham, *The Chemistry of Nanomaterials*. Weinheim: Wiley-VchVerlag GmbH, 2004.

[99] C. Klingshirn, *Semiconductor Optics*. Berlin: Springer-Verlag, 2005.

[100] Q. Fu et al., *"Linear strain-gradient effect on the energy bandgap in bent CdS nanowires"*, Nano Res., vol. 4, pp. 308–314, 2010.

[101] L. Kou, Y. Zhang, C. Li, W. Guo and C. Chen, *"Local-Strain-Induced Charge Carrier Separation and Electronic Structure Modulation in Zigzag ZnO Nanotubes : Role of Built-In Polarization Electric Field"*, J. Phys. Chem. C, vol. 115, pp. 2381–2385, 2011.

[102] B. Wei, K. Zheng, Y. Ji, Y. Zhang, Z. Zhang and X. Han, *"Size-Dependent Band gap Modulation of ZnO Nanowires by Tensile Strain"*, Nano Lett., vol.12, pp. 4595, 2012.

[103] Y. Lv, W. Liu, J. Huang and L. Yao, *"CdS Nanotubes and Y-Branched Nanochannels in AAM Fabricated by a Double Diffusion Route"*, Journal of Nanomaterials, vol.18, pp. 546715, 2011.

[104] S. P. Mondal, K. Das, A. Dhar and S. K. Ray, *"Characteristics of CdS nanowires grown in a porous alumina template using a two-cell"*, Nanotechnology, vol. 18. pp. 095606, 2007.

[105] F. Zhang and S. S. Wong, *"Controlled Synthesis of Semiconducting Metal Sulfide Nanowires"*, Chem. Mater., vol. 21, pp. 4541–4554, 2009.

[106] Y. Piao, H. Lim, J. Y. Chang, W.-Y. Lee and H. Kim, *"Nanostructured materials prepared by use of ordered porous alumina membranes"*, Electrochimica Acta, vol. 50, pp. 2997–3013, 2005.

[107] Y. Piao and H. Kim, "*Paired cell for the preparation of AgI nanowires using nanoporous alumina membrane templates"*, Electrochimica Acta, pp. 2898–2899, 2003.

[108] J. M. Patete, X. Peng, C. Koenigsmann, Y. Xu, B. Karn and S. S. Wong, *"Viable methodologies for the synthesis of high-quality nanostructures"*, Green Chemistry, vol. 13, pp. 482, 2011.

[109] A. Varghese and S. Datta, *"Directionally asymmetric self-assembly of cadmium sulfide nanotubes using porous alumina nanoreactors: Need for chemohydrodynamic instability at the nanoscale"*, Phy. Rev. E, vol. 85, pp. 056104, 2012.

[110] A. Varghese, *"Enhanced Photoluminescence from Ordered Arrays of Cadmium Sulfide Nanotubes Synthesized Using Nanoscale Chemical Reactors"*, Journal of Nanoscience and Nanotechnology, vol. 14, pp. 4495–4499, 2014.

[111] W. Zhou and Z. Lin, *Scanning Microscopy for Nanotechnology*. New York: Springer, 2006.

[112] R. F. Egerton, *Physical Principles of Electron Microscopy*. New York: Springer, 2005.

[113] Y. Leng, *Materials Characterization*. Singapore: John Wiley & Sons, 2008.

[114] T. Owen, *Fundamentals of UV-visible spectroscopy*. Hewlett-Packard Company, 1996.

[115] J. Singh and K. Shimakawa, *Advances in Amorphous Semiconductors*. London: Taylor Francis, 2003.

[116] S. Varghese, M. Iype, E. J. Mathew and C. S. Menon, *"Determination of the energy band gap of thin films of cadmium sulphide , copper phthalocyanine and hybrid cadmium sulphide / copper phthalocyanine from its optical studies",* Materials Letters, vol. 56, pp. 1078–1083, 2002.

[117] Z. Khan, M. Khannam, N. Vinothkumar, M. De and M. Qureshi, *"Hierarchical 3D NiO CdS heteroarchitecture for efficient visible light photocatalytic hydrogen generation"*, J. Mater. Chem., vol. 22, no. 24, pp. 12090, 2012.

[118] Stephen L. Upstone, *Encyclopedia of Analytic Chemistry*, Edited by R. A. Mayers, John Wiley & Sons Ltd, pp. 1699–1714, 2000.

[119] B. D. Cullity, *Elements oF X-Ray Diffraction*. Addison-Wesley, 1956.

[120] R. Guinebretire, *X-ray Diffraction by Polycrystalline Materials*. London: Antony Rowe Ltd, 2007.

[121] D. Zanchet, B. D. Hall and D. Ugarte, *Characterization of Nanophase Materials*. Wiley-Vch Verlag GmbH, 2000.

[122] J. T. Eijkel and A. van den Berg, *"Nanofluidics and the chemical potential applied to solvent and solute transport"*, Chem. Soc. Rev., vol. 39, pp. 957-973, 2010.

[123] E. A. Bluhm, *"Surface Effects on Cation Transport across Porous Alumina Membranes"*, Langmuir, vol. 15, pp. 8668–8672, 1999.

[124] T. M. Squires and S. R. Quake, *"* Microfluidics: Fluid physics at the nanoliter scale*"*, Rev. Mod. Phys., vol. 77, pp. 977, 2005.

[125] D. R. Lide, *CRC Handbook of Chemistry and Physics*. Boca Raton, CRC Press, 2005.

[126] S. Kalliadasis, J. Yang and A. D. Wit, *"Fingering instabilities of exothermic reaction-diffusion fronts in porous media", Phys. Fluids*, vol. 16, pp. 1395, 2004.

[127] S. Swernath and S. Pushpavanama, *"Viscous fingering in a horizontal flow through a porous medium induced by chemical reactions under isothermal and adiabatic conditions", J. Chem. Phys.*, vol. 127, pp. 204701, 2007.

[128] S. P. Jang, J. H. Lee, K. S. Hwang and S. S. Choi, *"Particle concentration and tube size dependence of viscosities of Al_2O_3-water nanofluids flowing through micro- and minitubes"*, Appl. Phys. Lett., vol. 91, pp. 243112, 2007.

[129] H. M. Lu and Q. Jiang, *"Size-Dependent Surface Tension and Tolman's Length of Droplets"*, Langmuir, vol. 21, pp. 779–781, 2005.

[130] T. Podgorski, M. C. Sostarecz, S. Zorman and A. Belmonte, *"Fingering instabilities of a reactive micellar interface"*, Phys. Rev. E, vol. 76, pp. 016202, 2007.

[131] T. Gerard and A. D. Wit*, "Miscible viscous fingering induced by a simple A+B = C chemical Reaction"*, Phys. Rev. E, vol. 79, pp. 016308, 2009.

[132] Y. Nagatsu and A. D. Wit, *"Viscous fingering of a miscible reactive A + B= C interface for an infinitely fast chemical reaction: Nonlinear simulations"*, Phys. Fluids, vol. 23, pp. 043103, 2011.

[133]J. Kiruthiga and A. Chatterji, *"Nanochannel induced advection with reaction-diffusion dynamics of reacting ions leads to self-assembly of ordered cylindrical structures*", J. Chem. Phys, vol. 138, pp. 024905, 2013.

[134]J. Kiruthiga and A. Chatterji, *"Self-assembly of monodisperse CdS nanocylinders with an axial pore*", Physical Review E, vol. 89, pp. 022304, 2014.

[135] L.D. Landau and L. M. Lifshitz, *Fluid Mechanics*, chapter 3.

[136]T. Kanniainen, S. Lindroos, J. Ihanus, and M. Leskela, *"Synthesis of CdS nanoparticles with enhanced optical properties",* J. Mater. Chem, vol. 6, pp. 983–986, 1996.

[137] A. Varghese, P. Ghosh and S. Datta, *"Cadmium Vacancy Minority Defects as Luminescence Centers in Size and Strain Dependent Photoluminescence Shifts in CdS Nanotubes"*, J. Phys. Chem. C, vol. 118, pp. 21604-21613, 2014**.**

[138] H. Xue, N. Pan, M. Li, Y. Wu, X. Wang and J. G. Hou, *"Probing the strain effect on near band edge emission of a curved ZnO nanowire via spatially resolved cathodoluminescence"*, Nanotechnology, vol. 21, pp. 215701, 2010.

[139] S. Xiong, B. Xi, C. Wang, G. Zou, L. Fei, W. Wang and Y. Qian, *"Shape-Controlled Synthesis of 3D and 1D Structures of CdS in a Binary Solution with L-Cysteine's Assistance"*, Chem. Eur. J, vol. 13, pp. 3076, 2007**.**

[140] D. Fan, P. J. Thomas and P. O'Brien, *"Deposition of CdS and ZnS thin films at the water/toluene interface"*, J. Mater. Chem., vol. 17, pp. 1381-1386, 2007.

[141] X.Li, H, Chu and Y. Li, *"Sacrificial template growth of CdS nanotubes from $Cd(OH)_2$ nanowires"*, Journal of Solid State Chemistry, vol. 179 , pp. 96-102, 2006.

APPENDIX

The research work presented in this thesis has appeared in the following publications.

1. **Arthur Varghese** and Shouvik Datta, "Directionally asymmetric self-assembly of cadmium sulfide nanotubes using porous alumina nanoreactors: Need for chemohydrodynamic instability at the nanoscale", *Physical Review E*, vol. 85, pp. 056104, 2012.

2. **Arthur Varghese**, "Enhanced Photoluminescence from Ordered Arrays of Cadmium Sulfide Nanotubes Synthesized Using Nanoscale Chemical Reactors", *Journal of Nanoscience and Nanotechnology*, vol. 14, pp. 4495-4499, 2014.

3. **Arthur Varghese**, P. Ghosh and Shouvik Datta, "Cadmium Vacancy Minority Defects as Luminescence Centers in Size and Strain Dependent Photoluminescence Shifts in CdS Nanotubes", *J. Phys. Chem. C*, vol. 118, pp. 21604-21613, 2014**.**